UNIVERSITÀ DI PARMA

UNIVERSITÀ DEGLI STUDI DI PARMA

DOTTORATO DI RICERCA IN
"TECNOLOGIE DELL'INFORMAZIONE"

XXXIV Ciclo

Femtosecond laser-induced two-photon polymerization and modeling of multicore optical fibers

Coordinatore:
Prof. Marco locatelli

Tutore:
Prof. Annamaria Cucinotta

Co-tutore:
Dr. Adrian H.A. Lutey

Dottorando: Seyyedhossein Mckee

Anni 2018/2022

I dedicate my thesis to all the nurses, doctors and scientists who try to save lives with indescribable effort especially during the COVID-19 pandemic as well as to my family for their invaluable support.

Contents

List of Figures

List of Tables

Introduction

The world fundamentally changed when an American physicist Theodore Harold Maiman invented the revolutionary first working laser in 1960. The term *laser* originated as an acronym for light amplification by stimulated emission of radiation. Compared to conventional light sources, it attracted significant interest due to its unique characteristics including monochromaticity, coherence, collimation and brightness. Depending on the type, lasers have wavelengths in the electromagnetic (EM) spectrum ranging from ultraviolet (UV) to infrared (IR). Each of these wavelengths has its own specific energy characteristics and therefore applications. As a result, a wide variety of laser applications have been developed and applied in various fields including industry (including additive manufacturing (AM)), science, astronomy and healthcare, as well as communications and military.

In this thesis, two cutting-edge laser technologies have been thoroughly investigated. The present work consists of two main parts. The first focuses on femtosecond pulsed laser-induced two-photon polymerization (TPP) to fabricate ultraprecise 3D microscale structures, an activity undertaken as part of a joint project between the Department of Chemistry and the Department of Engineering and Architecture at the University of Parma. The second focuses on multicore fibers (MCFs) for amplification and lasing, an activity undertaken as part of a close collaboration between two Universities of Parma and Modena.

The significant technical development of ultrashort pulsed laser systems has led to novel opportunities for AM, including fabrication of arbitrary and complex 3D structures having features as small as 100 nm through TPP processes. Over recent

years, this cutting-edge AM technology has received growing attention due to the creation of devices in the fields of advanced photonics (e.g., photonic crystals and microresonators), as well as biomedical applications (e.g., biological scaffolding, microfluidic devices and microneedles for drug delivery). Therefore, in order to stay up-to-date with the latest technology and enjoy the potential benefits of this innovative method, the laser laboratory at the Department of Engineering and Architecture (DIA) was equipped with an ultrashort pulsed laser for microfabrication via TPP, on loan from the University of Bologna. The laser generates 80 fs pulses with an energy of 70 nJ and peak power of approximately 100 kW. The repetition rate and operating wavelength are 76 MHz and 1030 nm, with the latter frequency doubled to 515 nm with a pulse energy of 25 nJ. It is worth noting that the TPP system used for the fabrication of 3D micro-scale structures needed to be set up completely, which took more than a year due to its considerable complexity to align components including the laser source, shutter, attenuators, stages, mirrors, objective lens etc., with the potential to use infrared or green laser beams depending on the desired structures. During the second and third year of the doctorate, the influence of ultrashort pulsed laser beams on different types of materials including commercial and custom-made photoresists was investigated in order to choose the most suitable resin for the TPP setup. Once the best material was chosen for the operating range of the laser system, several tests were performed to determine appropriate fabrication parameters such as laser power, scanning speed, layer height and hatch distance to produce the desired 3D microstructures with the highest possible structural resolution.

In parallel with the first project, a second topic was addressed, centered on the evaluation of the performance of multicore fibers (MCFs) designed for high-power fiber laser applications. This cutting-edge technology is posited as the best candidate to replace conventional fibers in lasers and optical amplifiers due to their considerable potential for delivering a single higher-power beam by combining several lower power beams coherently, which facilitates the possibility of overcoming the threshold power limit caused by the onset of nonlinearities and transverse mode instabilities (TMIs). However, the thermal effect on all doped active cores of a uniformly applied heat load, originating from the quantum defect in the amplification process, leads

to interaction between optically uncoupled cores, which can result in spurious mode coupling that causes detrimental effects on system performance. In this work, different configurations of this new revolutionary fiber including 9-core and 16-core MCFs have been investigated. The effects of thermal dissipation on doped cores and their relative material refractive index variations, as well as mode dephasing, have been investigated through a combined thermal and optical finite element method (FEM) model which is quite effective for the analysis of such problems.

The dissertation is organized as follows:

Part I

- Chapter 1 introduces 3D printing (also known as additive manufacturing) as a promising technology to produce arbitrary objects directly from 3D digital models by adding a wide range of materials layer-by-layer. The main advantages of this technology over subtractive manufacturing are highlighted as well. Moreover, two different types of AM technology based on laser material interactions are discussed in detail, including powder bed fusion and stereolithography, including their applications and steps needed to produce desirable structures.

- Chapter 2 provides a general literature review of two-photon polymerization as a revolutionary novel 3D printing technique to fabricate complex and ultraprecise 3D micro- and nano-scale structures with resolutions below the diffraction limit of the employed wavelength. The phenomenon of two-photon absorption, which represents the interaction between two photons emitted from an ultrafast laser source and a material including degenerate and non-degenerate processes, is summarized in this chapter. In addition, the various types of photosensitive materials (photoresists) used in this process, such as negative and positive photoresists and their fundamental differences, are reviewed in detail. Finally, the spatial resolution of fabricated microstructures, directly related to the voxel size or the minimum fabrication unit volume, is discussed.

- Chapter 3 investigates negative photoresists employed during laboratory activities, including commercial (femtoBond C and E-Shell 300) and custom-made (TPGDA, PEGDA and PETIA) compositions. A custom-built setup employed for experiments within this work with a brief description of its key components such as an ultrashort pulsed laser source, shutter, motorized attenuators, high-precision stages, etc., are presented in this chapter. Moreover, the steps which must be followed to fabricate desirable 3D microscale structures are described in detail.

- Chapter 4 presents experimental results relating to the polymerization of materials, namely transformation from a liquid to a solid state via two-photon absorption, along the path of the moving focused laser beam emitted from an Ytterbium-doped Potassium Gadolinium Tungstate (Yb:KGW) ultrashort pulsed laser source. The details of determining the entire range of usable laser power, from the polymerization threshold to the damage threshold, is described in this chapter by producing an array of lines within the photoresists. Several tests are also performed to build small square prisms with dimensions of 350 $\mu m \times 350\ \mu m \times 1000\ \mu m$ in order to choose the most suitable photoresists for experiments.

- Chapter 5 reports the development of 3D solid microneedle arrays as a novel transdermal drug delivery system with 49 conical needles arranged in a 7×7 configuration containing cones with a base diameter of 250 μm, tip diameter of 30 μm, height of 800 μm and pitch of 500 μm from PETIA. The influence of fabrication parameters including laser power, scanning speed, hatch distance and layer height on the structural resolution and fabrication time of microneedles are studied in detail. Furthermore, the interaction between a single microneedle and human skin through finite element simulations is investigated.

Part II

- Chapter 6 introduces multicore fibers as a cutting-edge technology to overcome the threshold power limit caused by the onset of nonlinearities and transverse mode instabilities in high-power applications by combining several lower

power beams coherently to obtain a single higher power beam. Moreover, the impact of thermal effects, due to the quantum defect in the optical amplification process, on the performance of 9-core and 16-core Yb-doped multicore fibres designed for high-power lasing and amplification applications is investigated.

The aims and objectives achieved during three years of the PhD course are listed below:

- Knowledge of the state-of-the-art of TPP in relation to technologies and materials.
- Knowledge of the properties of a femtosecond laser as well as the ability to use one.
- Designing and implementing the optical path for TPP machining in both infrared and visible through non-linear optics.
- Photoresist optimization in relation to the properties required according to the application (chemical/thermal stability and photostability, mechanical properties, optics, biocompatibility, etc.).
- Ability to create simple 3D microstructures.
- Design of complex 3D microstructures for specific applications such as microneedle arrays.
- Ability to analyze the resolution of fabricated 3D microstructures through scanning electron microscope (SEM).
- Analysing the impact of thermal effects, due to the quantum defect in the optical amplification process, on the performance of 9-core, 16-core Yb^{3+}-doped multicore fibres (MCFs) designed for high-power lasing and amplification applications through finite-element method (FEM) simulations.

Part I - Femtosecond laser-induced two-photon polymerization

Chapter 1

Introduction to laser-based 3D printing

The optimal use of time and resources, together with increased product functionality and customization, are amongst the primary reasons motivating companies to move towards advanced manufacturing technologies. Three-dimensional (3D) printing, also referred to as additive manufacturing (AM) [11] or rapid prototyping, is becoming increasingly popular due to its ability to build 3D structures directly from a computer-aided design (CAD) file by adding material layer-by-layer. In contrast to subtractive manufacturing (SM) technologies, which remove undesired material from a workpiece to build objects, this approach brings appreciable benefits such as increased design flexibility and dramatically reduced manufacturing waste [12] as well as reduction in fabrication time [13]. Figure 1.1 shows the difference between subtractive and additive manufacturing methods [14]. 3D printing also allows the design and creation of objects with much higher structural resolution and quality than conventional manufacturing methods while using diverse materials including thermoplastics, metals, ceramics and resins [15] depending on the desired application. This promising technology has found a wide range of application areas in medicine (e.g., tissue engineering, dental implants, etc.), agriculture [16], food [17], building and construction [18], as well as in the automotive and aerospace industries [1].

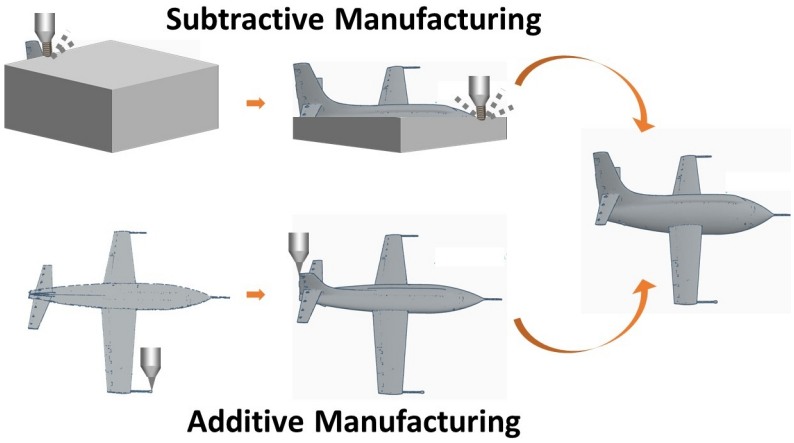

Figure 1.1: Classification of manufacturing processes: subtractive and additive.

There are several types of laser-based 3D printing, including powder bed fusion (selective laser melting, selective laser sintering), stereolithography [19] and two-photon polymerization [20], which are able to build high resolution structures via a focused laser beam. Although each of the mentioned methods has its own distinct attributes, they share some similar steps in the production of a structure. Typically, these include:

- 3D modeling of the desired object using CAD software.
- Converting the CAD file into STL format.
- Numerically slicing the STL file into thin layers or cross-sections using slicer software.
- Generating a G-code file and transferring it to the 3D printing machine.
- Printing the object in a layer-by-layer manner.
- Post processing (e.g., removing the object from the build platform, removing possible support structures, heat treatment, polishing, etc.) to obtain the fabricated structure as shown in Figure 1.2.

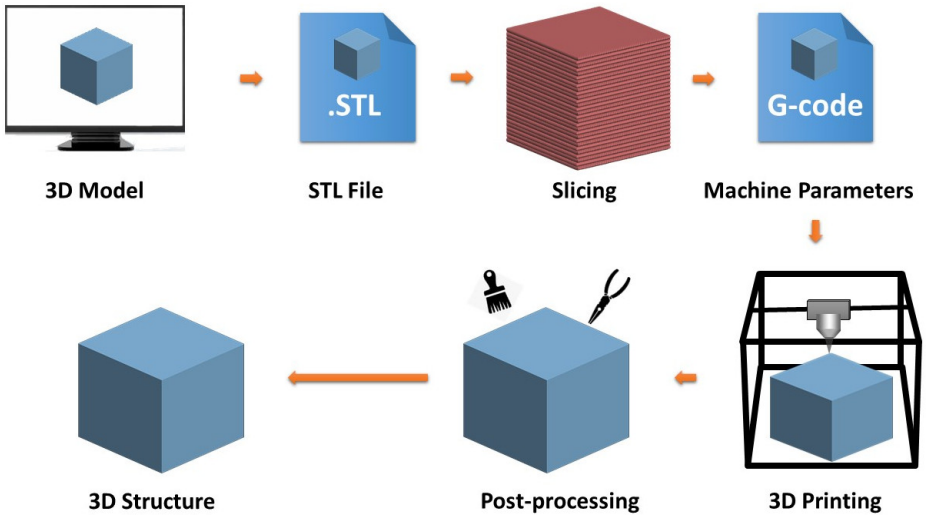

Figure 1.2: Common steps in additive manufacturing.

Choosing the right 3D printing process for a certain applications is vital to achieve design goals. The following chapter gives a brief introduction to laser powder bed fusion (selective laser melting, selective laser sintering) and stereolithography processes, as well as their differences.

1.1 Laser powder bed fusion

Over the years, laser powder bed fusion (LPBF), a subset of 3D printing, has gained much attention due to its potential to produce complex 3D structures with accurate dimensions and hollow structures. Increasing the speed of prototyping and manufacturing, and reducing fabrication costs and material waste [21], are the greatest benefits of this process over alternative traditional methods. Therefore, LPBF is the most common 3D printing technology in modern automotive and aerospace industries, as well as in medical fields [22]. The LPBF process uses a high-power laser beam to melt or sinter specific points on a layer of metallic or plastic powder to build 3D solid objects layer-by-layer. The high density of fabricated objects due to tight

adhesion between layers makes this process a popular choice among manufacturers. Depending on powder material, LPBF can be divided into two classes: selective laser melting (SLM) and selective laser sintering (SLS).

1.1.1 Selective laser melting

Selective laser melting (SLM), also referred to as laser powder bed fusion (LPBF) or direct metal laser melting (DMLM), is one of the most impressive 3D printing techniques, allowing sophisticated structures to be produced by applying a focused laser beam to melt metal powders [23]. SLM can be employed with diverse materials including stainless steel, titanium, aluminium [24] and composite materials [25], depending on the desired application. As a result, this process can be used in a wide range of industrial applications including aerospace, automobile, oil refinery, marine, construction [26], jewelry and medical devices (e.g., trabecular lower jaw implants, dense skull plates and dental implants) [27, 28]. Figure 1.3 presents a schematic of the SLM manufacturing process, which depicts several steps needed to reach the desired result. The fabrication process begins once a thin (20–100 μm) [29] layer of powder from the powder delivery cylinder is homogeneously spread across the build platform by a roller. The scanner system then allows the high power laser beam to move across the surface of the layer in correspondence with a G-code file. After heating the first layer of powder, the fabrication piston is lowered according to the layer height and a new layer of powder is deposited. The layering and melting process is repeated until the the final part is fabricated. After completion of the entire process, the fabricated part is removed from the base plate and unmelted powder is removed with brushes and compressed air during post processing. In order to prevent the material from oxidizing, the building chamber must first be filled with high-purity inert gas such as argon or nitrogen [30]. A review of the literature reveals that choosing the right material and fabrication parameters such as laser power, scanning speed and spot size plays a fundamental role in determining the quality of the final part [31]. Therefore, the optimal combination of fabrication parameters is one of the vital steps required to achieve the desired structure in the SLM process.

Table 1.1 reports the major advantages and disadvantages of SLM [32, 33, 34].

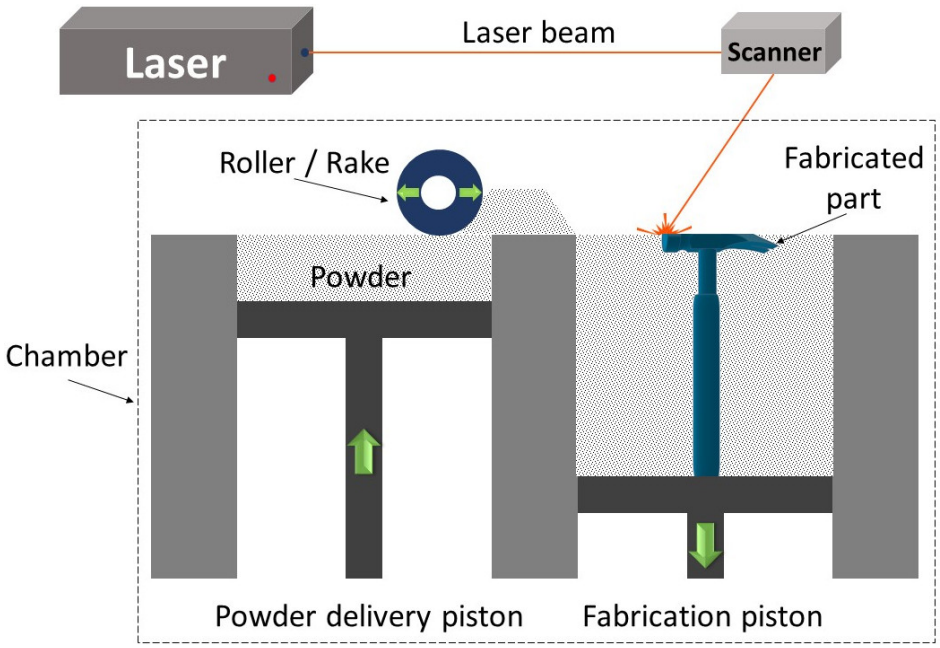

Figure 1.3: Schematic setup of SLM manufacturing [1].

Advantages	Disadvantages
Producing complex devices with acceptable mechanical properties	High cost of SLM machines and materials
Using a broad range of metal materials	Inert gas supply is required
Relatively fast	Post-processing is required

Table 1.1: SLM technique: advantages and disadvantages.

1.1.2 Selective laser sintering

Selective laser sintering (SLS) was first developed by Dr. Carl Deckard and and Dr. Joseph Beaman [35] in the 1980s at the University of Texas. It is often used in the manufacturing industry [36] where a thermal source such as focused laser beam (e.g., carbon dioxide CO_2 laser source) [37] precisely sinters material in powder form, without melting, to fabricate 3D structures. SLS and SLM share similar process steps

to build an object as described in the previous section, with the main difference between them being the employed materials. In fact, SLS uses a variety of materials including ceramic and thermoplastics such as PA12 (Nylon) and PEEK (Polyether ether ketone) [38]. Numerous applications have been reported in the literature for this process in the medical, dentistry, military, engineering and electronics industries [39]. The most significant advantages and disadvantages of SLS are listed in Table 1.2 [40, 41].

Advantages	Disadvantages
Fabricating complex shapes	High cost of SLS machines as well as materials
Using a broad range of materials	Poor surface finish
Short manufacturing cycle	Post-processing is required
No need for supports	Defects in the manufactured parts due to large shrinkage rates

Table 1.2: SLS technique: advantages and disadvantages.

1.2 Laser-stereolithography

Laser-based stereolithography (referred to as SLA or vector-based SLA) [42] belongs to the first generation of prototyping methods that were developed and commercialized, and is still widely used today in industry [43] since it enjoys important advantages of high precision and speed in fabricating complex shapes [44] using materials such as polymer, ceramic composite [45] and metal [42] to fabricate 3D objects that would be difficult or impossible to manufacture with traditional methods. SLA is classified as vat photopolymerization (VP) according to the American Society for Testing and Materials (ASTM) standards [46]. During the SLA fabrication process, an ultraviolet (UV) laser beam is focused into a vat filled with liquid resin. The obtained result is selectively curing and solidifying on the surface of the resin along the path followed by the moving focused laser beam. Therefore, using a layer-by-layer ap-

proach is the only option to fabricate 3D structures. In order to create a new surface, the fabrication platform is lowered into the resin vat according to the layer height, ranging from 25 μm to 100 μm [47], and another liquid resin layer is deposited, with excess resin removed by a blade. These steps are repeated until the complex 3D structure is produced as shown in figure 1.4. The next step after obtaining the desired structures is developing the sample by applying a suitable solvent such as isopropyl alcohol to remove unsolidified material and then manually removing support structures made from the same printing material [42]. Finally, an ultraviolet irradiation device, if needed, is used to provide uniform cross-linking of the developed structure to ensure that it is mechanically stable with the desired structure. SLA finds many uses in a wide variety of industries such as aerospace, automotive [42], molds, toys [48], conceptual models and biomedical applications including customized implants and tissue engineering [49]. The key advantages and disadvantages of SLA are summarized in Table 1.3 [50, 51, 42].

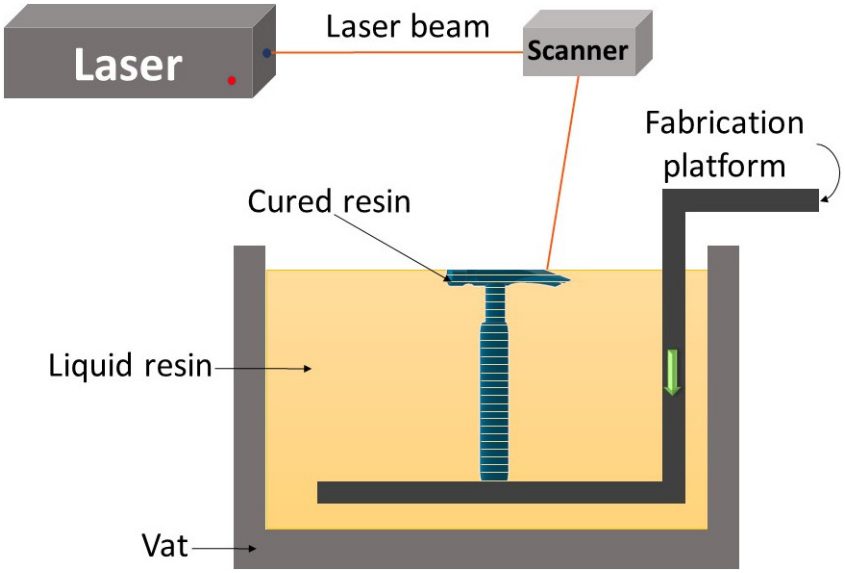

Figure 1.4: Schematic setup of laser-SLA. A UV laser is applied to solidify the surface of the liquid resin in a layer-by-layer approach to fabricate 3D structures [2].

Advantages	Disadvantages
Producing complex 3D structures with high accuracy and resolution	Resin drainage of thin walled parts is a challenge
Using a broad range of materials depending on desired applications	High cost of SLA machines as well as advanced materials
Relatively fast	Post-processing is required
Reduction of scrap	Weak mechanical properties

Table 1.3: SLA technique: advantages and disadvantages.

It is worth noting that traditional SLA and two-photon polymerization (as one of the two main topics in this work) are based on a similar mechanism where polymerization of the liquid resin, namely transformation from a liquid to a solid state, is a crucial process in both approaches to produce 3D structures. However, by employing femtosecond laser pulses during two-photon polymerization process, a minimum feature size is achieved which is several orders of magnitude smaller than SLA resulting in significant improvement in structural resolution. Therefore, this cutting-edge AM technology allows the fabrication of devices for advanced photonics and biomedical applications in a single manufacturing step which is in fact impossible to happen using layer-by-layer SLA process.

This process will be discussed in greater detail in the chapters that follow.

Chapter 2

3D Microfabrication via two-photon polymerization

Motivation is a fine example of social complexity.
It is nonlinear and sometimes unpredictable.
It cannot be defined or modeled with a single diagram.

– Jurgen Appelo

Over the past decades, unprecedented advances in 3D printing technology have led to the emergence of innovative approaches to this cutting-edge technology. Among these, two-photon polymerization (referred to as TPP or 2PP), has gained much attention in terms of research due to its promising potential as a revolutionary maskless 3D microfabrication technique [52, 53], to achieve resolution beyond the diffraction limit [54, 55, 56, 57, 58, 59]. The Abbe diffraction limit is one of the most widely used formula [60] to determine the spot size of a laser beam [61], which is given as

$$d = \frac{\lambda}{2NA} \tag{2.1}$$

where λ and NA are the laser wavelength and numerical aperture of the focusing objective, respectively [62]. This outcome owes to major technological advances in ultrashort pulsed laser systems [63] whose pulse duration and pulse energy are often

in the order of femtoseconds (fs or 10^{-15} s) [64, 65] and nanojoules (nJ) [66], respectively. In fact, TPP, employing an ultrashort pulsed laser source and appropriate photoresist (photosensitive material), is considered a breakthrough technique for producing arbitrary micro- or nanoscale structures directly from a CAD model [67] without requiring clean room facilities [68]. Since 1997, when the first high-resolution 3D microstructure was fabricated with a titanium-sapphire ultrashort pulse laser through TPP by Shoji Maruo, Osamu Nakamura and Satoshi Kawata [69], this technology has experienced significant progress in a large variety of academic and commercial applications including 3D photonic crystals [70, 71], metamaterials [72, 73], microelectromechanical systems (MEMS) [74, 75, 67], 3D microactuators [65], labs on a chip [76], microrobotics [77], plasmonics [78], scaffolds for cell cultures [79, 80], microfluidics [81, 82] and microneedle (MN) devices [83, 84, 85, 86].

In spite of TPP capability to produce true 3D microstructures [65] with higher resolutions and smoother surfaces [87] which in fact distinguishes this technique from the conventional ones, relatively low mechanical strength of functional parts due to the submicron size of components [67, 88] as well as very low area printing speed [89] still belong to the main issues of this technology. Therefore, by solving the aforementioned problems and manufacturing low-cost femtosecond lasers, the final throughput of fabrication can be improved significantly which results in commercialization of the TPP process and subsequently higher chances of being applied in various optical and medical fields [90, 91, 92].

2.1 Two-photon absorption

The principle of TPP technology is based on non-linear two-photon absorption (TPA or 2PA), which represents the interaction between two photons emitted from an ultrafast laser source and a material. TPA is the excitation of one atom or molecule from the ground state to the excited state by simultaneous absorption of two photons with the same or different energy, referred to as degenerate and nondegenerate processes, respectively (Figure 2.1) [62]. The sum of the energy of the two photons determines the energy difference between the ground and excited states where h and

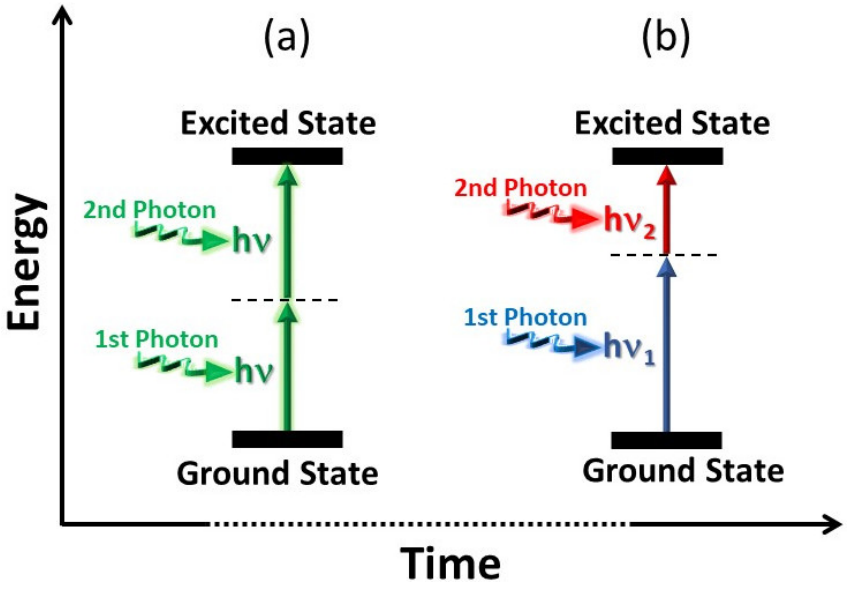

Figure 2.1: Schematic illustration of TPA: degenerate (a) and non-degenerate (b) processes. Dashed horizontal lines indicate virtual intermediate states [3].

ν are Planck's constant ($6.62607015 \times 10^{-34}$ Js) and the photon frequency, respectively.

This phenomenon was first predicted theoretically by Maria Göppert-Mayer in 1931 as part of her Ph.D. thesis at the University of Göttingen in Germany. Thirty years later, Kaiser and Garret observed TPA in a CaF_2:Eu^{2+} crystal for the first time by employing a pulsed ruby-crystal laser at a wavelength of 694 nm [93], which produced significantly greater peak power than a flash lamp [94]. In the 1990s, as sub-picosecond pulsed lasers (e.g., Ti:sapphire lasers) became more widely available, TPA became more accessible to study [95]. TPA has shown considerable promise not only in 3D microfabrication but also in microscopy, 3D data-storage, optical power limiting and photodynamic therapy [95, 96].

The process initiates when ultrashort laser pulses, which have the ability to produce high peak power (tens or hundreds of kilowatts) [97] over a very short time period (less than a picosecond) [98], are tightly focused into a very small volume

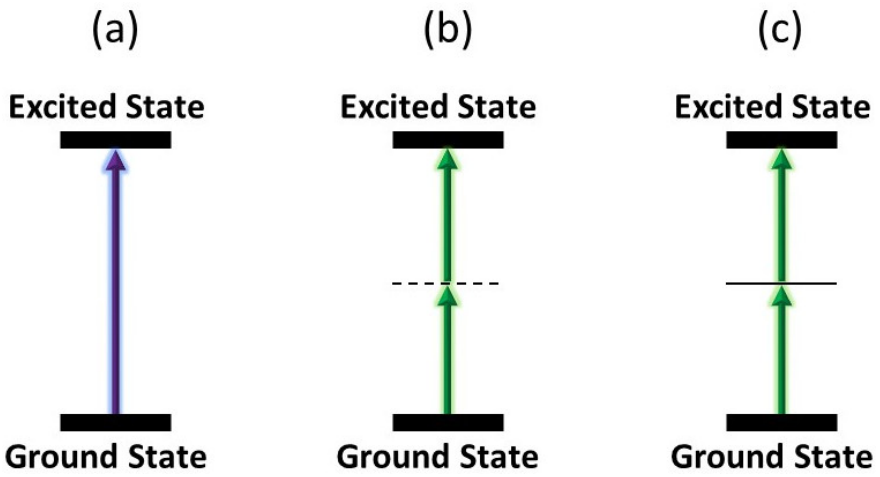

Figure 2.2: Schematic diagrams comparing different absorption mechanisms. One-photon absorption (a), simultaneous TPA (b) and stepwise TPA (c) of laser light. A dashed horizontal line indicates a virtual intermediate state while a solid horizontal line indicates a real intermediate state [4].

of transparent photosensitive material that triggers polymerization (solidification) to fabricate arbitrary, complex micro- and nanoscale structures [99, 100, 101, 102]. The TPA process is mainly divided into two types, which are simultaneous (Figure 2.2 (b)) and stepwise (Figure 2.2 (c)) absorption processes [94]. Stepwise absorption takes place when an atom or molecule is excited to a real intermediate state through absorption of the first photon, after which the second photon triggers the final excited state. Simultaneous absorption instead takes place when there is an intermediate virtual state, which is in fact the ultimate result of the interaction between the electromagnetic field and matter. Contrary to simultaneous TPA, in stepwise TPA there is no requirement for coherence of the incident light, which can be considered as two distinct one photon absorption events (Figure 2.2 (a)). Simultaneous TPA is regarded as a more efficient and relevant option for microfabrication due to its extremely short virtual state lifetime, from 10^{-16} to 10^{-15} s, which is significantly shorter than the duration of the pulse [103]. Stepwise TPA instead has a real intermediate state lifetime

from 10^{-9} to 10^{-4} s [4, 104, 105].

2.1.1 Comparison between one- and two-photon absorption

Conventional stereolithography typically uses a UV laser to induce one-photon absorption (1PA) at a rate that is directly proportional to the incident intensity, while the process is restricted to the photoresist surface leading to reduced resolution (Figure 2.3 (a)). In contrast, TPP can achieve a significant improvement in structural resolution by employing femtosecond laser pulses, typically in the visible spectrum, that are able to deeply penetrate into the photoresist without being absorbed. The volume in which material transformation takes place is confined to the focal point [106], where the photon density is sufficiently high to induce absorption of two photons (Figure 2.3 (b)). During conventional stereolithography, the UV laser beam therefore excites an entire column of liquid resin via 1PA, whose final product is a two-dimensional (2D) pattern of polymerized material. During TPP, the visible femtosecond laser beam instead polymerizes only a small volume, called a voxel [107], in the region in which absorption takes place. TPA requires the use of longer wavelengths to reach a given excited state from the ground state. Photons with half the energy (or twice the wavelength) of the corresponding 1-photon transition must be used [108]. Under these conditions, TPA increases with the square of the intensity of the radiation once the polymerization threshold has been reached. TPP therefore enables the creation of structures that would be impossible to produce with conventional layer-by-layer 1PP.

2.2 Materials for two-photon polymerization

Since variety, availability and the right choice of materials play an important role in the structural resolution of a part or product in every fabrication process, such factors must also be considered for TPP. Therefore, the main focus of most research, both commercially and academically, is on the design and production of TPP-based materials to fabricate ultraprecise 3D structures at the micro- and nanometer scale. Novel photoresists such as biocompatible materials play an important role in tissue

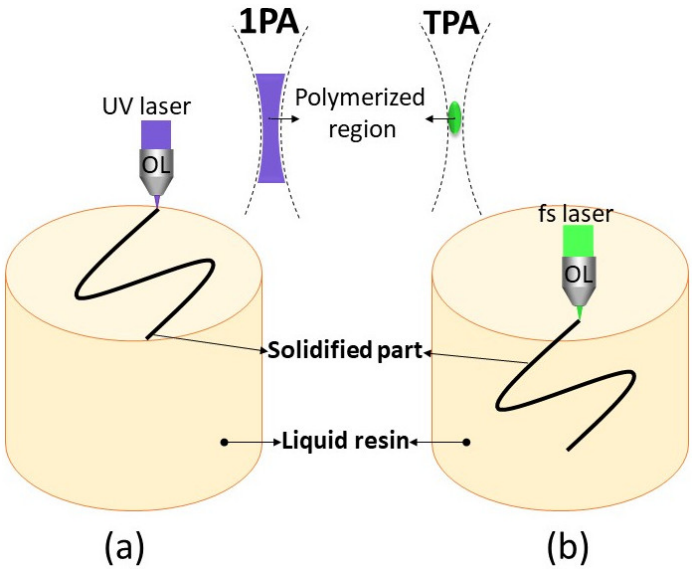

Figure 2.3: Comparison of different polymerization mechanisms: one-photon polymerization (1PP) (a) and two-photon polymerization (TPP) (b) [5, 6]. TPA occurs at the focal point of a focused femtosecond laser beam inside the liquid resin vat, while 1PA is restricted to the resin surface, which leads to reduction of structural resolution and quality.

engineering. For instance, they can be employed to fabricate 3D scaffolds which are essential to create living tissues and control the growth of tissue by integrating them artificially with host tissues within the body [7].

2.2.1 Photoresists chemical components

Photosensitive materials (photoresists), utilized for conventional stereolithography, can also be used for TPP-based microlithography [109] to produce μm- and sub-μm structures. However, over the last decade, a wide range of photoresists including light-sensitive polymers, hybrid polymer-ceramics and functionalized polymers [110, 111] have been specifically developed and commercialized for TPP, which is crucial for more precise applications.

In general, photoresists consist of acrylic or meth-acrylic monomers, photoinitiarors, absorbers, additives and fillers [42]. Amongst these, monomers and photoinitiators are regarded as the two fundamental components [112] since they have significant impact on the photopolymerization process.

- Low molecular weight monomers [113] are the building blocks of a polymer substance, which are connected to each other and form a solid 3D network after being exposed to a light source [42].

- Photoinitiators, which are molecules with low photon dissociation energy, play a crucial role in starting and determining the rate of polymerization by increasing the reactivity of the resin [114, 115, 116]. Photochemical initiation is usually achieved by subjecting suitable photoinitiators to UV irradiation; however, this can also be achieved through TPA at a longer wavelength, for example with tightly focused green femtosecond laser pulses. Choosing a photoinitiator with a large TPA cross-section (δ) is an essential aspect of a polymerization process [117] due to the effect that this parameter has on the reactivity of a photopolymer resin [118]. In ultrashort pulsed laser applications, negligible optical damage to photoresists can be obtained by selecting larger values of δ due to the lower required laser power [119]. In fact, δ of most conventional photoinitiators is designed for 1PA in the UV range, which is very small [120, 121]. As a result, in order to initiate the TPA process for microfabrication via TPP, higher laser power is needed. Generally, δ is expressed in Göppert-Mayer (GM) units, where 1 GM = 10^{-50}cm^{-4}s photon^{-1}, and can be obtained from the following equation:

$$\delta = \frac{\beta h\nu}{N} \tag{2.2}$$

where hν is the energy of the absorbed photon, N is the number of absorbers per unit volume and β is the TPA coefficient which contains information about the probability of a molecule or atom absorbing two photons simultaneously [3]. Z-scan, the nonlinear transmission (NLT) technique and two-photon excited fluorescence (TPEF) are the most common techniques for determining δ [95, 108].

- By applying absorbers, the penetration of light into the resin can be reduced and the depth can be also restricted, which is necessary to increase resolution in some applications [42].

- Additives and fillers are added to a liquid photoresist when it lacks the desired quality. Therefore, different properties including mechanical, thermal, optical or even electrical can be improved [122, 42].

2.2.2 Classification of photoresist

Negative-tone and positive-tone photoresists are commonly used for TPP microfabrication, as shown in Figure 2.4 (a). The significant difference between negative and positive photoresists after sample development is presented in Figure 2.4 (b). The illuminated volume of a negative-tone photoresists is cross linked and therefore the *unexposed* resin is removed during solvent treatment, or development. In positive-tone photoresists, however, laser exposure causes molecular dissociation and therefore *exposed* resin is washed away during sample development [7].

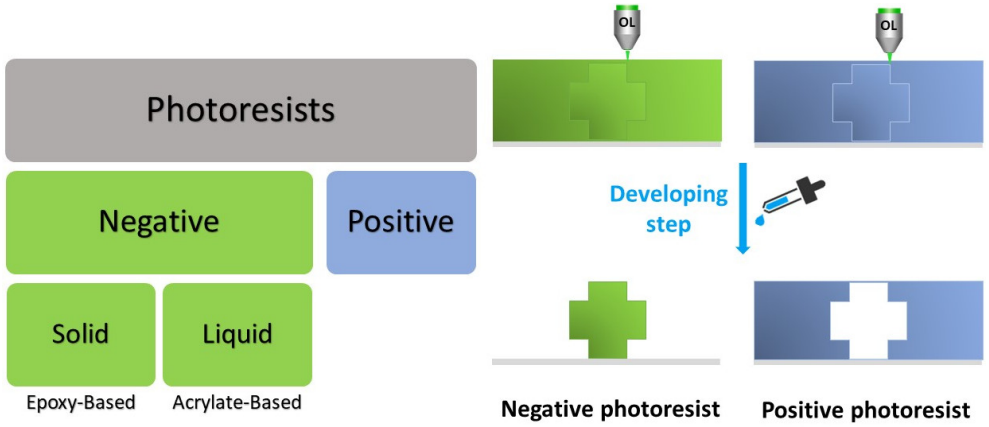

Figure 2.4: Classification of photoresists (a) [7]. Negative and positive photoresist sample development (b) [8].

Negative photosensitive materials can be either solid or liquid. The polymerization of the epoxy-based photoresists (e.g., SU8 formulation) occurs through cationic polymerization, where the interaction with laser irradiation produces an acid in the illuminated regions. Therefore, polymerization only happens after the post-exposure bake processing step. In liquid materials, which are acrylate- or methacrylate based, photopolymerization occurs via free-radical polymerization. As a result, TPP polymerization process can be monitored in real time [7].

In general, both negative and positive photoresists play a major role in the fabrication of 3D microstructures and have a number of benefits and drawbacks. Negative photoresists are less expensive with higher adherence potential to silicon as well as shorter processing times, while positive photoresists have superior resolution and thermal stability [123, 124]. Moreover, negative photoresists have higher sensitivity than positive photoresists, which is crucial to reducing exposure time and consequently increasing the efficiency of two-photon photopolymerization [125].

2.3 Two-photon photopolymerization

The components of a photoresist, including monomers/oligomers and photoinitiators, undertake chemical reactions after interacting with electromagnetic radiation from visible (e.g., green) or near-infrared (NIR) femtosecond laser pulses. Photopolymerization is the transformation of small unsaturated molecules (monomers) into macromolecules of polymer through a set of chemical reactions which consists of three basic steps: initiation (Eq. 2.3), propagation (Eq. 2.4) and termination (Eqs. 2.5, 2.6) [126, 127].

$$PI \overset{h\nu+h\nu}{\rightarrow} PI^{*} \rightarrow R\cdot, \tag{2.3}$$

$$R\cdot + M \rightarrow RM\cdot \overset{M}{\rightarrow} RMM\cdot \ldots \rightarrow RM_{n}\cdot \tag{2.4}$$

$$RM_{n}\cdot + RM_{m}\cdot \rightarrow RM_{m+n}R \tag{2.5}$$

$$RM_n \cdot + RM_m \cdot \rightarrow RM_n + RM_m \tag{2.6}$$

The photopolymerization process initiates when photoinitiators (PIs) absorb two photons to reach the excited state (PI^*) and subsequently break down into radicals ($R\cdot$). Subsequently, during the propagation phase, radicals react with monomers or oligomers (M) to form monomer radicals (RM_n), which leads to the growth of linear macromolecules. Finally, the chain propagation is stopped by combining two monomer radicals [128].

2.4 Resolution

The spatial resolution achieved during microfabrication via TPP is characterized by the voxel size, the minimum fabrication unit volume in both the lateral (xy-plane) and longitudinal (z-axis) directions [129]. Each voxel has an ellipsoidal shape [130] as shown in Figure 2.3 (green polymerized region), where various types of structures from a simple line to complex structures can be obtained by printing in a point-by-point manner. It is essential to emphasize that in order to form high resolution solid structures, an accurate distance between the voxels must be maintained.

The voxel width (d_r) and height (l_z) can be theoretically predicted with Equations 2.7 and 2.8 [131]:

$$d_r = w_0 (ln(\frac{I(r)}{I_{pt}}))^{\frac{1}{2}}, \tag{2.7}$$

$$l_z = 2z_r (\sqrt{\frac{I(z)}{I_{pt}}} - 1)^{\frac{1}{2}}. \tag{2.8}$$

where w_0 is the minimum laser spot radius, I_{pt} is the polymerization intensity threshold (Equation 2.9) and $I(r,z)$ is the Gaussian intensity distribution as a function of the radial r and axial z distances from the focal point (Equation 2.10).

$$I_{pt} = \frac{2TP_{avg}M^2}{R\tau w_0^2 \pi}, \tag{2.9}$$

where T is the objective transmittance, P_{avg} is the average laser power, M^2 is the beam quality parameter [132], R is the pulse repetition rate and τ is the laser pulse duration.

$$I(r,z) = I_0 \frac{w_0^2}{w(z)^2} exp(-\frac{2r^2}{w(z)^2}) \tag{2.10}$$

where I_0 is the intensity at the beam waist and $w(z)$ is the beam radius given by:

$$w(z) = w_0(1 + (\frac{z}{z_r})^2)^{\frac{1}{2}} \tag{2.11}$$

where z_r is the Rayleigh range, which can be expressed as the following:

$$z_r = \frac{n_0 w_0^2 \pi}{\lambda} \tag{2.12}$$

where n_0 is the real part of the material's refractive index and λ is exposure wavelength. In order to determine the voxel size, there are also other equations which can be found in the following references [133, 134, 135].

According to the findings of experiments performed within the present work, key parameters such as laser power, scanning speed and applied objective lens can all have a direct impact on voxel size, as discussed in Chapter 5. In fact, the fabricated structures with lower laser power and higher objective magnification exhibit higher quality and resolution.

Chapter 3

Materials and methods

3.1 Photoresists

A number of different photoresists were investigated experimentally, including commercial products femtoBond C and E-Shell 300, as well as custom compositions comprising TPGDA, PEGDA and PETIA. All were negative-tone resists where the illuminated volume was cross-linked, with the remaining volume washed away during sample development. The physical and chemical properties of photoresists can be altered to fit the requirements of specific applications by carefully changing the quantity of the components [136]. Making a selection of appropriate photopolymer resins was not only a crucial task but also a very time consuming process. This step was required to accomplished the desired resolution and quality of produced 3D devices with arbitrary geometries based on the employed experimental TPP setup.

3.1.1 Commercial photoresists

femtoBond C

femtoBond C (Laser nanoFab GmbH, Germany) is an organic-inorganic hybrid material with a ceramic content. Before laser exposure for microfabriaction via TPP, drops of femtoBond C must be deposited on a glass substrate and left to rest in a dark

environment for 24 hours at room temperature to evaporate residual solvent. This photoresist is more effective for the fabrication of microfluidics, micro-optics and micromechanics. It is also a biocompatible, which is ideal for biomedical devices.

E-Shell 300

E-Shell300 (EnvisionTEC GmbH, Gladbeck) is a cheap dimethacrylate-based liquid photoresist with a viscosity of 339.8 MPa·s, tensile strength of 51.6 MPa and density of 1.185 g/cm^3. This liquid resin is mainly designed for the fabrication of biomedical devices such as hearing aid shells as well as otoplastics due to its high strength and stiffness [137].

3.1.2 Custom photoresists

In this work, not only the above mentioned commercial photoresists were investigated but also several custom photoresists were developed and tested in order to determine the ideal composition in terms of monomer and photoinitiator for each chosen application.

TPGDA

TPGDA (Tripropylene glycol diacrylate) is a difunctional reactive diluent with a branched alkyl polyether backbone (Figure 3.1 (a)), which is supplied by Allnex (Allnex Holding S.à.r.l., Luxembourg). It is highly active and has low viscosity (10-15 MPa·s) and volatility. It is a suitable monomer when water resistance and good flexibility are required. TPGDA can be used in UV and electron beam cured coatings, inks and adhesives. Preparation of the photoresist was performed by mixing TPGDA monomer with 0.1 phr. (per hundred resin) IRGACURE 819 photoinitiator until the latter was completely dissolved in the liquid resin monomer.

PEGDA

PEGDA (Polyethylene glycol diacrylate) is a long-chain hydrophilic, crosslinking monomer (Figure 3.1 (b)). This thermosetting polymer can be used for a variety of drug delivery and tissue engineering based applications. The PEGDA photoresist was employed in this work was achieved by combining this monomer and Irgacure 819 (0.5 phr.).

PETIA

PETIA (Pentaerythritol triacrylate), developed by Allnex, is a multifunctional acrylate monomer containing a mixture of tri- and tetra-acrylate esters (ratio 1:1) with a high degree of acrylic unsaturation (Figure 3.1 (c)). It is characterized by a fast cure speed, high hardness and high gloss. This material is not only used for traditional UV cured coatings and ink systems where a high degree of crosslinking is required, but can also be employed in the field of additive manufacturing relating to vat photopolymerization technologies such as two-photon polymerization. Before printing, PETIA monomer and Irgacure 819 (0.1, 0.2, 0.5, 1 and 2 phr.) were mixed and kept away from light under magnetic stirring until the complete dissolution of the photoinitiator grains in the liquid resin monomer was achieved.

Photoinitiator

Irgacure 819, bis-(2, 4, 6-trimethylbenzoyl)-phenylphosphine oxide (BASF, Germany) was employed as photoinitiator (Figure 3.1(d)) in order to further improve the efficiency of the TPA process. When exposed to UV radiation, Irgacure 819 is decomposed into two radicals that can react with a monomer by opening its carbon-carbon bond and initiating a three dimensional network. The polymer chains are propagated via radical reactions with available acrylate double bonds on monomers or other polymer chains, giving rise to a thermoset crosslinked structure. Photopolymerization can be controlled by varying the laser intensity, photoinitiator concentration, exposure time, or monomer structure.

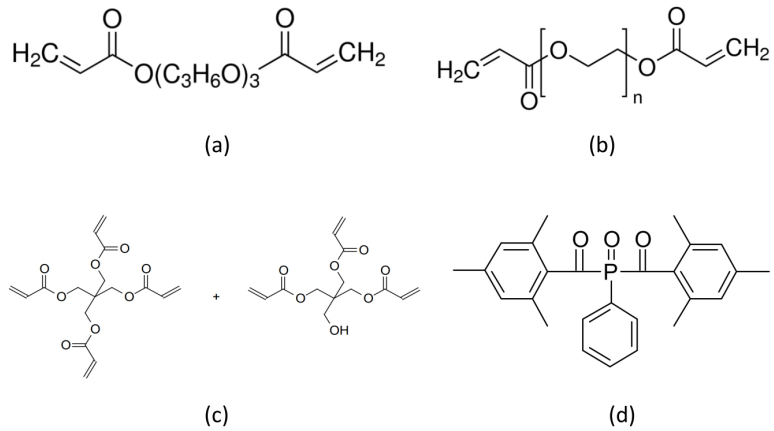

Figure 3.1: The molecular structures of TPGDA (a), PEGDA (b), PETIA (c) and Irgacure 819 (d) applied within the project to develop different custom-made negative photoresists.

It is worth noting that TPGDA, PEGDA and PETIA can be polymerized by free radicals during the 3D printing process. The formulation of each custom photoresist comprising monomers and the photoinitiator concentration in parts per hundred resin (phr.) is summarized in Table 3.1.

Photoresist	Monomer	Photoinitiator (phr.)
TPGDA	TPGDA	Irgacure 819 (0.1)
PEGDA	PEGDA	Irgacure 819 (0.5)
PETIA (a)	PETIA	Irgacure 819 (0.1)
PETIA (b)	PETIA	Irgacure 819 (0.2)
PETIA (c)	PETIA	Irgacure 819 (0.5)
PETIA (d)	PETIA	Irgacure 819 (1)
PETIA (e)	PETIA	Irgacure 819 (2)

Table 3.1: Chemical composition of employed custom photoresists comprising monomers and photoinitiators (phr.).

3.2 Laser setup

Having a powerful TPP setup is a critical requirement for the successful fabrication of complex functional microscale structures. A custom built TPP setup, shown in Figure 3.2, was employed for microfabrication without the need for clean room facilities. For safety, the setup was housed inside an aluminium cabinet equipped with an interlock system that automatically switched the laser off when the door was opened. The cabinet also prevented undesirable light sources such as direct sunlight or ambient light from reaching the photosensitive material, thus avoiding uncontrolled polymerization.

Figure 3.2: A photograph of the laser source and instruments employed for microfabrication via TPP.

A review of the literature reveals that TPP setups differ from one lab to another depending on the application; however, most components are quite similar in the majority of laboratories. Common elements include an ultrashort pulsed laser source (femtosecond laser), high precision stages and powerful objective lenses. Figure 3.3

shows some of the most important components employed within this work, which are as follows:

1. An ultrashort pulsed laser source,
2. A shutter,
3. Motorized attenuators,
4. A polarizer rotator,
5. A non-linear crystal,
6. High-precision stages,
7. An objective lens.

Figure 3.3: Photograph of custom-built TPP setup.

A schematic representation of the experimental setup is shown in Figure 3.4, where infrared (IR) or green laser beams can be used depending on the desired structure. Within the present work, the green laser beam was employed.

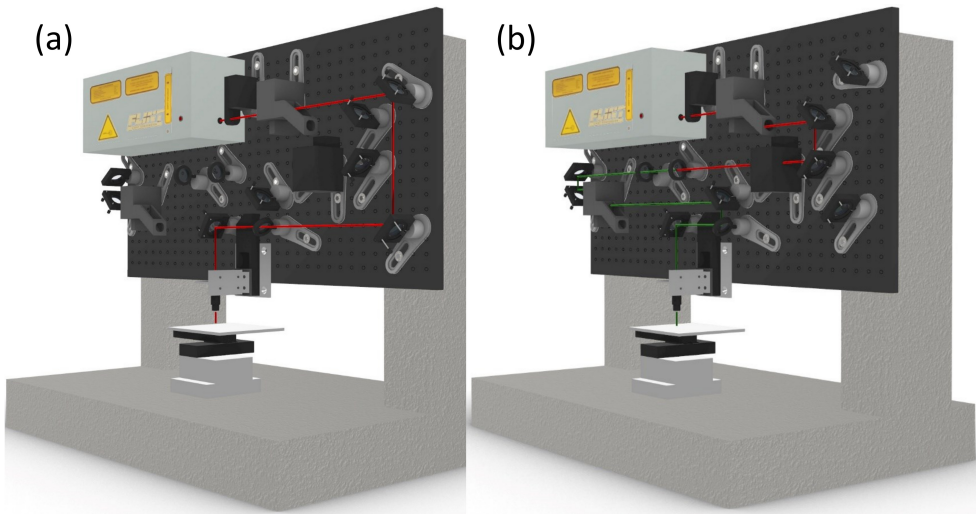

Figure 3.4: CAD drawing of TPP Setup for TPP microfabrication using IR (a) and green (b) femtosecond laser beam.

A FLINT (Light Conversion, Lithuania) Ytterbium-doped Potassium Gadolinium Tungstate (Yb:KGW) ultrashort pulsed laser source was employed to generate pulses of duration 80 fs, energy 70 nJ and peak power 100 kW. The repetition rate and operating wavelength were 76 MHz and 1030 nm, respectively, with the latter frequency doubled to 515 nm with a maximum pulse energy of 25 nJ. A shutter was employed to control exposure of the resin by allowing passage of the laser beam via a control signal provided through computer software. The average laser power and pulse energy transmitted to the working area were controlled by motorized attenuators comprising rotating waveplates and polarizers. A nonlinear optical (NLO) crystal (Altechna, Lithuania) was employed for frequency conversion of high intensity laser radiation. This element was an essential component for the generation of green laser radiation through optical nonlinearities, appropriate for achieving TPA by the employed

photoresists. The average laser power was calibrated with a Gentec-EO MAESTRO power meter, shown in Figure 3.5. The positioning system consisted of three Aerotech linear motorized stages controlled via computer software programmed in G-code. A horizontal platform was mounted on the x- and y-stages, while the focusing lens was mounted on the z-stage. Total travel distance and maximum travel velocity in the x-, y- and z-directions were 25 mm and 2.5 mm/s, respectively. Although the maximum velocity of the mechanical stages was low, they exhibited a high resolution and repeatability of approximately 0.1 μm and ± 0.75 μm as well. $10\times$ and $20\times$ microscope objectives with numerical apertures (NA) of 0.25 and 0.4, respectively, were used to focus the green (515 nm) femtosecond pulsed laser beam inside the photosensitive material, which resulted in TPP and solidification taking place at the focal point. In fact, the green laser beam was tightly focused with 10–$20\times$ objectives to a spot size ranging from approximately 8 μm to 4 μm.

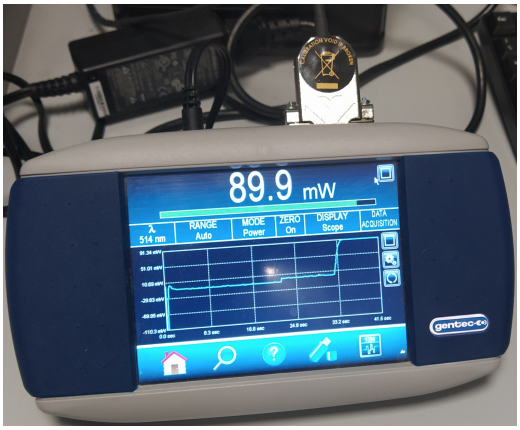

Figure 3.5: Photograph of the power meter employed to monitor and provide accurate average laser power measurements.

3.3 3D printing procedure

Microfabrication via TPP, depicted in Figure 3.6, started with the production of a CAD model of the desired object using SOLIDWORKS (Dassault Systèmes). The CAD model was exported as an STL file and then sliced and hatched with open source software Slic3r. A rectilinear snake-scan pattern with a 90° rotation between layers was applied to fill internal regions. This resulted in an efficient balance of velocity and strength with an automated procedure that could be applied to more complex geometries. Subsequently, the obtained G-code was imported into the Aerotech software, which was responsible for controlling the motorized stages as well as activating the shutter. Material preparation was performed by placing drops of photoresist on a transparent glass substrate mounted on a horizontal platform. Metal washers were utilized to contain the photoresist within a cylindrical volume of height 2 mm and diameter 10 mm on the glass substrate, which was raised 5 mm from the platform to avoid high-intensity reflections from the latter. The laser beam was then focused within the sample to achieve a sufficiently high photon density for TPP of material within the focal volume, namely transformation from a liquid to a solid state via polymerization along the path followed by the focused laser beam. The next step after obtaining the desired microstructures included developing the sample by applying single droplets of solvent to remove unsolidified material. Removing unpolymerized resin without destroying the structure proved to be a significant challenge. After a number of preliminary tests, a mix consisting of 80% isopropyl alcohol with 20% distilled water was found to be the most effective solvent. Finally, an ultraviolet irradiation device was used to provide uniform cross-linking of the developed structure to ensure that it was mechanically stable, leading to emergence of the desired 3D microscale structures on the glass substrate.

With the aim of determining appropriate process parameters for producing the desired 3D microstructure through TPP, several tests were performed to quantify the photosensitive material properties with the employed fabrication setup. As the polymerization threshold is a fixed material-specific value [138], the first fundamental step was to identify the entire range of usable laser power from the polymerization

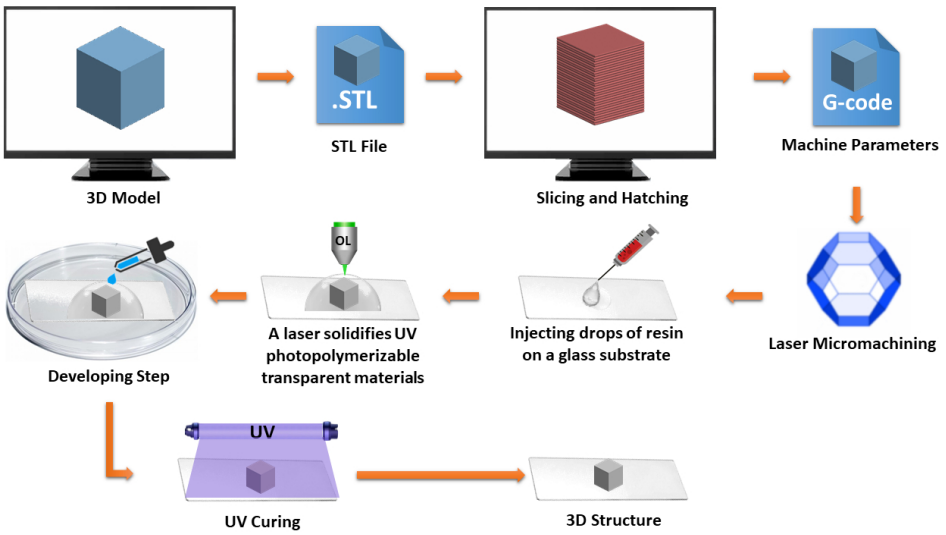

Figure 3.6: Fabrication steps performed to produce 3D microstructures via TPP.

threshold to the damage threshold by producing an array of lines within the resin at a constant scanning speed and applying different values of laser power. A femtosecond laser beam ideally has a Gaussian spatial intensity profile [139], leading to a region in which polymerization takes place without damage. Figure 3.7 shows three Gaussian profiles, below the polymerization threshold, above the threshold and above the damage threshold. Depending on the photoresist, the laser power should lie above the polymerization threshold and below the damage threshold (within the process window [140]) where the material is sufficiently cross-linked for a given scanning speed to enable the production of any desired structure via TPP. The next step after drawing 2D lines within the photoresists was to produce more complex microstructures. In order to reach this goal, small square prisms were produced based on the design in Figure 3.8 (a) by applying different values of laser power at a constant scanning speed of 0.1 mm/s. Finally, after determining the correct balance between laser power and scanning speed for construction of a $0.35 \times 0.35 \times 1$ mm square prism, the height of the structure was reduced to half (0.5 mm) and then a quarter (0.25 mm), as shown in Figure 3.8 (b). The influence of fabrication parameters including the layer height,

defined as the distance between the center of two adjacent lines in the z-direction, and the hatch distance, defined as the distance between the center of two adjacent lines in x- and y-directions, on the structural resolution of rectangular prisms was studied [141, 142]. In order to make a fair comparison between photoresists to choose the most suitable material, the above mentioned steps were employed for all photoresists, which ultimately resulted in the fabrication of complex 3D structures.

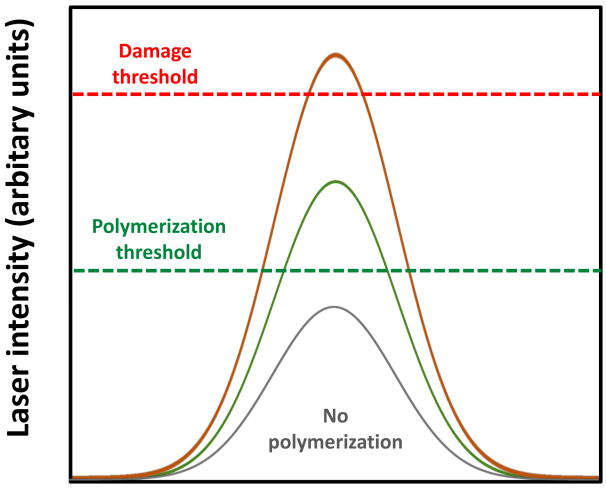

Figure 3.7: Gaussian laser intensity distribution relative to the polymerization and damage thresholds. To achieve high precision 3D microfabrication via TPP, the laser power should lie above the polymerization threshold (green dash line) and below the damage threshold (red dash line).

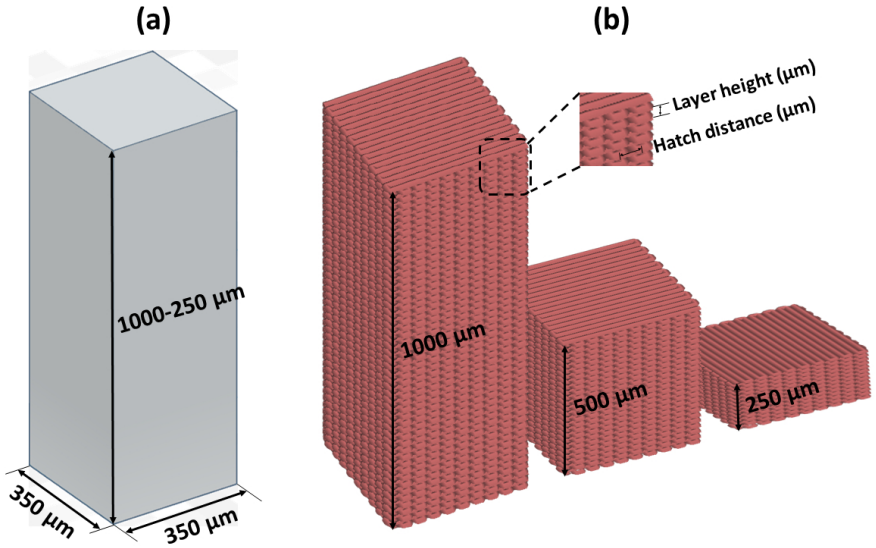

Figure 3.8: 3D microstructure: CAD model (a), slicing and hatching process (b). CAD model line width and thickness not to scale.

Chapter 4

Results and discussion

4.1 femtoBond C

A minimum laser power of 70 mW, the threshold laser power, provided the possibility of transforming femtoBond C from a liquid to a solid state. Below this value, photopolymerization did not occur. Increasing the laser power from 70 mW to 140 mW led to increasingly thick lines and reduction of the space between them. Once a laser power of 140 mW was exceeded, the material started burning. The applied parameters and obtained results with this photoresist are summarized in Table 4.1. A laser

Power (mW)	Objective	Result
<70	10×	No polymerization
=70	10×	Polymerization threshold
>140	10×	Damage threshold
Layer height = 10 μm and hatch distance = 40 μm at scanning speed of 0.1 mm/s		

Table 4.1: TPP fabrication parameters and obtained results relating to femtoBond C.

power of 80 mW was therefore determined to be the best value with a 10× objective at a scanning speed of 0.1 mm/s, which was slightly above the polymerization threshold power for obtaining the smallest voxel size to build the desired structures. After

printing, the structure was placed in 100% 2-Propanol for 90 minutes, a widely used solvent for washing away the unexposed resin without damaging the structure of the exposed region. Although 1-Propanol can be used in place of 2-Propanol for faster development, it entails a higher risk of causing structural damage. As shown in Figure 4.1, the green laser beam creating horizontal lines in the x-direction (first layer) then moved up according to layer height in the z-direction and created more horizontal lines in the y-direction (second layer) to fabricate microscale square prisms.

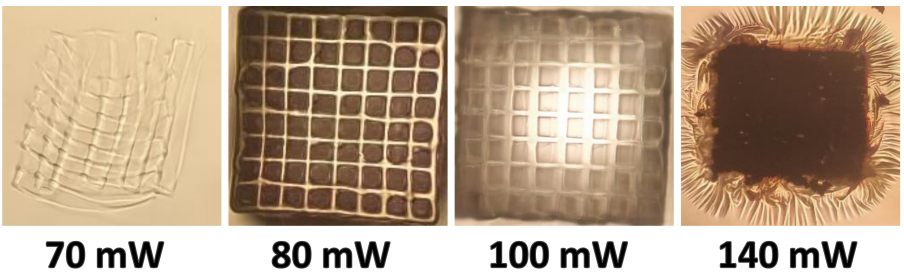

Figure 4.1: Top view of two-photon polymerized woodpile structures made with a 10× objective using femtoBond C photoresist with various laser powers. The layer height, hatch distance and scanning speed were set to 10 μm, 40 μm and 0.1 mm/s, respectively.

The fabricated structures only reached a maximum height of 250 μm, rather than 500 μm and 1000 μm, which represented the main drawback of this organic-inorganic hybrid material. Several approaches were taken in an attempt to overcome this problem, including pre-baking the material to more effectively remove the solvent while precisely controlling the temperature (e.g., 50°C, 60°C and 80°C) and baking time (e.g., 2, 4, 6 and 8 hours), applying different layer heights from 10 μm to 500 μm, increasing the scanning speed from 0.1 mm/s to 0.2 mm/s and using objective lenses with a high numerical aperture such as 0.4 (20×). The layers were basically superimposed while it was not possible to achieve vertical expansion beyond 250 μm. In general, this photoresist exhibited random behaviour requiring many experiments to be performed to achieve a reliable result.

4.2 TPGDA

Figure 4.2 shows microscope images of lines achieved in TPGDA. The laser power had a strong impact on the shape of the polymerized lines. Lines made with lower laser power were wavy and very narrow while those created with higher power were straight and thicker. The applied parameters and obtained results of this photoresist are reported in Table 4.2.

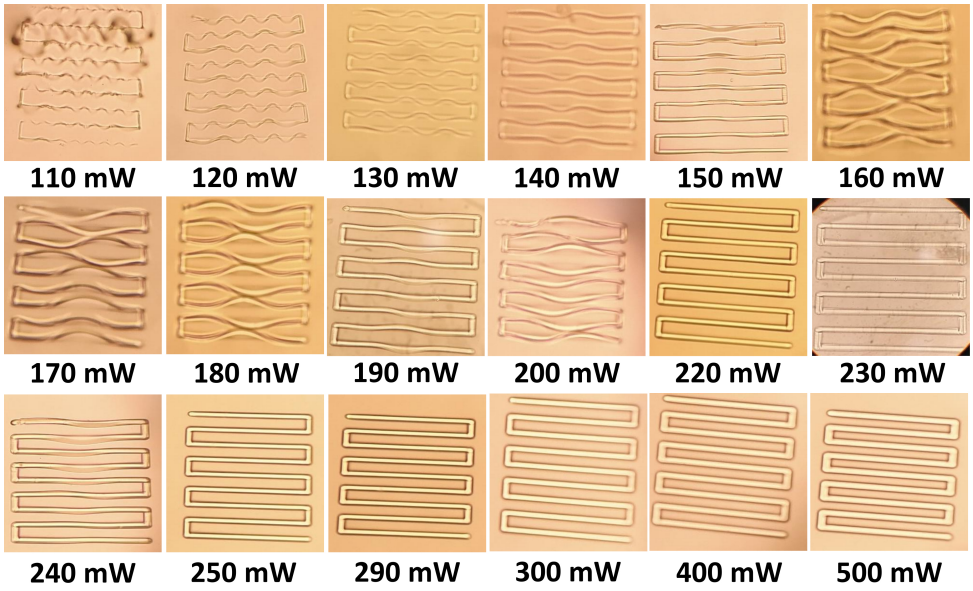

Figure 4.2: Top view of two-photon polymerized lines made with a 10× objective using TPGDA photoresist with various laser powers. The hatch distance and scanning speed were set to 40 μm and 0.1 mm/s, respectively.

The next step after defining the process window was to build woodpile structures obtained by stacking one layer on top of another as shown in Figure 4.3. For power values less than 150 mW, the layers washed away during sample development; however, at higher laser power such as 150 mW, 160 mW and 170 mW the material started burning after approximately 15 layers. Therefore, generated layers at lower values of power were removed after developing while increasing the power led to burning and

Power (mW)	Objective	Result
<110	10×	No polymerization
110-500	10×	Acceptable power
Layer height = 10 μm and hatch distance = 40 μm at scanning speed of 0.1 mm/s		

Table 4.2: TPP fabrication parameters and obtained results for a layer of TPGDA.

subsequently failure of the desired structure. Different solutions were prepared by diluting the solvent with distilled water but this had no observable effect on the final result.

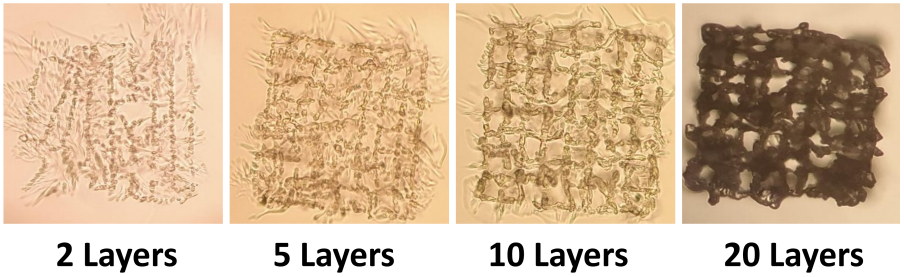

Figure 4.3: Top view of two-photon polymerized woodpile structures made with a 10× objective using TPGDA photoresist with a laser power of 150 mW. The layer height, hatch distance and scanning speed were set to 10 μm, 40 μm and 0.1 mm/s, respectively.

4.3 PEGDA

A minimum laser power of 30 mW with the 10× objective or 15 mW with the 20× objective led to transformation of PEGDA from a liquid to a solid state. By increasing the laser power from 30 mW to 190 mW with the 10× objective or from 15 mW to 60 mW with the 20× objective the space between the lines decreased considerably, which resulted in much thicker lines as shown in Figures 4.4 and 4.5. Once the power exceeded 190 mW with the 10× objective or 60 mW with the 20× objective, this

photoresist started burning. According to the results shown in Table 4.3, objective lenses with a higher NA had a significant influence on the required laser power and polymerization threshold. In this case, the applied laser power with a 20× objective was reduced by half compared that with the 10× objective to minimize the risk of burning the PEGDA.

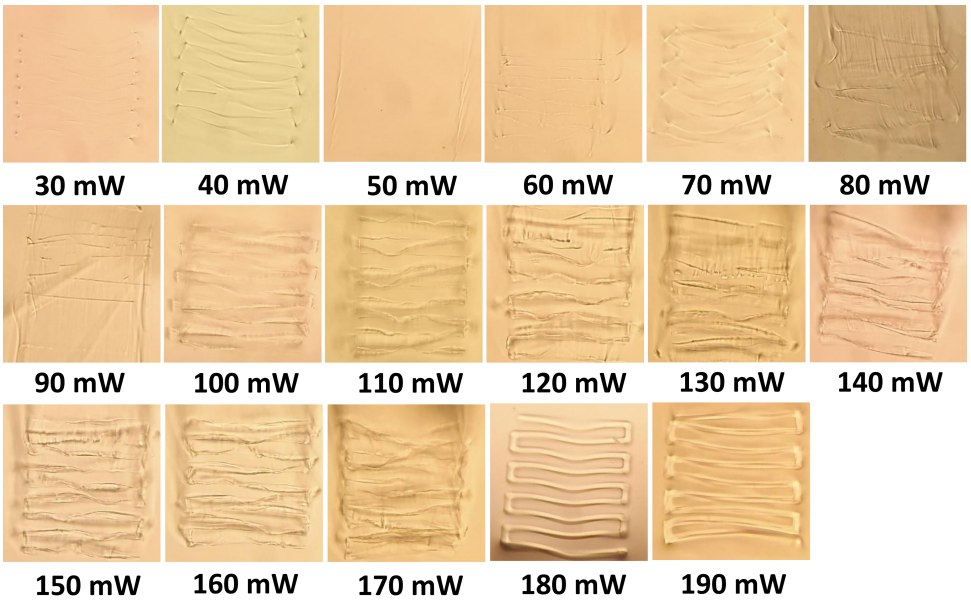

Figure 4.4: Top view of two-photon polymerized micro-lines made with a 10× objective using photoresist PEGDA with various laser powers. The hatch distance and scanning speed were set to 40 μm and 0.1 mm/s, respectively.

Figure 4.6 depicts microscale scaffolds fabricated with a 10× objective consisting of 5 layers with a layer height of 10 μm and a hatch distance of 40 μm. One of the most important challenges related to this photoresist was its high sensitivity to laser power, which increased the height of the fabricated microstructures. For instance, by a applying laser power of 40 mW, the height of the structure reach 1000 μm instead of 50 μm, while by applying lower levels of power such as 30 mW the structure was completely removed during development. By repeating the experiment with a 20× objective, the issue with the height of the built structures remained. Moreover, the

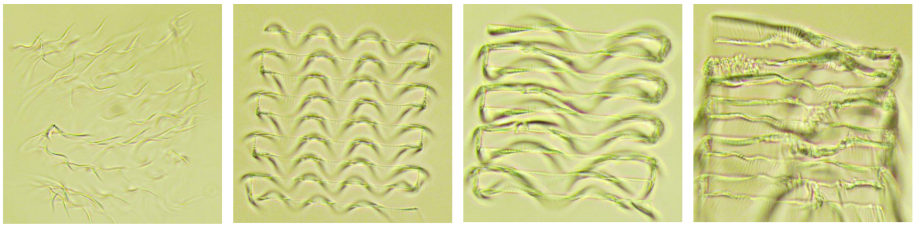

Figure 4.5: Top view of two-photon polymerized woodpile structures made with a 20× objective using PEGDA photoresist with various laser powers. The hatch distance and scanning speed were set to 40 μm and 0.1 mm/s, respectively.

Power (mW)	Objective	Result
<30	10×	No polymerization
30-190	10×	Polymerization threshold
>190	10×	Damage threshold
<15	20×	No polymerization
15	20×	Polymerization threshold
>60	20×	Damage threshold
Layer height = 10 μm and hatch distance = 40 μm at scanning speed of 0.1 mm/s		

Table 4.3: TPP fabrication parameters and obtained results for a layer of PEGDA.

structures were damaged and deformed during sample development. For instance, applying 20 mW and 30 mW led to compressed square prisms during sample development, while by slightly increasing power to 40 mW this issue was not longer present but the desired shape was not achieved, as shown in Figure 4.7.

Based on these results, PEGDA was too sensitive to laser power, starting to burn at very low values of power, which made it almost impossible to achieve the desired structure.

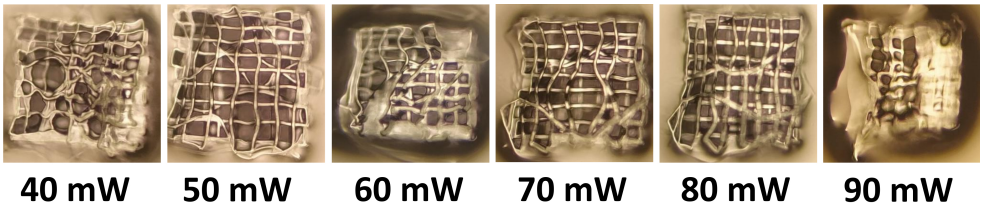

Figure 4.6: Top view of two-photon polymerized woodpile structures made with a 10× objective using PEGDA photoresist with various laser powers. The layer height, hatch distance and scanning speed were set to 10 μm, 40 μm and 0.1 mm/s, respectively.

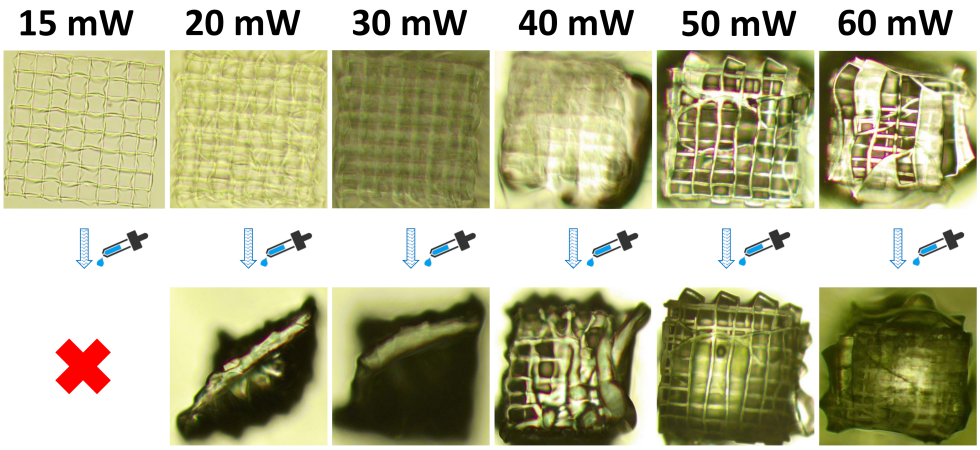

Figure 4.7: Top view of two-photon polymerized woodpile structures made with a 20× objective using PEGDA photoresist with various laser powers. The layer height, hatch distance and scanning speed were set to 10 μm, 40 μm and 0.1 mm/s, respectively.

4.4 E-Shell 300

Due to the fact that a 10× objective required a lot of laser power for E-Shell 300, which increased the chance of burning the material, a 20× objective was used for production of microstructures. The results demonstrated that the threshold power for

both photoresists was 8 mW with the employed experimental setup. Below this value, photopolymerization did not take place, while above this value photopolymerization caused irreversible modification of the material. By increasing the laser power, the width of the lines increased, as shown in Figure 4.8. At very high values (>80 mW @ 0.1 mm/s), E-Shell 300 started burning. Table 4.4 summarizes the applied parameters and obtained results for this material.

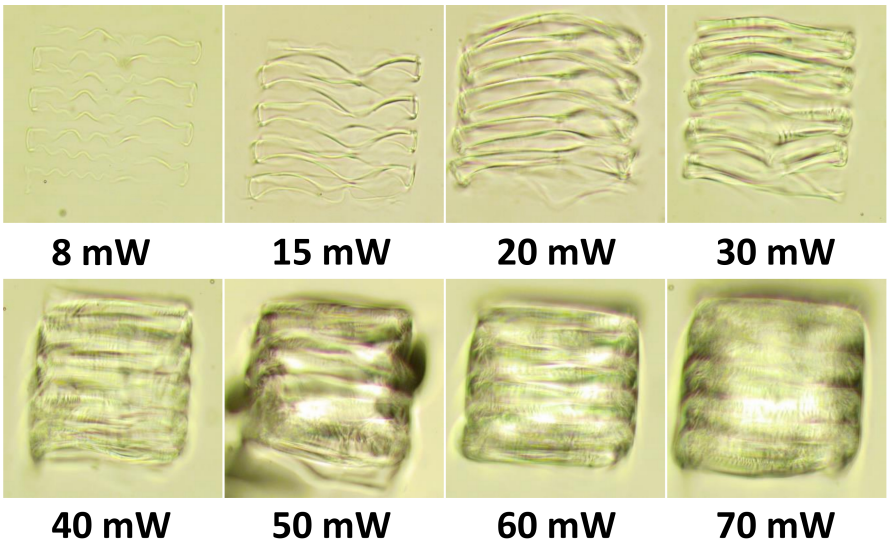

Figure 4.8: Top view of two-photon polymerized micro-lines made with a 20× objective using E-Shell 300 photoresist with various laser powers. The hatch distance and scanning speed were set to 40 μm and 0.1 mm/s, respectively.

Power (mW)	Objective	Result
<8	20×	No polymerization
=8	20×	Polymerization threshold
>80	20×	Damage threshold
Layer height = 10 μm and hatch distance = 40 μm at scanning speed of 0.1 mm/s		

Table 4.4: TPP fabrication parameters and obtained results relating to E-Shell 300.

Laser power levels of 8 mW, 10 mW, 12 mW and 15 mW were therefore found to be most appropriate with a constant scanning speed of 0.1 mm/s, which were slightly above the polymerization threshold for obtaining the smallest voxel size. Other key process parameters such as layer height and hatch distance were then changed to determine their effects on the final quality of the scaffold structures. The resulting structures are shown in Figures 4.9-4.14, with the respective processing parameters and achieved height reported in Tables 4.5-4.10. The main goal of optimizing fabrication parameters was to achieve the desired structure while maintaining precision.

Figure 4.9 shows micro scaffolds produced with a layer height and hatch distance of 10 μm and 40 μm, respectively. Although increasing the laser power from 8 mW to 15 mW resulted in an acceptable form after development, the desired height was not achieved. With a laser power of 8 mW, the height of microstructures reached 500 μm (25 layers), 1000 μm (50 layers) and 1800 μm (100 layers). With a power of 15 mW, the height was instead 1000 μm (25 layers), 1500 μm (50 layers) and 2000 μm (100 layers). These results were beyond the height prescribed within the CAD model: 250 μm (25 layers), 500 μm (50 layers) and 1000 μm (100 layers).

Power (mW)	Height (μm) [25 layers]	Height (μm) [50 layers]	Height (μm) [100 layers]
8	500	1000	1800
10	600	1100	1900
12	980	1250	1980
15	1100	1500	2000
Layer height=10 μm and hatch distance=40 μm at scanning speed of 0.1 mm/s			

Table 4.5: TPP fabrication parameters and obtained results relating to Figure 4.9.

Figure 4.10 presents 3D structures produced with a hatch distance of 40 μm while increasing the layer height from 10 μm to 20 μm. In this case, the form of the fabricated structures was acceptable even at low values of laser power while the structure height improved slightly, especially for 50 layers (50$\times$20 μm) compared to a layer height of 10 μm.

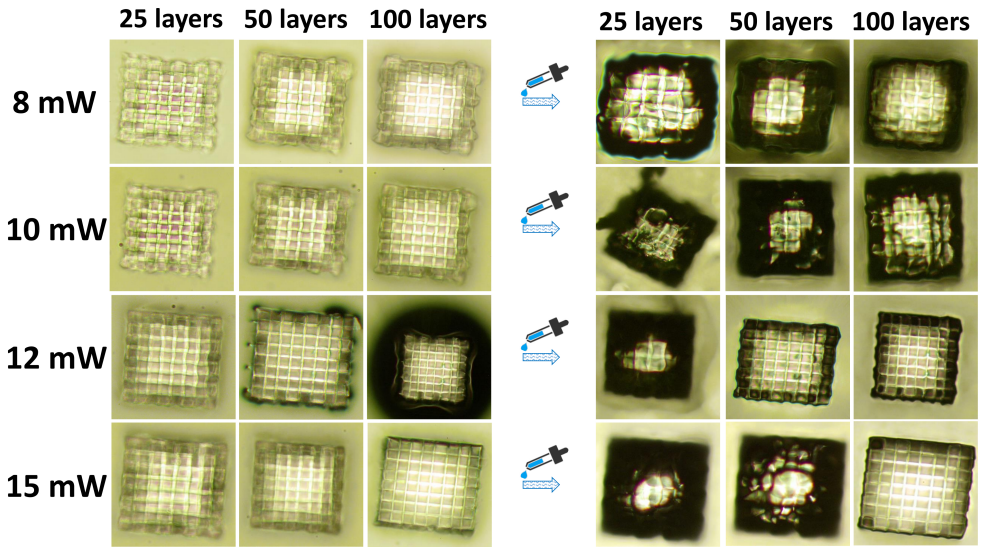

Figure 4.9: Top view of two-photon polymerized woodpile structures made with a 20× objective using E-Shell 300 photoresist with various laser powers. The layer height, hatch distance and scanning speed were set to 10 μm, 40 μm and 0.1 mm/s, respectively.

Power (mW)	Height (μm) [12 layers]	Height (μm) [25 layers]	Height (μm) [50 layers]
8	500	980	1200
10	550	1080	1250
12	945	1205	1465
15	1000	1223	1500
Layer height=20 μm and hatch distance=40 μm at scanning speed of 0.1 mm/s			

Table 4.6: TPP fabrication parameters and obtained results relating to Figure 4.10.

By setting the hatch distance constant and increasing the layer height to 30 μm, as shown in Figure 4.11, the edges of the fabricated structures lost the correct form when lower values of power were applied; however, by applying laser powers of 12

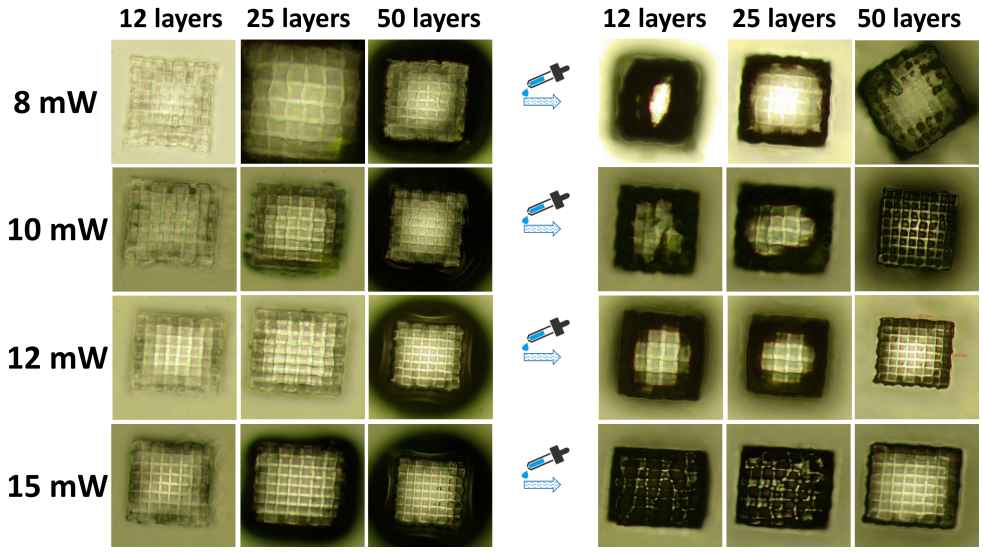

Figure 4.10: Top view of two-photon polymerized woodpile structures made with a 20× objective using E-Shell 300 photoresist with various laser powers. The layer height, hatch distance and scanning speed were set to 20 μm, 40 μm and 0.1 mm/s, respectively.

mW and 15 mW, the desired shape was obtained.

Figure 4.12 displays results achieved with an increase in layer height from 30 μm to 40 μm with a hatch distance of 40 μm. A laser power of 8 mW was inappropriate for the whole structure to be fully polymerized. By increasing laser power, although the structures tended to remain on the glass substrate, their form was still unacceptable during sample development.

Microstructures shown in Figure 4.13 were created by increasing the layer height from 50 μm to 80 μm at a laser power of 12 mW and a hatch distance of 40 μm. During the developing process with 2-Propanol, the edges of fabricated structures lost their square shape and became more rounded; however, no improvement in height was achieved, as presented in Table 4.9.

As a final test performed on this photoresist, the effect of increasing scanning speed from 0.2 to 2 mm/s at a constant laser power of 12 mW was investigated. Ac-

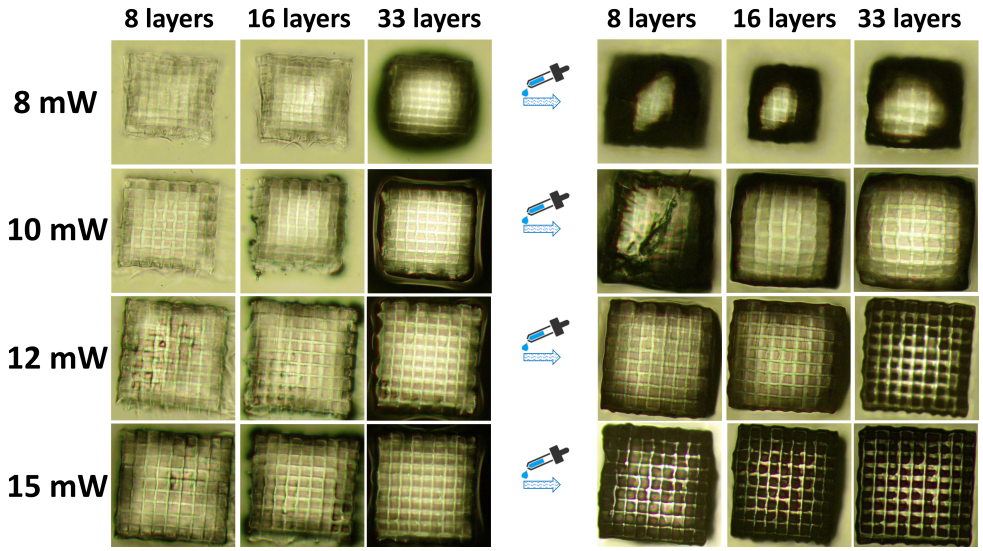

Figure 4.11: Top view of two-photon polymerized woodpile structures made with a 20× objective using E-Shell 300 photoresist with various laser powers. The layer height, hatch distance and scanning speed were set to 30 μm, 40 μm and 0.1 mm/s, respectively.

power (mW)	Height (μm) [8 layers]	Height (μm) [16 layers]	Height (μm) [33 layers]
8	800	1000	1400
10	865	1020	1500
12	988	1100	1800
15	1121	1200	2000
Layer height=30 μm and hatch distance=40 μm at scanning speed of 0.1 mm/s			

Table 4.7: TPP fabrication parameters and obtained results relating to Figure 4.11.

cording to the obtained results, shown in Figure 4.14 and Table 4.10, increasing the scanning speed resulted in lower mechanical strength of the fabricated microstructures due to insufficient laser exposure to polymerize the liquid monomers into insol-

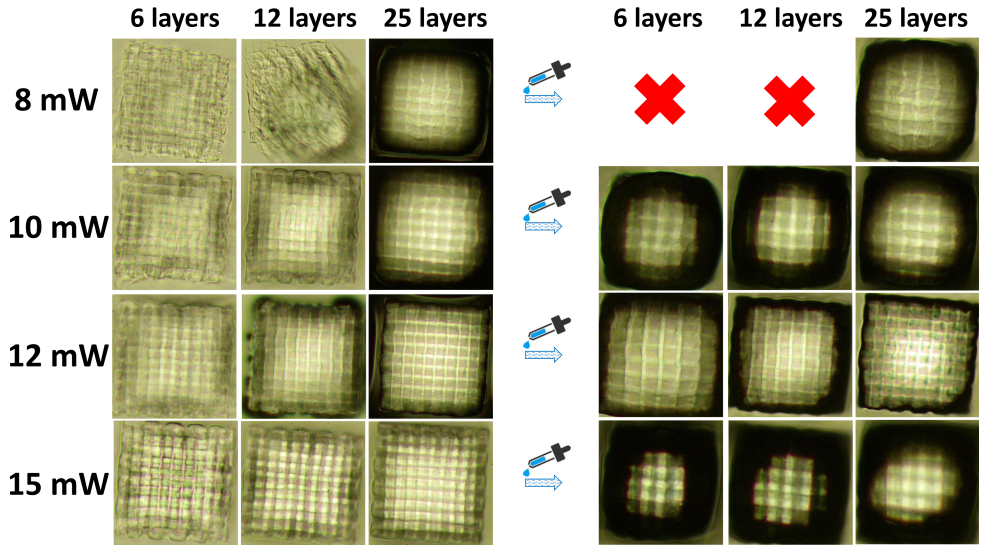

Figure 4.12: Top view of two-photon polymerized woodpile structures made with a 20× objective using E-Shell 300 photoresist with various laser powers. The layer height, hatch distance and scanning speed were set to 40 μm, 40 μm and 0.1 mm/s, respectively.

power (mW)	Height (μm) [6 layers]	Height (μm) [12 layers]	Height (μm) [25 layers]
8	Removed	Removed	1500
10	900	1100	1700
12	1000	1180	1800
15	1122	1223	1825
Layer height=40 μm and hatch distance=40 μm at scanning speed of 0.1 mm/s			

Table 4.8: TPP fabrication parameters and obtained results relating to Figure 4.12.

uble cross-linked network polymers. For instance, structures made at speeds of 1 and 2 mm/s suffered significantly from damage during sample development compared to structures made at lower speeds such as 0.2 mm/s, with unwanted deformation more

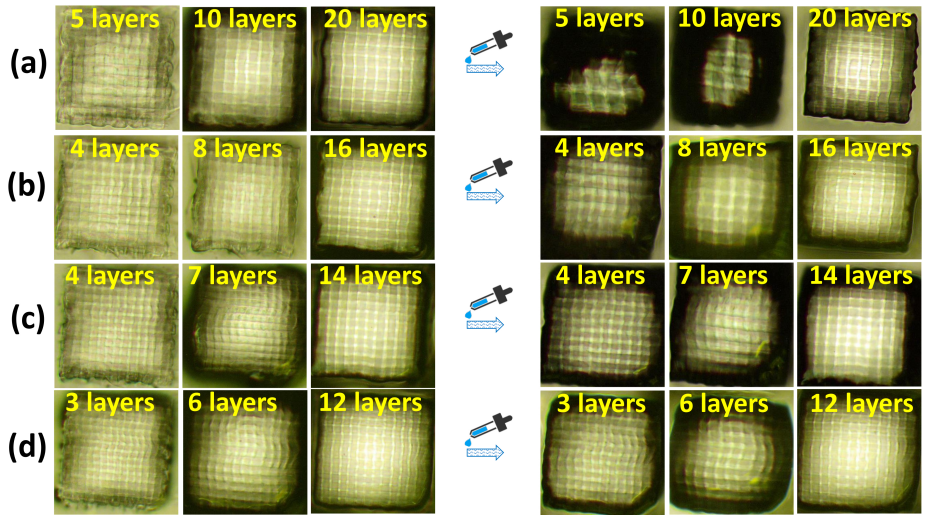

Figure 4.13: Top view of two-photon polymerized woodpile microstructures made with various layer heights of 50 μm (a), 60 μm (b), 70 μm (c) and 80 μm (d) as well as hatch distances of 40 μm fabricated, laser power of 12 mW with E-Shell 300 photoresist.

visible with 25 and 50 layers. Furthermore, increasing the speed did not result in improved outcomes in terms of desired height or structural resolution.

It was therefore determined that fabrication parameters including average laser power, scanning speed, layer height and hatch distance directly influenced the microstructure quality achieved with E-Shell 300. However, reaching the desired height, especially when this was less than 500 μm, remained impossible. Moreover, experimental results demonstrated that applying a lower laser power at higher scanning speed leads to both poor structural integrity and undesired quality during sample development.

Layer height (μm)	Height (μm) 5 layers 10 layers 20 layers	Height (μm) 4 layers 8 layers 16 layers	Height (μm) 4 layers 7 layers 14 layers	Height (μm) 3 layers 6 layers 12 layers
50 (a)	850			
//	1050			
//	1500			
60 (b)		900		
//		1100		
//		1600		
70 (c)			1000	
//			1200	
//			1500	
80 (d)				1000
//				1200
//				1600
Laser power of 12 mW and hatch distance of 40 μm at scanning speed of 0.1 mm/s				

Table 4.9: TPP fabrication parameters and obtained results relating to Figure 4.13.

4.5 PETIA

In the following section, five different compositions of PETIA were investigated. In fact, the effect of various photoinitiator concentrations (0.1, 0.2, 0.5, 1 and 2 phr.) on the threshold laser power as well and the resulting fabricated structures was comprehensively studied in order to choose the most suitable photoresist for the TPP setup. Detail information about this photosensitive material and the various compositions employed, including PETIA (a), PETIA (b), PETIA (c), PETIA (d) and PETIA (e), have been presented in Chapter 3.

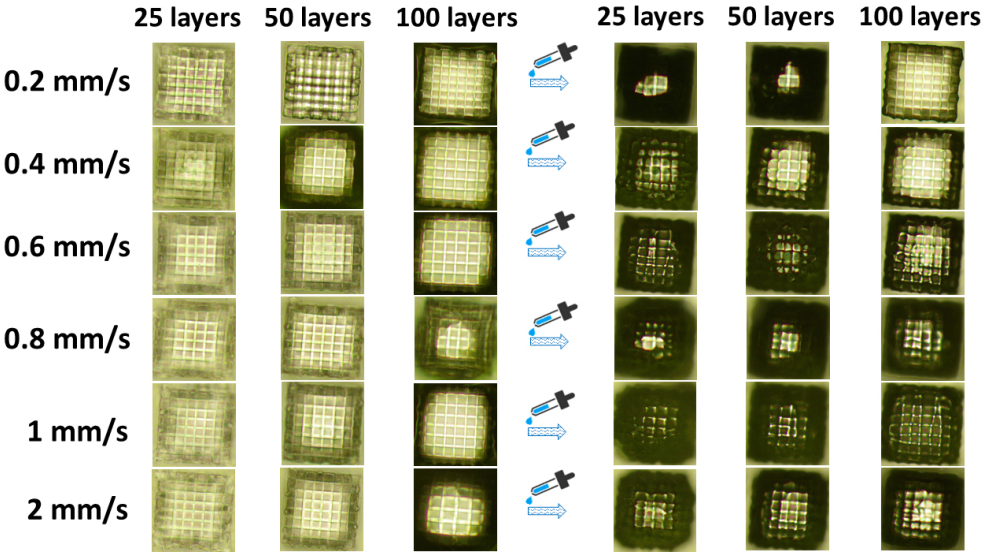

Figure 4.14: Top view of two-photon polymerized woodpile structures made with a 20× objective using E-Shell 300 photoresist with a laser power of 12 mW and various scanning speeds. The layer height, hatch distance and scanning speed were set to 10 μm and 40 μm, respectively.

power (mW)	Speed (mm/s)	Height (μm) [25 layers]	Height (μm) [50 layers]	Height (μm) [100 layers]
12	0.2	800	1000	1400
12	0.4	970	1230	1700
12	0.6	1000	1200	1500
12	0.8	800	1120	1800
12	1	860	1200	1700
12	2	750	1120	1550
Layer height=10 μm and hatch distance=40 μm				

Table 4.10: TPP fabrication parameters and obtained results relating to the Figure 4.14.

4.5.1 PETIA (a)

The polymerization threshold of PETIA (a) was determined to be 12 mW. As shown in Figure 4.15, simple lines were drawn within this photoresist applying power ranging from 12 mW to 69 mW. The material started burning with a power of 70 mW at a constant scanning speed of 0.1 mm/s, as reported in Table 4.11.

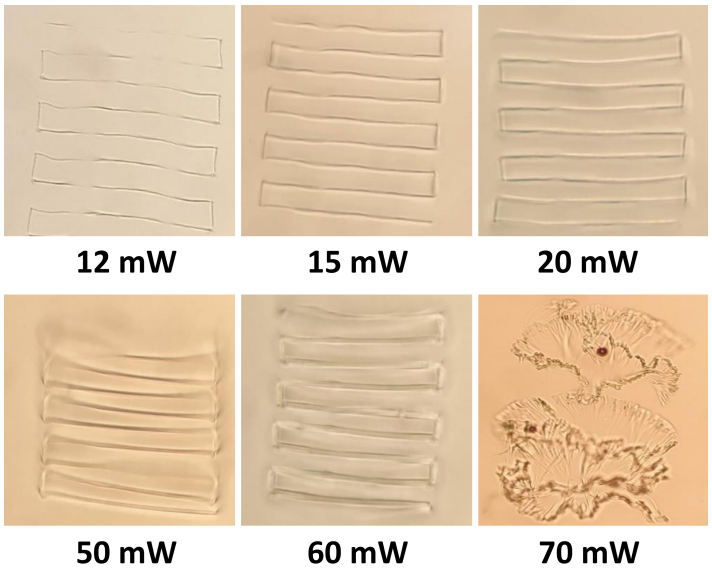

Figure 4.15: Top view of two-photon polymerized micro-lines made with a 20× objective using PETIA (a) photoresist with various laser powers. The hatch distance and scanning speed were set to 40 μm and 0.1 mm/s, respectively.

After performing several tests, the main issue that emerged was transformation of the built scaffold structures. Figure 4.16 depicts woodpile structures created with various laser powers with a layer height of 10 μm and a hatch distance of 40 μm at a constant velocity of 0.1 mm/s. In this case, sample development caused increased structural shrinkage. Obtaining the desired microstructure form was therefore impossible. It should be noted that altering fabrication parameters such as increasing the laser power and scanning speed, adjusting the values of layer height and hatch dis-

Power (mW)	Objective	Result
<12	20×	No polymerization
12	20×	Polymerization threshold
>69	20×	Damage threshold
Layer height = 10 μm and hatch distance = 40 μm at scanning speed of 0.1 mm/s		

Table 4.11: TPP fabrication parameters and the obtained results for a layer of PETIA (a).

tance were found to be ineffective. Moreover, using weaker solvents including a mix consisting 60% isopropyl alcohol with 40% distilled water or 50% ethanol with 50% distilled water had no effect on the final result.

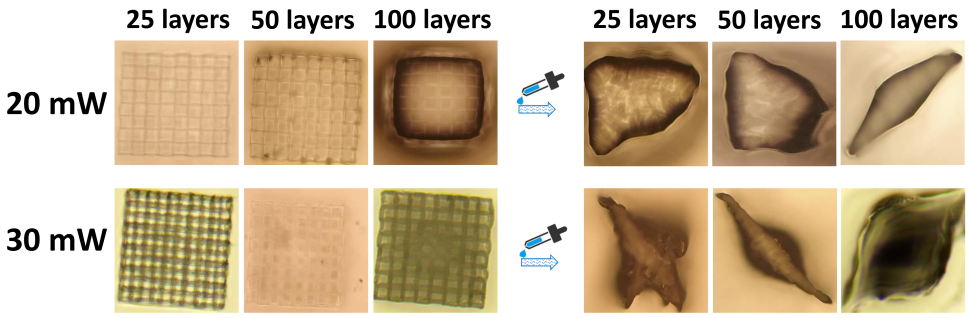

Figure 4.16: Top view of two-photon polymerized woodpile structures made with a 20× objective using PETIA (a) photoresist with various laser powers. The layer height, hatch distance and scanning speed were set to 10 μm, 40 μm and 0.1 mm/s, respectively.

4.5.2 PETIA (c)

Arrays of lines were drawn within PETIA (c) with different values of laser power at a constant scanning speed of 0.1 mm/s, from a minimum laser power of 3 mW to a maximum power of 110 mW, as shown in Figure 4.17. According to Table 4.12, the results demonstrated that the threshold power for this photoresist was 3 mW while

by increasing the laser power, the width of the lines increased. However, at very high values (>109 mW) the material began burning. As shown in Figure 4.18, this photoresist behaved much like PETIA (a) and therefore the main challenge was again obtaining the desired form after developing, which was not possible. It is also worth noting that for both PETIA (a) and PETIA (c), a hatch rotation angle of 45 degrees, as shown in Figure 4.19, was applied to fill the area with a rectilinear pattern in order to produce stronger microstructures. Although the mechanical strength of the fabricated structures improved slightly as a result of this change, this improvement was still insufficient to achieve the desired shape. In comparison to PETIA (a), PETIA (c) demonstrated greater resistance to the applied solvents and a better result was achieved.

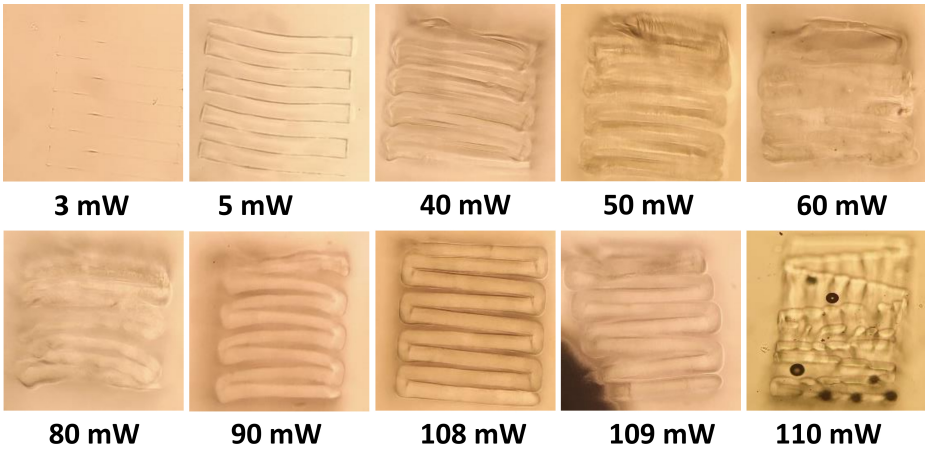

Figure 4.17: Top view of two-photon polymerized micro-lines made with a 20× objective using PETIA (c) photoresist with various laser powers. The hatch distance and scanning speed were set to 40 μm and 0.1 mm/s, respectively.

4.5.3 PETIA (d)

PETIA (d), which contained a higher concentration of photoinitiator, required only 2 mW of laser power to polymerize, as shown in Figure 4.20. It also demonstrated

Power (mW)	Objective	Result
<3	20×	No polymerization
3	20×	Polymerization threshold
>109	20×	Damage threshold
Layer height = 10 μm and hatch distance = 40 μm at scanning speed of 0.1 mm/s		

Table 4.12: TPP fabrication parameters and the obtained results for a layer of PETIA (c).

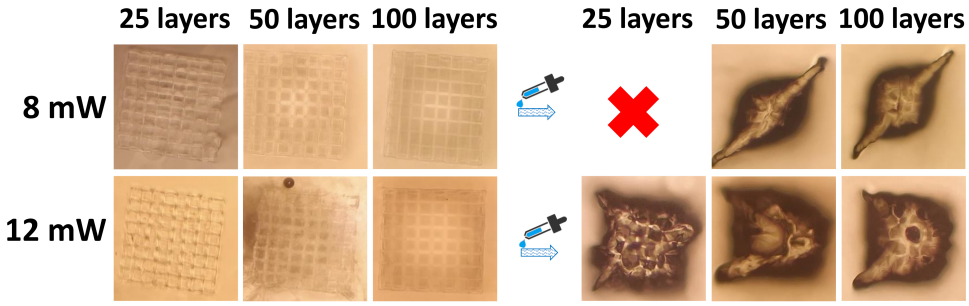

Figure 4.18: Microscope image of two-photon polymerized woodpile microstructures with various powers fabricated with a 20× objective from a negative-tone photoresist PETIA (c). The layer height, hatch distance and scanning speed were set to 10 μm, 40 μm and 0.1 mm/s, respectively.

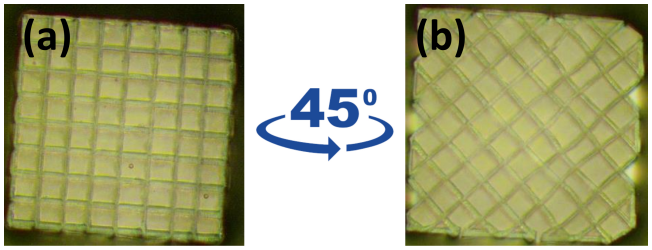

Figure 4.19: Hatch pattern (a) was used in this experiment, rotated by 45 degrees (b) to create micro-lines within PETIA (c).

greater resistance to high levels of power, such as 200 mW at a constant scanning speed of 0.1 mm/s, without causing damage or burning, as reported in Table 4.13. Figure 4.21 depicts square prisms obtained with a layer height of 10 μm, hatch distance of 40 μm, laser power of 10 mW and scanning speed of 0.1 mm/s. Most significantly, effective removal of the unexposed resin with various solvents including 1-Propanol, 2-Propanol, acetone and ethanol was not possible.

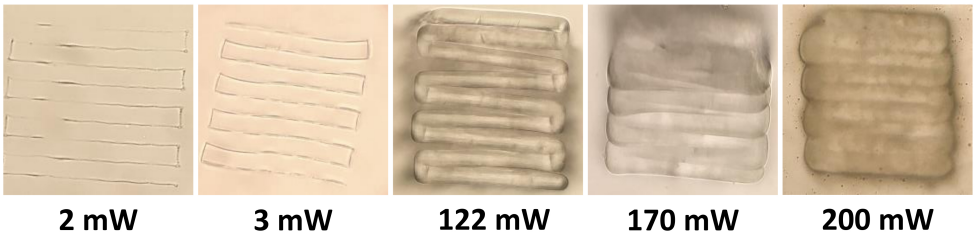

Figure 4.20: Top view of two-photon polymerized micro-lines made with a 20× objective using PETIA (d) photoresist with various laser powers. The hatch distance and scanning speed were set to 40 μm and 0.1 mm/s, respectively.

Power (mW)	Objective	Result
<2	20×	No polymerization
2-200	20×	Acceptable powers
Layer height = 10 μm and hatch distance = 40 μm at scanning speed of 0.1 mm/s		

Table 4.13: TPP fabrication parameters and the obtained results for a layer of PETIA (d).

4.5.4 PETIA (e)

As shown in Figure 4.22 and Table 4.14, by applying laser power ranging from 3 mW to 200 mW with a 20× objective, the micro-lines were drawn within PETIA (e). The main challenge with this material was removing the unpolymerized resin after sample development. Even following immersion in solvent for three days, the

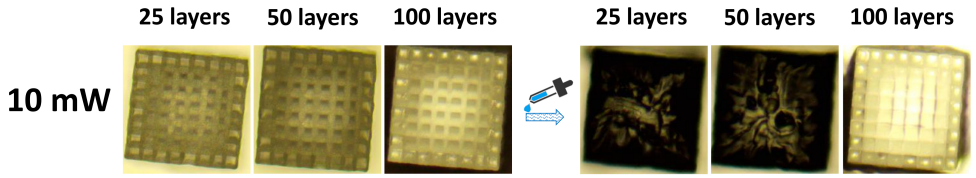

Figure 4.21: Top view of two-photon polymerized woodpile structures made with a 20× objective using PETIA (d) photoresist with various laser powers. The layer height, hatch distance and scanning speed were set to 10 μm, 40 μm and 0.1 mm/s, respectively.

unpolymerized material remained stuck so tightly to the produced part that it was impossible to separate them, as shown in Figure 4.23.

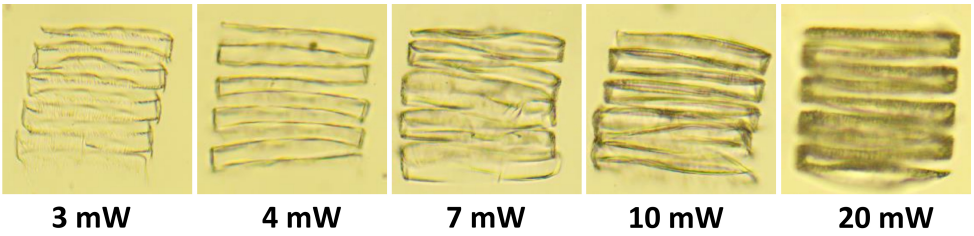

Figure 4.22: Top view of two-photon polymerized micro-lines made with a 20× objective using PETIA (e) photoresist with various laser powers. The hatch distance and scanning speed were set to 40 μm and 0.1 mm/s, respectively.

Power (mW)	Objective	Result
<3	20×	No polymerization
3-200	20×	Acceptable powers
Layer height = 10 μm and hatch distance = 40 μm at scanning speed of 0.1 mm/s		

Table 4.14: TPP fabrication parameters and the obtained results for a layer of PETIA (e).

It should be noted that the fabricated structures with PETIA (d) and PETIA (e)

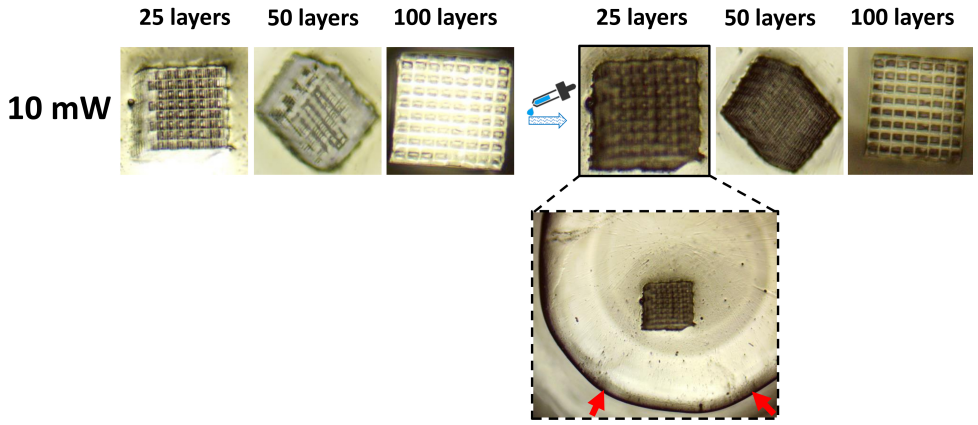

Figure 4.23: Top view of two-photon polymerized woodpile structures made with a 20× objective using PETIA (e) photoresist with various laser powers. The layer height, hatch distance and scanning speed were set to 10 μm, 40 μm and 0.1 mm/s, respectively.

demonstrated greater physical strength than PETIA (a) and PETIA (c). Achieving the desired structure was therefore possible; however, the problem regarding reaching the desired height still persisted.

4.5.5 PETIA (b)

The final and most suitable photoresist was PETIA (b). A minimum laser power of 7 mW provided the possibility of transforming this resin from a liquid to a solid state, as presented in Figure 4.24. The applied processing parameters and results are summarized in Table 4.15. Increasing the laser power from 7 mW to 80 mW led to increasingly thick lines and a reduction in space between them. Once the laser power exceeded 70 mW, the PETIA (b) started burning, as shown in Figure 4.25. This SEM image depicts a series of lines suspended between two supporting blocks. In the specific example presented in the figure, the minimum applied laser power was 20 mW, above the threshold value of 7 mW due to difficulty in preserving the manufactured lines after the developing process at lower laser power.

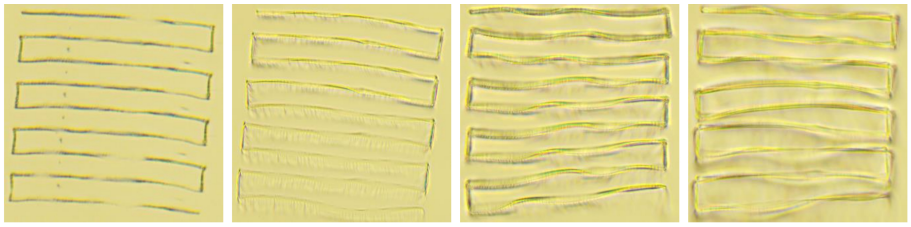

Figure 4.24: Top view of two-photon polymerized micro-lines made with a 20× objective using PETIA (b) photoresist with various laser powers. The hatch distance and scanning speed were set to 40 μm and 0.1 mm/s, respectively.

Power (mW)	Objective	Result
<7	20×	No polymerization
7	20×	Polymerization threshold
>69	20×	Damage threshold
Layer height = 10 μm and hatch distance = 40 μm at scanning speed of 0.1 mm/s		

Table 4.15: TPP fabrication parameters and the obtained results for a layer of PETIA (b).

The TPP resolution or voxel size can also be determined through this method. Figure 4.26 shows the effect of the laser power on the line width with a scanning speed of 0.1 mm/s. As can be observed, by increasing the laser power, the width of the lines increases from 2.668 μm at 20 mW to 9.827 μm at 80 mW, which means that the voxel dimension is affected by the combination of laser power and scanning speed. Therefore, it is important to provide precise control over the above-mentioned parameters to achieve the desired quality. Higher levels of laser power can be selected for faster fabrication of structures with less precision, while lower values are more appropriate for ultraprecise structures.

After performing several tests, 12 mW was selected as the best value of laser power, which was slightly above the polymerization threshold required to generate the necessary free radicals while maintaining the scanning speed constant at 0.1

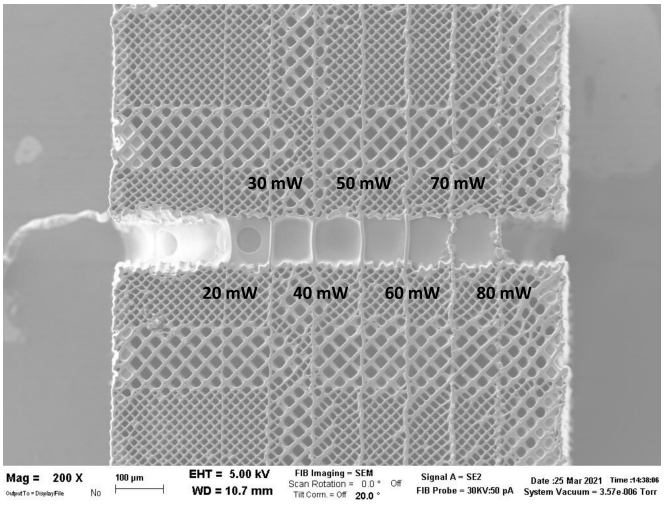

Figure 4.25: Scanning electron microscopy (SEM) image of lines made with different values of laser power at a constant velocity of 0.1 mm/s where the horizontal distance between the lines was 100 μm. Lines were suspended between two supporting blocks above and below the central region.

mm/s. Figure 4.27 presents produced woodpile microstructures with the layer height and hatch distance both equal to 10 μm, a laser power of 12 mW and a scanning speed of 0.1 mm/s. The height of structures was 330 μm and 640 μm for 25 and 50 layers, respectively, which was beyond the heights prescribed within the CAD model, namely 250 μm and 500 μm. It should be noted that for the first time the height of produced structures was less than 500 μm, which was impossible to achieve with other photoresists. By using a layer height of 40 μm and a hatch distance of 20 μm, the minimum height of 250 μm was achieved but with an undesirable microstructure shape due to the lower physical strength of the structure.

To summarize the main points, PETIA (b) in comparison to other photoresists including femtoBond C, TPGDA, PEGDA, E-Shell 300, as well as PETIA (a,c,d,e), showed considerable potential in reaching the pre-design microstructure; however, it exhibited a high level of sensitivity to the incident laser beam.

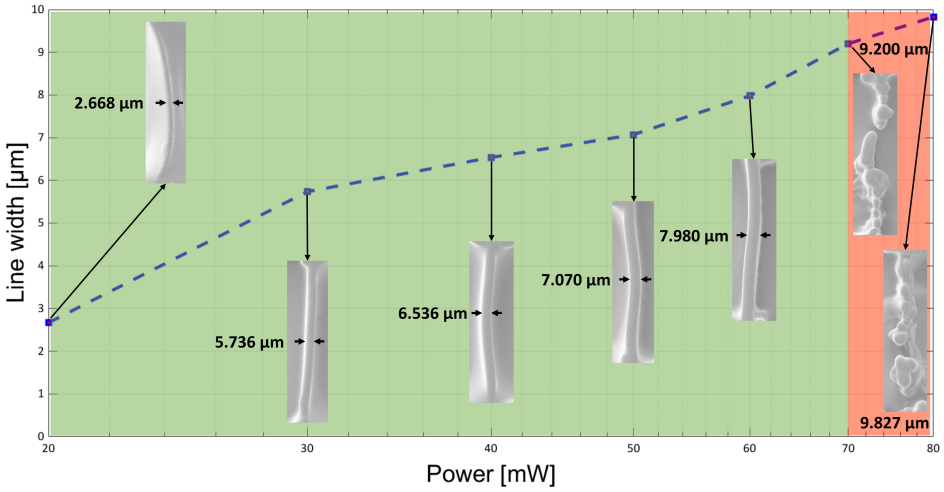

Figure 4.26: Experimentally measured line width as a function of average laser power at 0.1 mm/s for PETIA (b) resin where green indicates the processing window and orange the damaged zone.

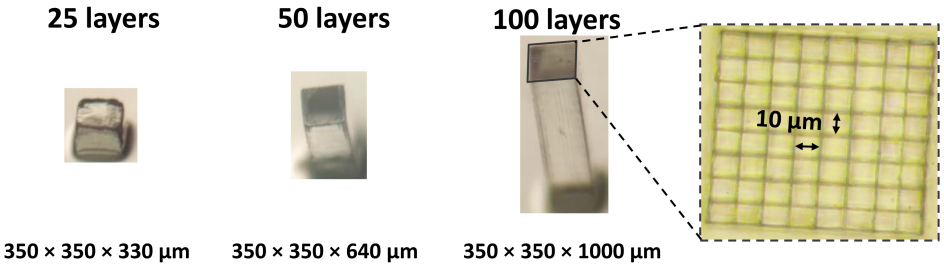

Figure 4.27: Two-photon polymerized woodpile microstructures with various heights from 330 μm to 1000 μm made with a 20× objective using PETIA (b) photoresist.

Chapter 5

Fabrication of microneedle arrays

Microneedles (MNs), comprising sub-millimeter needles positioned on a baseplate, have attracted remarkable attention over recent decades [143, 144] due to their advantages such as painless injection by avoiding contact with nerve endings [145] and limited requirements for medical expertise due to their simple application [146]. A broad range of materials (e.g., modified ceramics, inorganic-organic hybrid polymers, acrylate-based polymers or water-soluble materials) and geometries (e.g., conical, pyramidal, pentagonal, hexagonal, octagonal and canonical) have been used to produce MNs through TPP [147, 148]. MN devices are generally classified as coated, dissolving, hollow or solid according to their specific design and application. Coated MNs, as shown in Figure 5.1 (a), are primarily used to puncture the skin in order to deliver drugs where the maximum dosage is less than one milligram. Coating is achieved via dipping or spraying the MNs with a viscous aqueous solution. The maximum achievable dosage is in fact the main drawback of this type of MN. Figure 5.1 (b) shows painless dissolving MNs made of safe materials including biodegradable polymers or natural polymers that control the release of drugs or vaccines integrated into the applied materials. The main issues related to the fabrication of dissolving MNs include high cost and a very time consuming process. Hollow MNs (Figure 5.1 (c)) not only deliver drugs at higher doses, but can also transport a wide range of molecules during tissue fluid extraction, which has attracted the interest of many

researchers. However, because of insufficient mechanical strength, hollow MNs are frequently prone to fracture [149].

Solid MNs have proven to be one of the most effective ways to deliver diverse molecules including insulin, calcein, naltrexone and proteins into the human body [150]. Within this context, the main purpose of the present research is to improve the fabrication resolution and production time of solid MNs, which are mostly used to create micro-pores in human skin and facilitate absorption of pharmaceutical formulations such as solutions, creams or gels [151] through the creation of channels, as shown in Figure 5.1 (d), while reducing pain, injury and recovery time.

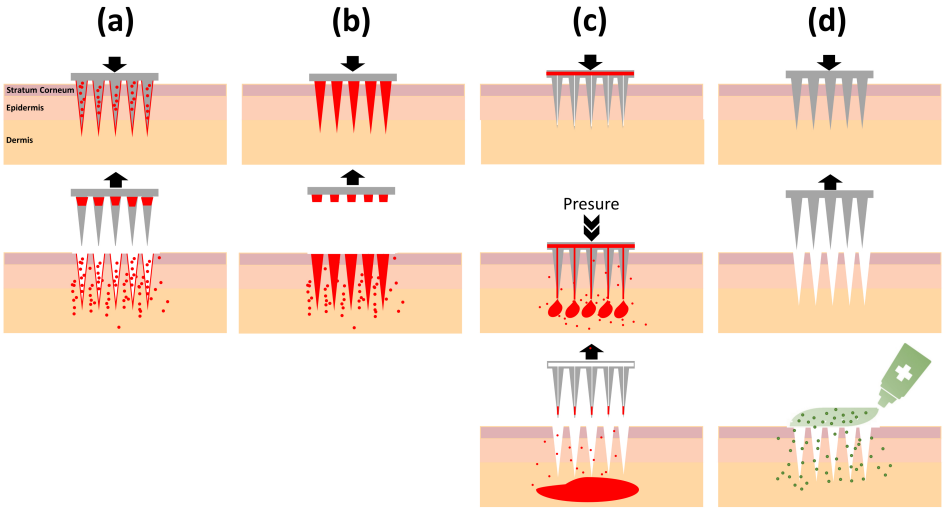

Figure 5.1: A schematic of four different microneedle types: Coated (a), dissolving (b), hollow (c) and solid (d) MNs used for drug delivery to the skin [9].

5.1 Experimental results and discussion

After successfully producing the small square prisms from PETIA (b), the next step was the fabrication of ultraprecise solid MNs with 49 conical needles arranged in a 7×7 configuration comprising cones with a base diameter of 250 μm, tip diameter of 30 μm, height of 800 μm and pitch of 500 μm [152], as depicted in Figure 5.2.

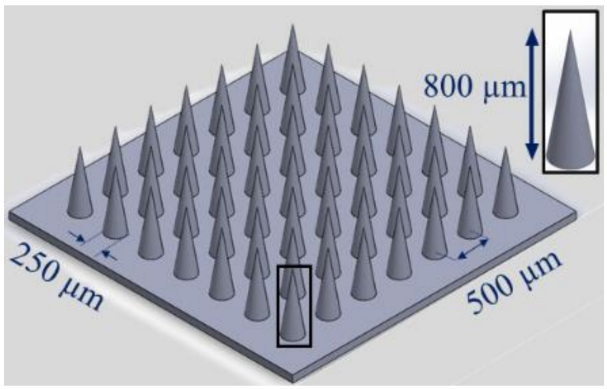

Figure 5.2: CAD model of 7×7 solid MN array using SOLIDWORKS software.

Though a layer height and hatch distance of 10 μm could be employed for the effective production of such structures with a laser power of 12 mW and a scanning speed of 0.1 mm/s, the overall fabrication time was approximately 12 hours. To overcome this barrier, a series of experiments was carried out with a scanning speed of 2 mm/s while other key process parameters directly affecting the final quality of the MNs were changed. Although the usable laser power range was shifted to higher values during these preliminary experiments due to the much shorter exposure time at 2 mm/s, onset of polymerization at low laser power and burning phenomena at high laser power were much more strongly associated with laser power, and therefore laser intensity, than total energy dose. Higher scanning velocity reduced thermal accumulation and therefore increased the burning threshold slightly compared to the value that had been observed at 0.1 mm/s. The production of bulk structures during MN fabrication allowed shorter exposure times to be employed without the risk of destroying the structures during the development phase. Complete curing was then achieved with an ultraviolet irradiation device to provide uniform cross-linking.
The resulting structures are shown in Figures 5.3-5.6, with the respective processing parameters, achieved height and fabrication times reported in Tables 5.1-5.4. The main purpose of optimizing the MN fabrication parameters was to reach the desired structure as quickly as possible without compromising accuracy.

The top row of optical microscope images in Figure 5.3 shows fabricated MNs produced with the layer height and hatch distance both equal to 10 μm, with increasing laser power from 30 mW to 50 mW from left to right. With increasing scanning speed from 0.1 mm/s to 2 mm/s, the fabrication time was reduced from 12 hours to 110 minutes, some 6.5$\times$ faster. By applying a laser power of 30 mW (a), the MNs collapsed as the laser power was insufficient to polymerize the resin with a scanning speed of 2 mm/s. Increasing the power to 40 mW (b), the MNs adhered very well to the glass substrate but the desired shape was still not obtained. Increasing the power further to 50 mW (c), the structure strength was sufficient for the MNs to be self-sustaining; however, the height of the cones increased to 1303 μm, beyond the height prescribed within the CAD model (800 μm). The bottom row of microscope images in Figure 5.3 shows MNs produced with a layer height of 10 μm and a hatch distance of 20 μm. By applying a laser power of 40 mW, structural failure occurred and no result was achieved. By increasing the power to 50 mW (d), the MNs stayed upright on the glass substrate but were not conical. With a laser power of 60 mW (e) and 70 mW (f), the desired MNs appeared. By applying laser powers of 50 mW, 60 mW and 70 mW the height of the MNs was 700 μm, 968 μm and 980 μm, respectively. The overall fabrication was further reduced to 60 minutes. Therefore, the result of increasing the hatch spacing by 10 μm was quite evident on the overall fabrication time. The applied parameters and obtained results of all MNs presented in Figure 5.3 are summarized in Table 5.1.

The top row of microscope images in Figure 5.4 shows MNs produced with a layer height of 10 μm while increasing the hatch distance to 30 μm. By applying a laser power of 50 mW (a), some individual MNs collapsed; however, by increasing laser power to 60 mW (b), the MNs attached to the glass substrate very well and the desired shape was obtained. Further increasing the laser power to 70 mW (c) resulted in an undesired MN shape due to a lack of smoothness over the entire surface. As expected, when the laser power was increased from 50 mW to 70 mW, the build height also increased from 446 μm to 910 μm. Similarly to the previous experiment, increasing the hatch distance resulted in a significant reduction in fabrication time, down to 40 minutes. The bottom row of microscope images in the same

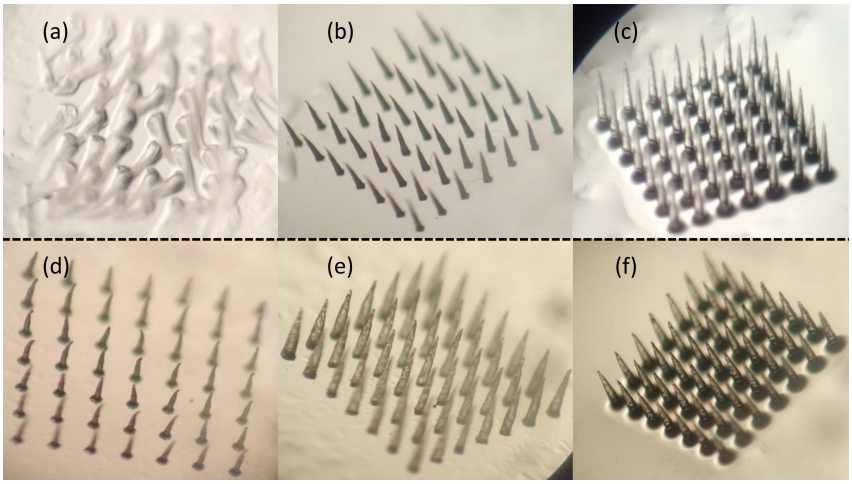

Figure 5.3: Microneedles fabricated by TPP in PETIA (b) at a constant scanning speed of 2 mm/s with: a layer height of 10 μm, hatch distance of 10 μm and laser power of 30 mW (a), 40 mW (b) and 50 mW (c); a layer height of 10 μm, hatch distance of 20 μm and laser power of 50 mW (d), 60 mW (e) and 70 mW (f).

Index	Power(mW)	Layer height(μm)	Hatch distance(μm)	Height(μm)
a	30	10	10	Collapsed
b	40	10	10	921
c	50	10	10	1303
Fabrication time: 110 minutes at 2 mm/s scanning speed				
d	50	10	20	700
e	60	10	20	968
f	70	10	20	980
Fabrication time: 60 minutes at 2 mm/s scanning speed				

Table 5.1: TPP fabrication parameters and obtained results relating to Figure 5.3.

figure shows MNs produced by increasing the layer height to 20 μm while decreasing the hatch distance to 10 μm. Owing to the relatively fast scanning velocity, 30 mW (d) of laser power was inappropriate for the whole structure to be fully polymerized.

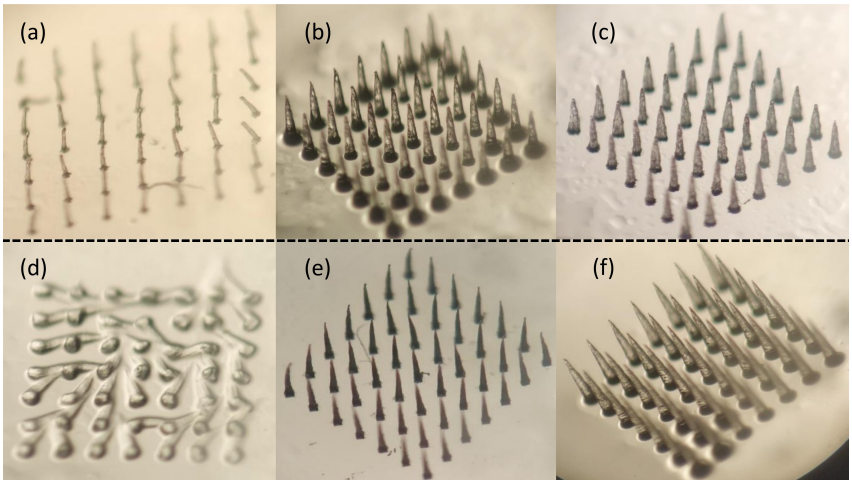

Figure 5.4: Microneedles fabricated by TPP in PETIA (b) at a constant scanning speed of 2 mm/s with: a layer height of 10 μm, hatch distance of 30 μm and laser power of 50 mW (a), 60 mW (b) and 70 mW (c); a layer height of 20 μm, hatch distance of 10 μm and laser power of 30 mW (d), 40 mW (e) and 50 mW (f).

By increasing laser power to 40 mW (e), the MNs tended to remain straighter on the glass substrate although their form was still not acceptable. A value of 50 mW (f) was essential to convert the undesirable curved shape of the MNs to the correct form; however, the structure height increased to 1188 μm, greater than the required 800 μm. The total time required to produce the structures in this case was 90 minutes. The applied parameters and obtained results of all MNs presented in Figure 5.4 are summarized in Table 5.2.

The top row of microscope images presented in Figure 5.5 shows MN patches fabricated by increasing the layer height further to 30 μm while maintaining the hatch distance constant at 10 μm. At 30 mW (a) laser power, the lack of structural integrity could be clearly seen, with some of the MNs collapsing. In order to mitigate this detrimental effect, 40 mW (b) of laser power was applied, causing the MNs to attach very well to the glass substrate, although their form was still not acceptable. By fabricating the structures with 50 mW (c), a considerable improvement in surface

Index	Power(mW)	Layer height(μm)	Hatch distance(μm)	Height(μm)
a	50	10	30	446
b	60	10	30	813
c	70	10	30	910
Fabrication time: 40 minutes at 2 mm/s scanning speed				
d	30	20	10	Collapsed
e	40	20	10	923
f	50	20	10	1188
Fabrication time: 90 minutes at 2 mm/s scanning speed				

Table 5.2: TPP fabrication parameters and obtained results relating to the Figure 5.4.

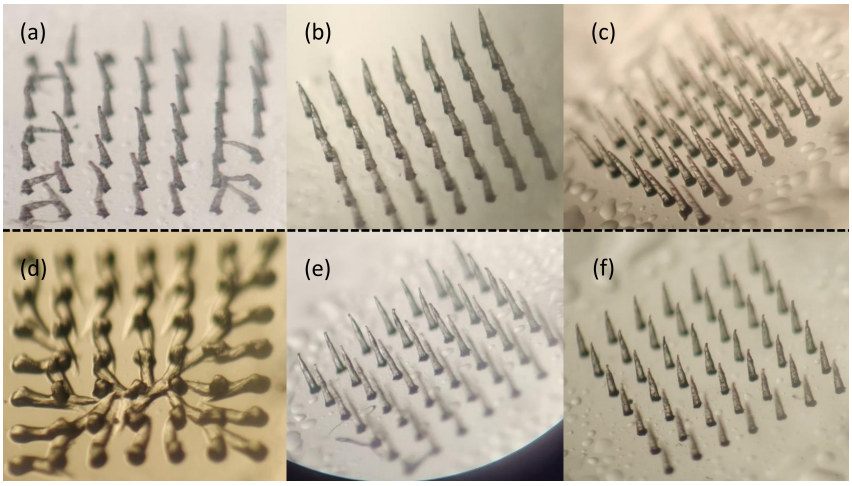

Figure 5.5: Microneedles fabricated by TPP in PETIA (b) at a constant scanning speed of 2 mm/s with: a layer height of 30 μm, hatch distance of 10 μm and laser power of 30 mW (a), 40 mW (b) and 50 (c) mW; a layer height of 20 μm, hatch distance of 20 μm and laser power of 40 mW (d), 50 mW (e) and 60 mW (f).

quality was achieved while the height of the MNs increase to 852 μm, which was relatively well aligned with the required 800 μm. In this case, 90 minutes was required to build the structures. The bottom row of microscope images shown in Figure 5.5

corresponds to MNs produced with both the layer height and hatch distance equal to 20 μm. By applying a laser power of 40 mW (d), the MNs collapsed due to incomplete polymerization, while this effect was mitigated by increasing laser power to 50 mW (e). At 60 mW (f), an appropriate structural resolution was obtained with the height of the MNs reaching 715 μm. Moreover, the total production time was reduced to 40 minutes. The applied parameters and obtained results of all MNs presented in Figure 5.5 are summarized in Table 5.3.

Index	Power(mW)	Layer height(μm)	Hatch distance(μm)	Height(μm)
a	30	30	10	Collapsed
b	40	30	10	816
c	50	30	10	852
Fabrication time: 90 minutes at 2 mm/s scanning speed				
d	40	20	20	Collapsed
e	50	20	20	700
f	60	20	20	715
Fabrication time: 40 minutes at 2 mm/s scanning speed				

Table 5.3: TPP fabrication parameters and obtained results relating to Figure 5.5.

Finally, the top row of microscope images presented in Figure 5.6 shows MNs featuring the same layer height as in the previous case (30 μm) but with a hatch distance of 30 μm. By applying a laser power of 70 mW (a), some individual MNs collapsed; however, by increasing this value to 80 mW (b) such an effect was not observed. By increasing the laser power to 100 mW (c), much higher quality was obtained after developing with an increase in the height of MNs to 981 μm. Burning did not take place despite the high value of laser power employed, as the high scanning velocity reduced thermal accumulation and therefore increased the burning threshold compared to the value that had been observed at 0.1 mm/s (70 mW). The overall fabrication time was 20 minutes, representing a significant improvement over previous cases. The bottom row of microscope images in the same figure shows MNs produced with both layer height and hatch distance equal to 40 μm. Applying 80 mW

(d) and 90 mW of laser power resulted in an undesirable MN tip shape; however, by increasing the power to 100 mW (e), the desired MNs with sharp tips were fabricated. For the two different values of laser power, 80 mW and 100 mW, the height of MNs reached 837 μm and 967 μm, respectively, within 12 minutes. The last column of the second row of Figure 5.6 presents MNs produced with both the layer height and hatch distance equal to 50 μm with a laser power of 100 mW (f). The desired MNs failed to emerge due to a defective tip shape resulting from insufficient process resolution, although the overall fabrication time was reduced to just 10 minutes. The applied parameters and obtained results of all MNs presented in Figure 5.6 are summarized in Table 5.4.

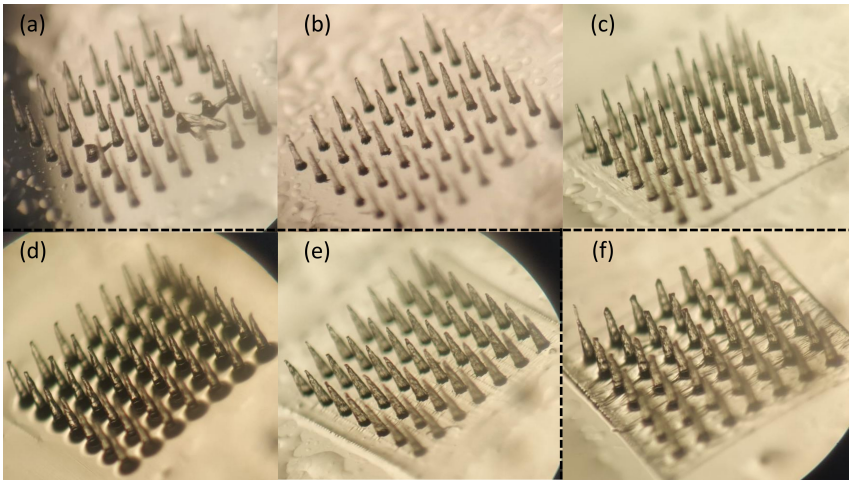

Figure 5.6: Microneedles fabricated by TPP in PETIA (b) at a constant scanning speed of 2 mm/s with: a layer height of 30 μm, hatch distance of 30 μm and laser power of 70 mW (a), 80 mW (b) and 100 mW (c); a layer height of 40 μm, hatch distance of 40 μm and laser power of 80 mW (d) and 100 mW (e); a layer height of 50 μm, hatch distance of 50 μm and laser power of 100 mW (f) mW.

The obtained results clearly demonstrate how optimization of laser power, scanning speed, layer height and hatch distance can have a profound impact on process outcomes and production times. While process resolution may improve with lower

Index	Power(mW)	Layer height(μm)	Hatch distance(μm)	Height(μm)
a	70	30	30	700
b	80	30	30	721
c	100	30	30	981
Fabrication time: 20 minutes at 2 mm/s scanning speed				
d	80	40	40	837
e	100	40	40	967
Fabrication time: 12 minutes at 2 mm/s scanning speed				
f	100	50	50	1275
Fabrication time: 10 minutes at 2 mm/s scanning speed				

Table 5.4: TPP fabrication parameters and obtained results relating to Figure 5.6.

values of laser power due to the smaller line width and voxel size, careful consideration of the required resolution, minimum feature size and total polymerized volume must be made to avoid unnecessarily high production times. Use of high laser power with a greater distance between individual lines leads not only to faster polymerization, but also creates stronger elements that are able to better withstand the development phase prior to complete curing with an ultraviolet irradiation device. In the present case, a 30 μm MN tip diameter was considered appropriate for the application at hand, allowing the fabrication time to be reduced to 20 minutes with a laser power of 80-100 mW, layer height of 30 μm and hatch distance of 30 μm at a constant scanning speed of 2 mm/s. The bulk nature of the structures allowed a relatively high scanning speed to be employed, with shorter exposure times, without the risk of destroying the structures during the development phase.

Figure 5.7 shows a SEM image of an MN array fabricated by applying a laser power of 100 mW, layer height of 30 μm, hatch distance of 30 μm and scanning speed of 2 mm/s. An accelerating voltage (HV) of 15 kV, a spot size of 4.5 and a working distance (WD) of about 12 mm were used to acquire this image. The achieved tip diameter was approximately 30 μm. Some additional particles can be observed on the MN tip surface. Further investigation into this aspect and the im-

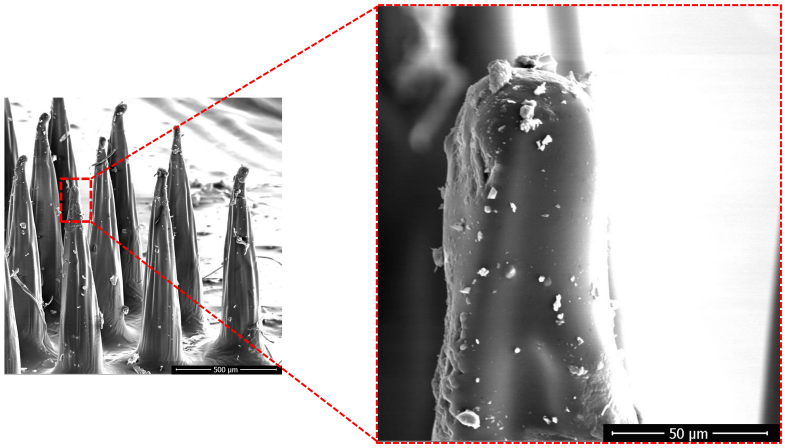

Figure 5.7: SEM image of a PETIA single MN tip created by the microfabrication via TPP.

plications of impurities generated during the process will likely be required before implementation of MNs as medical devices.

5.2 Simulation of MN-skin contact

The interaction between a single MN and human skin was studied with the finite element method (FEM) to verify the development of mechanical stress and deformation within both MN and skin during use of the device. The outcomes of this study are presented in Figure 5.8. The first step of the procedure involved developing a 3D CAD model of a single MN, comprising a cone with a height of 800 μm and base and tip diameters of 250 μm and 30 μm, respectively. The tip diameter was chosen to realistically represent the real geometry of an MN produced with the TPP fabrication method employed for experiments. A 2 mm $\times$ 2 mm $\times$ 1.6 mm block was created to represent the three main layers of human skin comprising the stratum corneum (most external), epidermis and dermis with thicknesses of 20 μm, 80 μm and 1500 μm, respectively [10]. The MN and skin geometry was imported into COMSOL Multiphysics where the two elements were assigned the respective mechanical properties

given in Table 5.5 [10]. Meshing was performed automatically within COMSOL with

	Young's modulus (GPa)	Poisson's ratio	Density(kg/m³)
Stratum corneum	1.998	0.48	1500
Epidermis	0.102	0.48	1119
Dermis	0.0102	0.48	1116
MN	3.6	0.38	1180

Table 5.5: The mechanical properties of human skin layers [10] and PETIA (b) (MN) used in numerical simulation.

free tetrahedral elements of size in the range 0.46-46 μm. The final step involved applying a coaxial force to the base of the MN with a fixed constraint at the opposite side of the skin block such that the two elements were pressed against one another. The relationship between the maximum von Mises stress in the skin and the applied

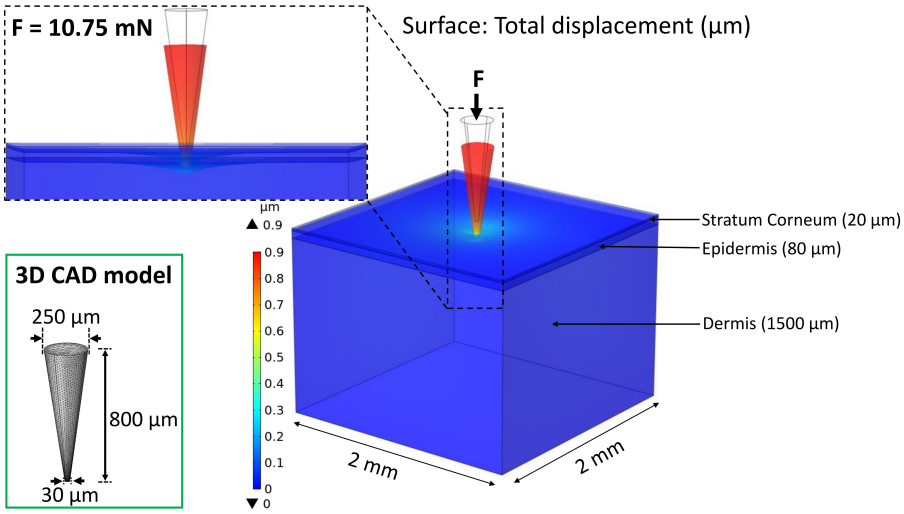

Figure 5.8: Schematic view of human skin layer displacement when 10.75 mN of force is applied uniformly in the z direction to the base of a single MN. The properties and thickness of human skin specified in Ref. [10] were used for the simulation.

force (F) is shown in Figure 5.9.

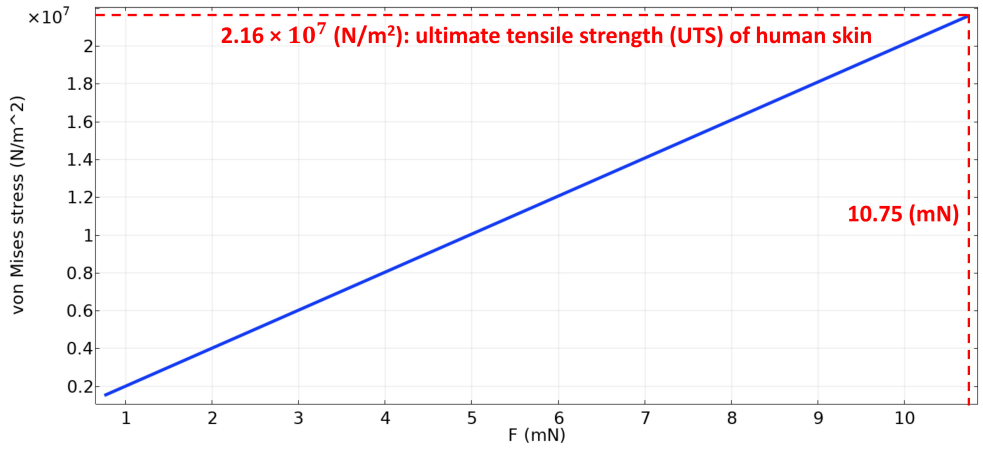

Figure 5.9: FEM simulation results: maximum von Mises stress within skin as a function of the applied force, F.

As seen from the obtained data, the equivalent stress increased linearly with the applied force up to 21.6 MPa with an applied load of 10.75 mN, representing the ultimate tensile strength of human skin [153]. The force required to overcome the stratum corneum, the strongest barrier, and subsequently reach lower skin layers was therefore approximately 10.75 mN for a single MN and 526.75 mN for 49 MNs. The von Mises stress within the MN with the same force was 51.8 MPa. It must be noted that the strength of human skin depends on a variety of factors such as location, age and gender, for which some variability must be accounted for [154]. In order to clearly demonstrate deformation of the skin, a lateral cut line was introduced in the middle of the block. As can be seen in Figure 5.10, total displacement values of 0.03 μm, 0.12 μm, 0.22 μm, 0.31 μm, 0.40 μm and 0.49 μm were obtained for values of force equal to 0.75 mN, 2.75 mN, 4.75 mN, 6.75 mN, 8.75 mN and 10.75 mN, respectively.

Figure 5.11 shows the von Mises stress distribution of the skin model with an applied force of 10.75 mN. Sharp peaks are evident in correspondence with the outer edges of the MN tip where shearing of the skin takes place. The central area di-

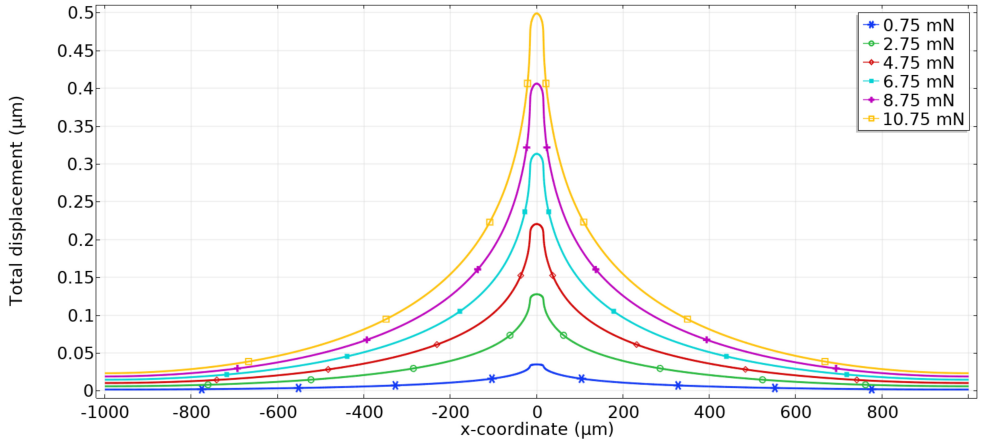

Figure 5.10: FEM simulation results: maximum total displacement of skin upon contact with MN with applied force of 0.75 mN, 2.75 mN, 4.75 mN, 6.75 mN, 8.75 mN and 10.75 mN.

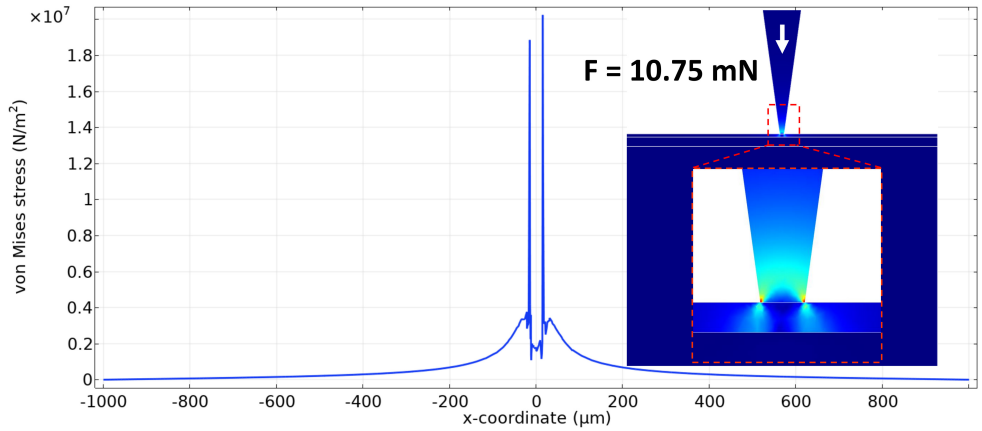

Figure 5.11: FEM simulation results: von Mises stress distribution with an applied force of 10.75 mN.

rectly below the tip instead experiences a lower level of stress. This effect clearly demonstrates the importance of TPP fabrication resolution on the resulting force requirements and stress development, as the MN tip diameter directly influences the

developed stress distribution within the skin and MN itself.

Conclusions - Part I

3D printing technology has pushed state-of-the-art manufacturing towards more advanced processing methods through its ability to produce complex computer-designed 3D structures in a wide range of materials. TPP, which belongs to one of the various innovative approaches to cutting-edge 3D printing, is applied to the fabrication ultra-precise 3D microstructures. The integration of an ultrashort pulsed laser source and an appropriate photoresist has made it an attractive candidate for advanced photonics and biomedical applications.

In the first part of this doctoral dissertation, femtosecond laser-induced TPP and its unique physical and chemical fundamentals were investigated. The steps required to build desirable 3D structures with microscale resolution through TPP were described in detail. Experiments were conducted to produce microscale square prisms with different parameters using various types of commercial (femtoBond C and E-Shell 300) and custom-made (TPGDA, PEGDA and PETIA) photoresists .

After performing a series of tests and generating a significant quantity of data in terms of processing efficiency as a function of processing parameters for the aforementioned photoresists, an acrylate-based thermosetting polymer PETIA (Pentaerythritol triacrylate monomer) with 0.2% IRGACURE 819 photoinitiator was identified as the most suitable material, allowing the fabrication of 7×7 MN arrays as a specific biomedical application of this cutting-edge technology. MNs were produced with experimental outcomes demonstrating that process parameters such as laser power, scanning speed, layer height and hatch distance are crucial factors in determining the build resolution. Insufficient laser power at high values of scanning speed caused

MNs to shrink or collapse due to incomplete photopolymerization, while excessive laser power at lower scanning speed resulted in burning of the material. By applying lower values of layer height, the height of MNs increased together with the fabrication time. The hatch distance was also found to be a fundamental parameter directly affecting MN integrity. Lower values of hatch distance increased physical strength and fabrication time, while higher values resulted in the opposite effect. Therefore, determining the optimal combination of fabrication parameters is one of the vital steps required to achieve the desired microstructure with the employed TPP setup. Finite-element simulations were then performed to analyze the stress distribution and deformation within a single MN and skin upon applying various values of force. The results indicated that the minimum force required to reach the ultimate tensile strength of human skin was 10.75 mN for a single MN and 526.75 mN for 49 MNs. The maximum equivalent stress within the PETIA (b) MN under these conditions was 51.8 MPa. Simulation results highlighted the importance of MN tip diameter and therefore TPP fabrication on the resulting force requirements and stress development.

Based on these findings, one of the primary goals for future research should be the fabrication of more advanced drug delivery devices such as hollow or dissolving MNs, as well as 4D bio-engineered scaffolds in biocompatible materials for personalized medicine and functionalized structures for sensing. Furthermore, installing a CCD camera to monitor the production process online, as well as more powerful objectives with higher NA such as 60 $\times$ or 100 $\times$ to increase the structural resolution on the existing laser system, will play a promising role in future experimentation.

Part II - Multicore fibers for high power fiber lasers

Chapter 6

Multicore fiber lasers

Multicore fibers (MCFs) are a cutting-edge technology posited as the best candidate to replace conventional fibres in lasers and optical amplifiers, due to their potential to provide further scaling of output power owing to their distinctive designs and characteristics. Depending on the desired application, multiple cores in a variety of patterns such as hexagonal, square lattice, one-ring, dual-ring, and linear array are arranged within the cladding region [155]. However, when it comes to a superior scaling of the number of cores, a square array of cores can be considered as a potential candidate since such arrangement facilitates the manufacturing process and allows for tighter packing of cores compared to the other alignments [156, 157]. As a result, these innovative optical fibers have opened up new areas of opportunities and applications in the fields of astronomy [158], telecommunication, fiber sensors, fiber lasers[159] as well as biomedical sensing and imaging applications [160].

A coherently combined laser amplifier with a quadratic arrangement of 16 Yb-doped silica cores, was experimentally fabricated as indicated in Ref. [161] where the diameter of each core, numerical aperture and center-to-center core distance (or precisely pitch), were 19 μm, 0.06 and 55 μm, respectively. Up to now, the core diameter of both commercial and custom-made active MCFs, is relatively small [162]. However, in order to avoid both complicating the MCFs design and excessively increasing the number of cores, a greater mode field area of each core seems to be an

efficient solution to achieve a considerable higher output power [163].

Rare-earth doped fiber lasers and their major drawbacks on light guidance at high-power levels such as nonlinear and thermal effects, have been discussed in this chapter. Furthermore, the impact of heat generation in the doped cores caused by the quantum defect between pump and laser signals in the optical amplification process on the performance of 9- and 16-core Yb^{3+}-doped MCFs designed for high-power lasing and amplification applications was numerically investigated through finite-element method (FEM) software package (COMSOL Multiphysics 5.4) by combining optical and thermal models.

6.1 Rare-earth doped fiber lasers

Over the last 20 years, the output average power of fiber laser and amplifier systems (both continuous wave and pulsed) has experienced an exponential growth [164]. Fiber lasers and amplifiers based on double-clad (DC) designs have moved more and more into the center of attention due to their unique characteristics of high average power along with high efficiency, compactness, and reliability [165, 166, 167]. In fact, such fibers are made up of a centered core which is doped with laser-active rare earth ions [168, 169] such as erbium (Er^{3+}), ytterbium (Yb^{3+}), neodymium (Nd^{3+}) and thulium (Tm^{3+}), etc., with a high refractive index while surrounded by an inner and outer cladding with lower refractive indexes. A review of the literature reveals that among all aforementioned ions, Er^{3+} and Yb^{3+} ions, have received greater commercial interest. While silica glass based erbium-doped fiber amplifiers (EDFA) are widely employed in the high-capacity and high-speed optical communication (C- and L-band) providing high signal gain and low noise figure over the wide bandwidth [170, 171, 172, 173], ytterbium-doped fibers are commonly utilized for high power fiber components as well as the double- clad fiber design and fabrication due to their particular characteristics, especially their high efficiency, high output power, compact structure and good beam quality [174, 175, 176].

The structural design of DC fibers allows to absorb all pump light within the laser cavity to amplify the signal light and subsequently obtain higher gain and output

power efficiency, leading to a rapid expansion in industrial, defense, scientific and medical applications [177, 178]. Besides theses potential benefits, there are some limitations including nonlinear and thermal effects which have a significant impact on the stability and further power improvement of such fibers due to the fact that some of these applications also require the light to be a single frequency and have a stable polarization state [179].

6.1.1 Nonlinear effects

At high power levels, nonlinear phenomena such as Brillouin and Raman scattering, as well as self phase modulation [177], are the primary limitations in the power scaling of fiber lasers and amplifiers [180]. In fact, the tight confinement of high-intensity light into a very tiny core diameter along a given fiber propagation length renders such fibers very sensitive to the aforementioned unfavorable consequences [181] which can negatively affect the fiber single-mode regime. Therefore, large mode area (LMA) fibers with larger core diameters and lower NA [182] can be applied as a simple solution to mitigate the mentioned detrimental effects by lowering optical intensity inside the core through distributing power across a larger effective area [183] while preserving single mode operation as far as possible. Therefore, several fiber designs including photonic crystal fibers (PCFs), chirally coupled core fibers (CCCs), photonic bandgap fibers (PBGFs), large pitch fibers (LPFs), distributed mode filtering fibers (DMFs), and leakage channel fibers (LCFs) [184, 185], have been developed. These fibers are well-known for their ability to control nonlinear effects while still maintaining outstanding beam quality at high power levels.

6.1.2 Thermal effect influence

A review of the literature reveals that thermal effects are another limiting factor for average-power scaling of pulsed fiber lasers including large-mode-area fibers (both step-index and PCFs) [185, 186] resulting in a drop in system efficiency. Transverse mode instabilities (TMIs), which emerge from the thermal dissipation process have a detrimental influence on system operation by turning a formerly stable high-quality

output beam of a high-power fiber laser into an unstable one once a certain average power threshold has been reached [187, 188]. Although an energy transfer between the fundamental mode (FM) and higher-order modes (HOMs) on a millisecond (ms) time-scale appears to be the most probable explanation of the output beam fluctuations in the fiber, a change in the relative phase between these transverse modes can be considered as a second reason as reported in Ref. [189]. As a result, selecting an adequate core diameter, chemical composition for the host glass as well as different relative refractive indices of coating materials can reduce the number of transverse modes, assuring the excellent quality of fiber lasers [190].

MCFs technology can be used to improve TMI as well as the threshold limit of non-linearities [191], by combining several lower power beams coherently to obtain a single higher power beam. In other words, power scaling is delivered by propagating independent beams which are spatially multiplexed into different adjacent cores [161].

Since each core in MCFs operates as an isolated waveguide or is designed to be single mode step-index fiber, cross-talk induced by undesired power transmission from one core to another [192] as a result of core interaction is regarded as a serious concern in this system. Optical cross-talk is fairly simple to manage by setting the cores distant enough that the overlap integral between the guided modes becomes negligible. However, high-power applications entail a strong heat load q [W/m] on the doped cores, originated by the quantum defect due to the energy difference between the pump photons and the signal ones [193], in the amplification process which is defined as [194]:

$$q = \frac{1 - 10^{-\alpha \frac{dL}{10}}}{dL}(1 - \frac{\lambda_p}{\lambda_s})P, \tag{6.1}$$

where α is the pump absorption [dB/m], dL is the fiber length [m], λ_p is the pump wavelength [nm], λ_s is the laser wavelength [nm] and P is the pump power [W]. This generates a heat flux flowing from a core through the adjacent ones, which propagates far across the fiber cross-section. In engineering applications, heat flow per unit area

ϕ $[W/m^2]$ can be described by the Newton's equation [195]:

$$\phi = h \cdot \Delta T, \tag{6.2}$$

where h is the convective heat transfer coefficient [W/(m^2·K)], and the temperature difference ΔT [K] can be characterized by:

$$\Delta T = T_{ext} - T, \tag{6.3}$$

where T_{ext} and T are the external temperature [K] and the surface temperature respectively. According to Stefan Boltzmann law, the total radiant heat power emitted from the fiber surface can be formulated as:

$$d\Phi = \sigma \cdot \varepsilon \cdot dA \cdot (T^4 - T_{ext}^4), \tag{6.4}$$

where σ [W/m$^2K^4$] is the Stefan Boltzmann constant while ε and A are the emission factor and the fiber surface area as well [196, 197]. In turn, this creates a temperature gradient inside the fiber, which induces a refractive index gradient following the temperature profile. Thus, the heat flux propagating from one core causes thermally-induced refractive index variations in other cores as described in Eq. (6.5), producing a feedback that can result in unwanted coupling between cores that would normally be optically uncoupled.

$$\Delta n = n(x,y,q) - n_c(x,y) = \beta \Delta T, \tag{6.5}$$

where β= $1.16 \cdot 10^{-5}$/K is the silica thermo-optic coefficient and $n_c(x,y)$ is the refractive index distribution for a cold-MCFs in which the value of heat lead is assumed to be zero (q=0 W/m) [198].

This gives the possibility for thermal cross-talk, leading to unwanted coupling between cores, which affects beam generation and amplification [199] by making specific modes belonging to different cores leading to degeneration and formation of supermodes [200].

6.2 Numerical model of multicore fibers

Recently, numerical simulations were performed on a system based on a 2-core MCFs, which examined the effect of the heat load on the relationship between the fundamental LP_{01} mode and the higher-order LP_{11} mode of each core. Results showed that thermal cross-talk caused feedback between the modes by affecting their field overlap with the respective doped cores. This in turn had a longitudinal effect on the refractive index profile, with almost periodic shifts that caused mode beatings and resonances [201].

In this work, the aforementioned effects of the distributed heat load on the performance of 9-core and 16-core MCFs designed for high-power fiber laser applications have been evaluated. The finite element method (FEM) was employed to model the optical field for optical amplification and lasing, by using the commercial software "COMSOL Multiphysics," which is a software package with specific numerical solvers aimed at various physics and engineering applications. In order to investigate the behavior of Yb-doped photonic-crystal fiber amplifiers, a combined thermal and optical FEM model was successfully employed to study mode power evolution and gain competition [201]. In particular, the field distributions of the guided modes are computed with the full-vector FEM modal solver, which works on a modified material permittivity tensor. The modification consists in adding a term that accounts for the thermo-optic effect, which causes a local refractive index variation Δn proportional to the temperature variation ΔT. This is calculated by the thermal FEM model, which solves the steady-state heat equation for a 2D heat propagation problem across the fiber cross-section.

6.2.1 Multicore fiber structure

As shown in Figure 6.1, MCFs with 9 (a) and 16 (b) Yb^{+3}-doped silica cores with 3×3 and 4×4 matrices, with a common cladding, featuring the same core diameter d ranging from 12 to 19 μm defined by the boundary of the doped core region, were analyzed using a thermal-optical FEM model, to obtain the thermally induced refractive index change along the fiber cross-section. The refractive index of the cores (n_c),

inner cladding (n_{icl}) and outer cladding (n_{icl}) were 1.45, 1.4487 and 1.37 respectively, while the pitch (D) varied between 25 and 55 μm. Moreover, the silica inner cladding diameter (D_i) was 420 μm and the acrylate polymer outer cladding diameter (D_o) of 600 μm was considered, having a lower glass refractive index in order to confine the pump power within the region occupied by the doped cores.

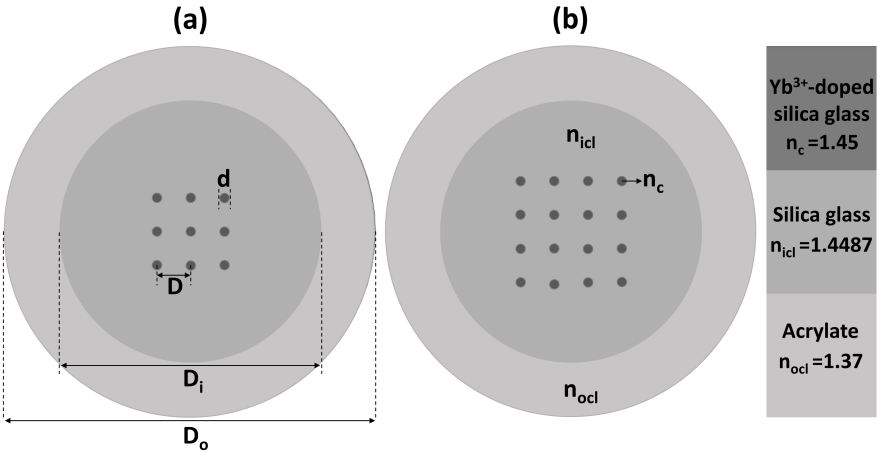

Figure 6.1: Cross-section of MCF with 9 (a) and 16 (b) step-index cores.

From the thermal point of view, the fiber was simulated for an external temperature of 25°C, a silica thermal conductivity of 1.38 W/(m·K) and a convective heat transfer coefficient of 80 W/(m^2·K) at the outer physical boundary. After designing geometry and applying physics to the model, the next step was to build the mesh with free tetrahedral elements of size in the range of 0.18-40.2 μm. It should be noted that the same mesh was used for both 9-core and 16-core MCFs simulations within this work. The optical field was modeled at 1032 nm wavelength, a typical emission wavelength of Yb^{+3} doped fiber lasers and amplifiers.

6.3 Results and discussions

In order to calculate the electric and magnetic field distributions, different values of q (according to the formula reported in Equation (6.1)) were applied to each core. As

an example, Figure 6.2 shows the electromagnetic field distribution of FMs confined in central cores in the particular case of a q equal to 5 W/m for each core.

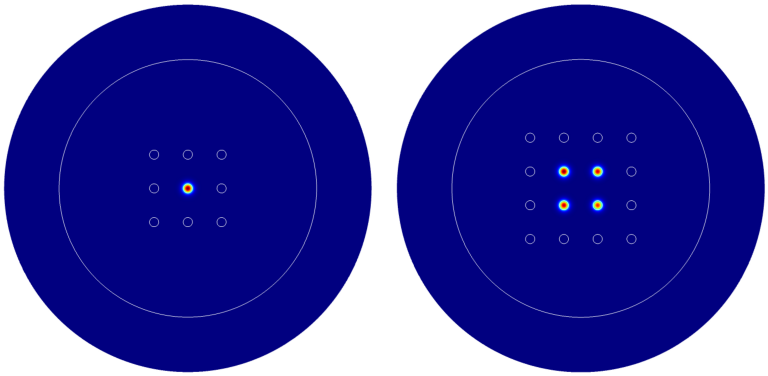

Figure 6.2: FM distribution of the 9-core (left) and 16-core (right) MCFs with q = 5 W/m equally applied to each core.

Figure 6.3 reports the temperature distribution in the entire cross-section of the mentioned fibers, as well as the temperature profile along the black dashed lines in the inset when a heat load, q = 5 W/m was applied equally to each core, resulting in a temperature profile featuring a maximum temperature of 623 K in the central core of the cross-section of 9-core or 872 K in the four central cores of 16-core MCFs, due to the combined heating effect of the neighboring cores. It should be noticed that the positions of these peaks match to the positions of the cores of these fibers cores.

As heat load q is varied between 0 and 11 W/m for 9-core as well as 0 and 7 W/m for 16-core MCFs equally for each core, three core families (A, B, C) are established. In fact, the effective mode index difference Δn_{eff} of the fundamental mode of the side cores (B) and corner cores (C) for both fibers increased linearly with the value of q, as shown in Figure 6.4, where the effective mode index of the central core (A) was taken as reference. The results show that the center core, where a significant amount of heat is concentrated, has the highest value of effective mode index with respect to the side and corner cores effective indices, which causes a change in the fiber mode guiding properties, and therefore a detrimental effect on the quality of the beam.

In fact, as it can be seen in Figure 6.5, by increasing value of the total heat load

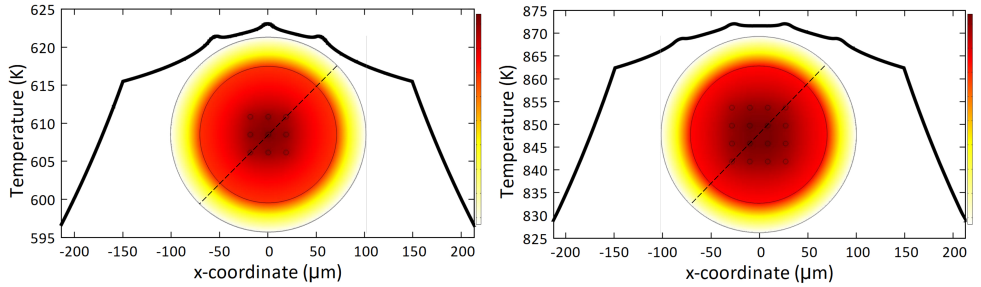

Figure 6.3: Temperature distribution on the cross-section and temperature profile along the dashed line of the inset for the 9-core (left) and 16-core (right) MCFs with q = 5 W/m for each core. The maximum value occurs for the single central core (left) or the four central cores (right).

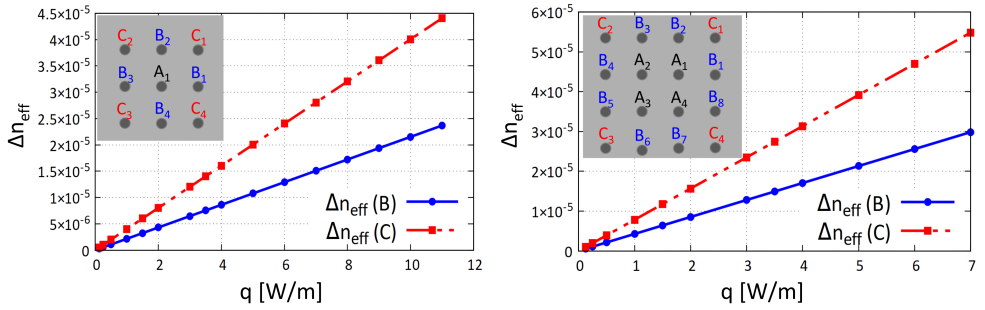

Figure 6.4: Effective index difference (Δn_{eff}) of the fundamental mode of side (B) and corner (C) cores concerning central core (A) as a function of q for the 9-core (left) and 16-core (right) MCFs with core diameter d = 12 μm.

(Σq), which is obtained by summation of the heat load across all cores, the maximum temperature (T_{max}) across the fiber, which is found in the center core, increases linearly from 306 K at 1.125 W/m to 1013.2675 K for a combined heat load of ∼100 W/m for 9-core MCFs as well as 313 K at 2 W/m to 1100.9955 K for a combined heat load of 112 W/m for 16-core MCFs. It should be noted that in order to preserve the physical integrity of the fiber, maximum temperature is limited to ∼1000 K, thus Σq to ∼100 W/m. The hard limit above which irreversible damage would occur to

the fiber is depicted with the green dashed lines in both plots.

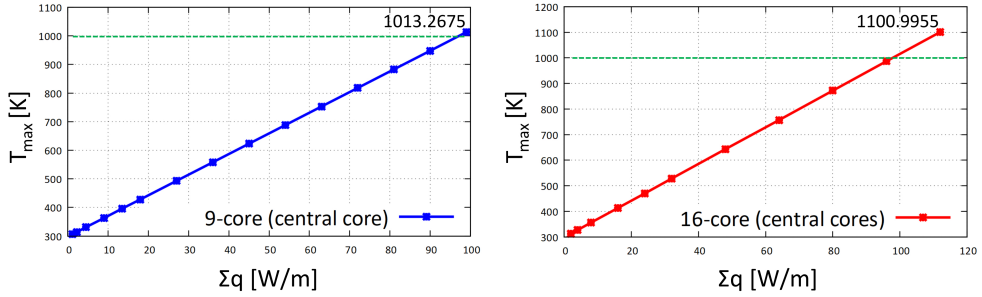

Figure 6.5: Maximum temperature (T_{max}) inside the 9-core (left) and 16-core (right) MCFs as a function of total heat load (Σq) where Σq = q $\times$ number of cores with core diameter of 12 μm. In both kinds of fiber, the T_{max} is reached in the center of the fiber (the center core in 9-core and innermost cores in 16-core MCFs).

The following results show how the heat load affects the overlap integral Γ of each mode on the active core cross-section, which gives account of the field confinement inside the cores and thus of the gain per unit of length of the mode. The FEM model calculates the guided modes, and then uses the modal field distributions to evaluate the overlap integral Γ, defined as:

$$\Gamma = \iint_{S_d} i(x,y)dxdy, \tag{6.6}$$

where S_d is the active core cross-section, and i(x,y) is the normalized intensity distribution of the mode:

$$i(x,y) = Re[P_z(x,y)/P], \tag{6.7}$$

where P is the modal power and P_z(x,y) is the distribution of the longitudinal component of the Poynting vector. In fact, the Poynting vector gives the power flow per unit area and can be obtained by multiplying the electric and magnetic fields of the modes [202, 203].

Therefore, the overlap integral of FM (Γ_{FM}) as well as the overlap integral difference ($\Delta\Gamma$) were evaluated according to Equation (6.6) by applying a uniform q to the active cores of 9-core and 16-core MCFs as shown in Figures 6.6-6.8. In fact,

$\Delta\Gamma$ gives account of the different amplification of the fundamental mode and the higher-order modes ($\Delta\Gamma_{HOM,i} = \Gamma_{FM}$ - $\Gamma_{HOM,i}$) and it is used to define the effectively single-mode behavior of the fiber [204]. It was found that the Γ_{FM} in the heat loaded case remained above 0.8, which is one criterion for effective single-mode behavior, however the overlap integral difference $\Delta\Gamma$ did not always remain above 0.3, which is the second criterion for having sufficient gain competition to prevent the higher-order mode from being amplified.

As a matter of fact, what can be clearly seen in Figure 6.6, which depicts the evolution of $\Delta\Gamma$ for d values varying from 12 to 12.5 μm, is a decreasing trend with q for the three higher-order modes closest to the fundamental mode in both 9-core and 16-core MCFs. For 9-core MCFs (left column) d = 12 μm (first row), the $\Delta\Gamma_{min}$ varies from 0.754 for q = 0.125 W/m to 0.653 for q = 11 W/m, while for d = 12.5 μm (second row), it varies from 0.708 to 0.596. However, for 16-core MCFs (right column) d = 12 μm (first row), the $\Delta\Gamma_{min}$ varies from 0.748 for q = 0.125 W/m to 0.650 for q = 7 W/m, while for d = 12.5 μm (second row), it varies from 0.713 to 0.605. Thus, for increasing diameter, the slope of $\Delta\Gamma$ variation with q tends to progressively decrease. Looking at the field profiles reveals the fact that the symmetries are respected due to the uniform distribution of the heating, however by increasing core diameter, the field is more confined into the cores and tends to distribute more to the outer cores.

As it is also confirmed in Figure 6.7 by increasing diameter, considering 9-core MCFs (left column) when d = 13 μm, $\Delta\Gamma_{min}$ varies from 0.572 for q = 0.125 W/m to 0.534 for q = 11 W/m, while for d = 13.5 μm (second row), it varies from 0.475 to 0.471. However, for 16-core MCFs (right column) d = 13 μm (first row), $\Delta\Gamma_{min}$ varies from 0.594 for q = 0.125 W/m to 0.534 for q = 7 W/m, while for d = 13.5 μm (second row), it varies from 0.467 to 0.464. In this case, the field tends to be more confined to the outer cores and $\Delta\Gamma_{min}$ is most invariant with respect to d = 12, 12.5 and 13 μm in both fibers.

This is even more apparent in Figure 6.8, where for 9-core MCFs (left column) with d = 14 μm, $\Delta\Gamma_{min}$ varies from 0.414 for q = 0.125 W/m to 0.412 for q = 11 W/m, while for 16-core MCFs (right column), it varies from 0.411 (q = 0.125 W/m) to 0.406 (q = 7 W/m). Finally, for high diameter values, the curve is almost flat and

the field is highly confined into the outer cores, however the effectively single-mode criterion is no longer valid, as for d = 19 μm (second row), $\Delta\Gamma_{min}$ varies from 0.152 (q = 0.125 W/m) to 0.149 (q = 11 W/m) for 9-core MCFs (left column). This also applies for 16-core MCFs (right column) where $\Delta\Gamma_{min}$ varies from 0.152 for q = 0.125 W/m to 0.150 for q = 7 W/m.

According to the obtained results, Γ_{FM} is slightly affected by q while up to d = 13 μm, $\Gamma_{HOM,i}$ increases in proportion to the q. Furthermore, for d > 13 μm, q has no effect on both Γ_{FM} and $\Delta\Gamma_{HOM,i}$. It should be noted that $\Delta\Gamma_{min}$ can be managed to reach single-mode operation ($\Delta\Gamma_{min} \geq 0.3$) for d $\leq$15 μm when D = 55 μm.

In the last step of the electromagnetic modeling, the performance of these fibers has been evaluated by reducing the value of pitch D from 55 to 25 μm. Figures 6.9 perfectly demonstrates that the pitch reduction decreases the value of $\Delta\Gamma_{min}$ for core diameter of 12 μm without any significant effects on the effectively single-mode condition. This is also valid for core diameters d $\leq$15 μm (except D = 25 μm for d = 15 μm where effectively single-mode behaviour fails as shown in Figure 6.10). It is worth noting that the pitch reduction for larger core diameters (d > 15 μm), has no effect on single-mode criterion where the fiber is already no longer single-mode. In fact, HOMs become more confined into the cores which causes a negative impact on the performance of both 9-core and 16-core MCFs.

The performance of such fibers can also be analyzed by taking into account the effective area and bending effects which in fact bring this model to a higher level of complexity. However, a higher degree of model complexity would lead to significant increase of computation time. Therefore, using larger amounts of physical memory (RAM), as well as an appropriate central processing unit (CPU) and graphics processing unit (GPU), is strongly suggested in order to overcome the aforementioned issue and subsequently to obtain the analytic results as quick as possible.

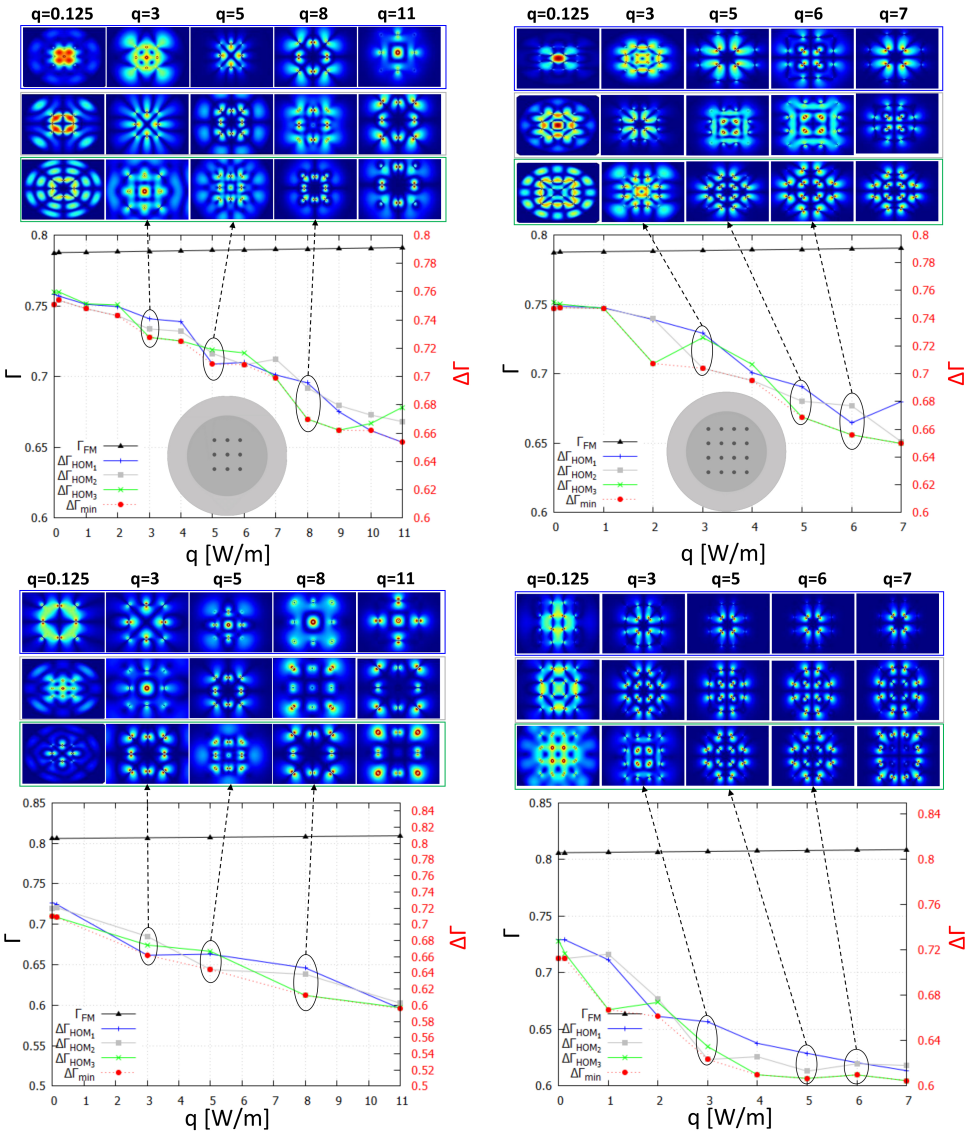

Figure 6.6: FM core overlap integral (Γ_{FM}) and overlap integral difference ($\Delta\Gamma_{HOM,i}$) between FM and three HOMs with effective index closest to FM (minimum $\Delta\Gamma_{min}$), as a function of uniform heat load q, for 9-core (left column) and 16-core (right column) MCFs with pitch D = 55 μm and core diameters d = 12 μm and d = 12.5 μm (from top to bottom).

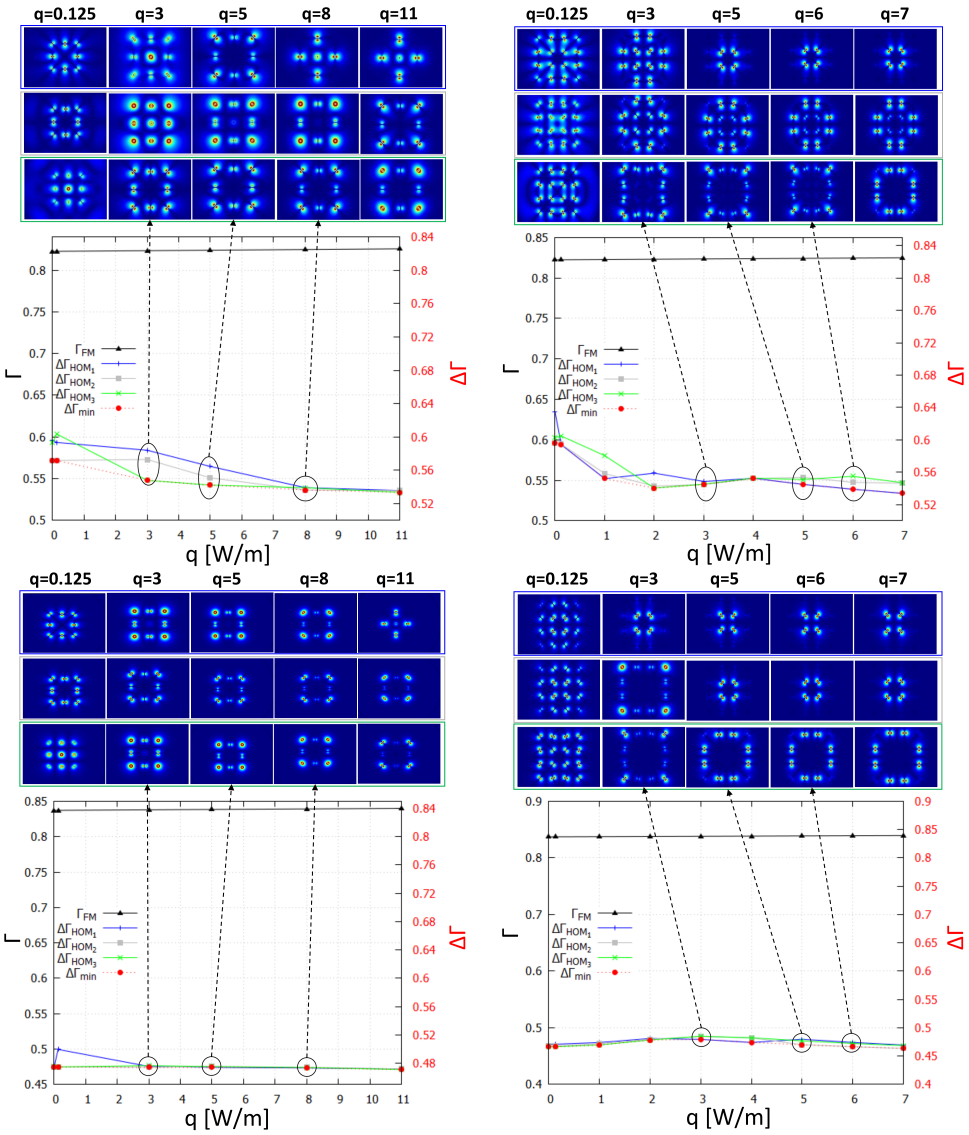

Figure 6.7: FM core overlap integral (Γ_{FM}) and overlap integral difference ($\Delta\Gamma_{HOM,i}$) between FM and three HOMs with effective index closest to FM ($\Delta\Gamma_{min}$), as a function of uniform heat load q, for 9-core (left column) and 16-core (right column) MCFs with pitch D = 55 μm and core diameters d = 13 μm and d = 13.5 μm (from top to bottom).

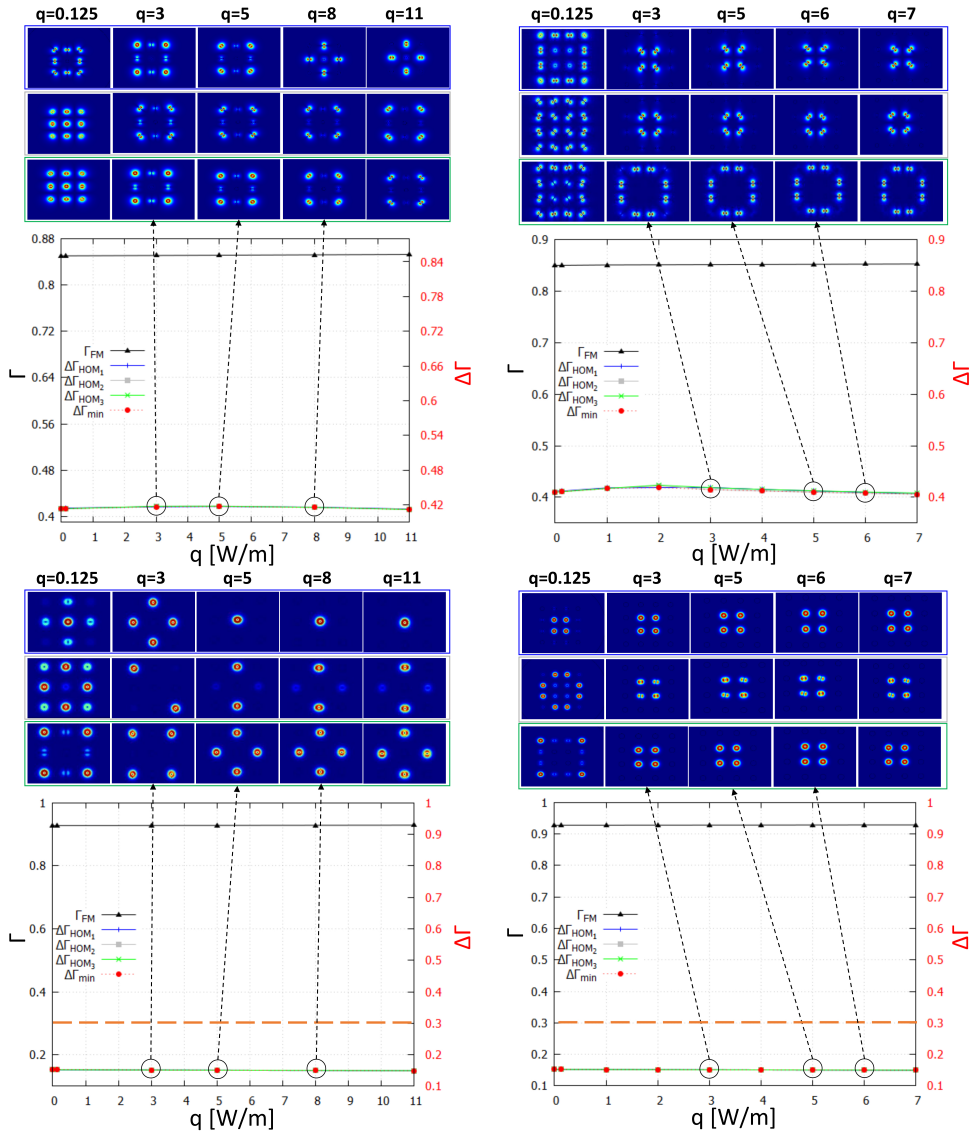

Figure 6.8: FM core overlap integral (Γ_{FM}) and overlap integral difference ($\Delta\Gamma_{HOM,i}$) between FM and three HOMs with effective index closest to FM ($\Delta\Gamma_{min}$), as a function of uniform heat load q, for 9-core (left column) and 16-core (right column) MCFs with pitch D = 55 μm and core diameters d = 14 μm and d = 19 μm (from top to bottom).

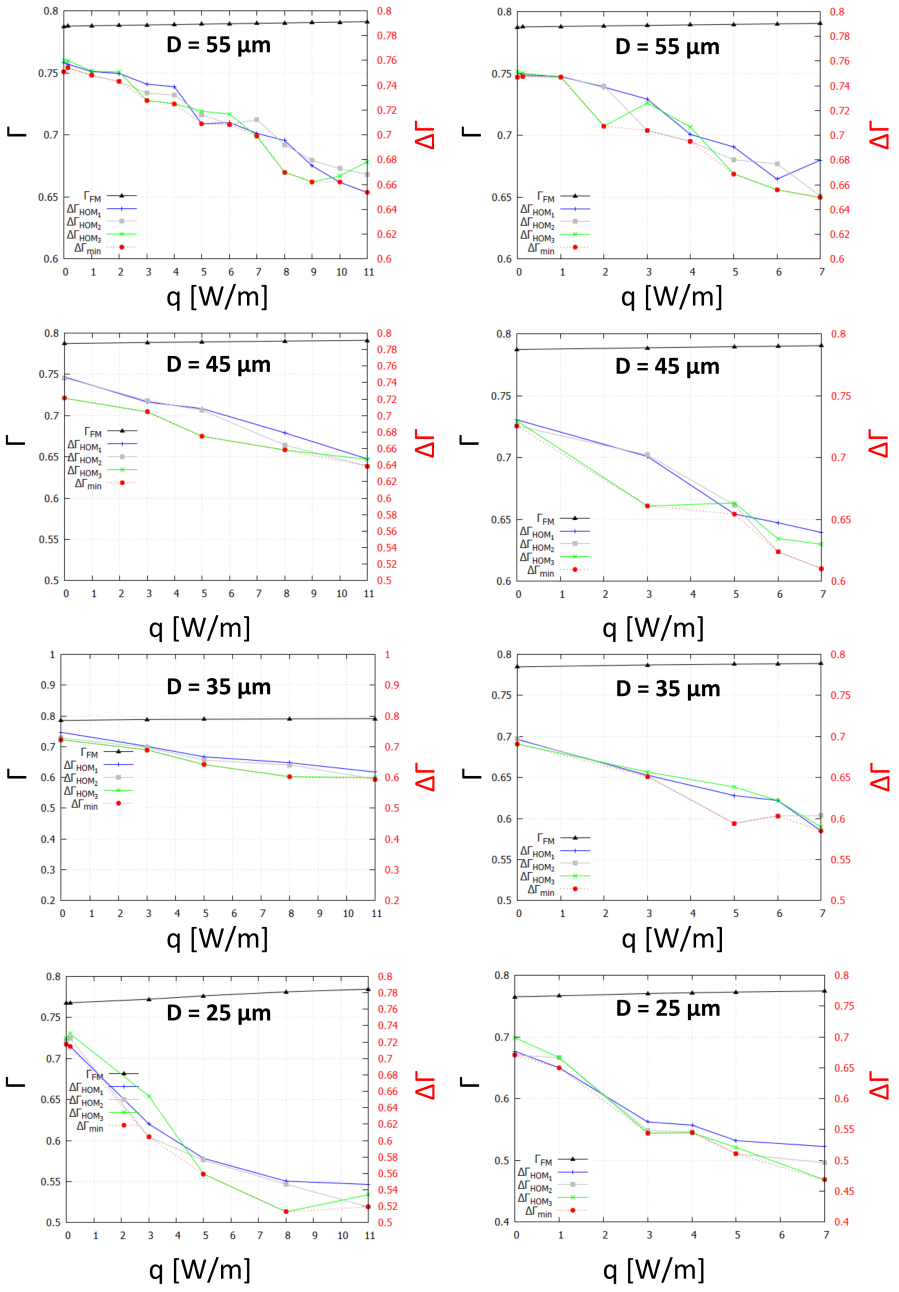

Figure 6.9: FM core overlap integral (Γ_{FM}) and overlap integral difference ($\Delta\Gamma_{HOM,i}$) between FM and three HOMs with effective index closest to FM ($\Delta\Gamma_{min}$), as a function of uniform heat load q, for 9-core (left column) and 16-core (right column) MCFs with core diameter d = 12 μm and pitch D reduction from 55 to 25 μm (from top to bottom).

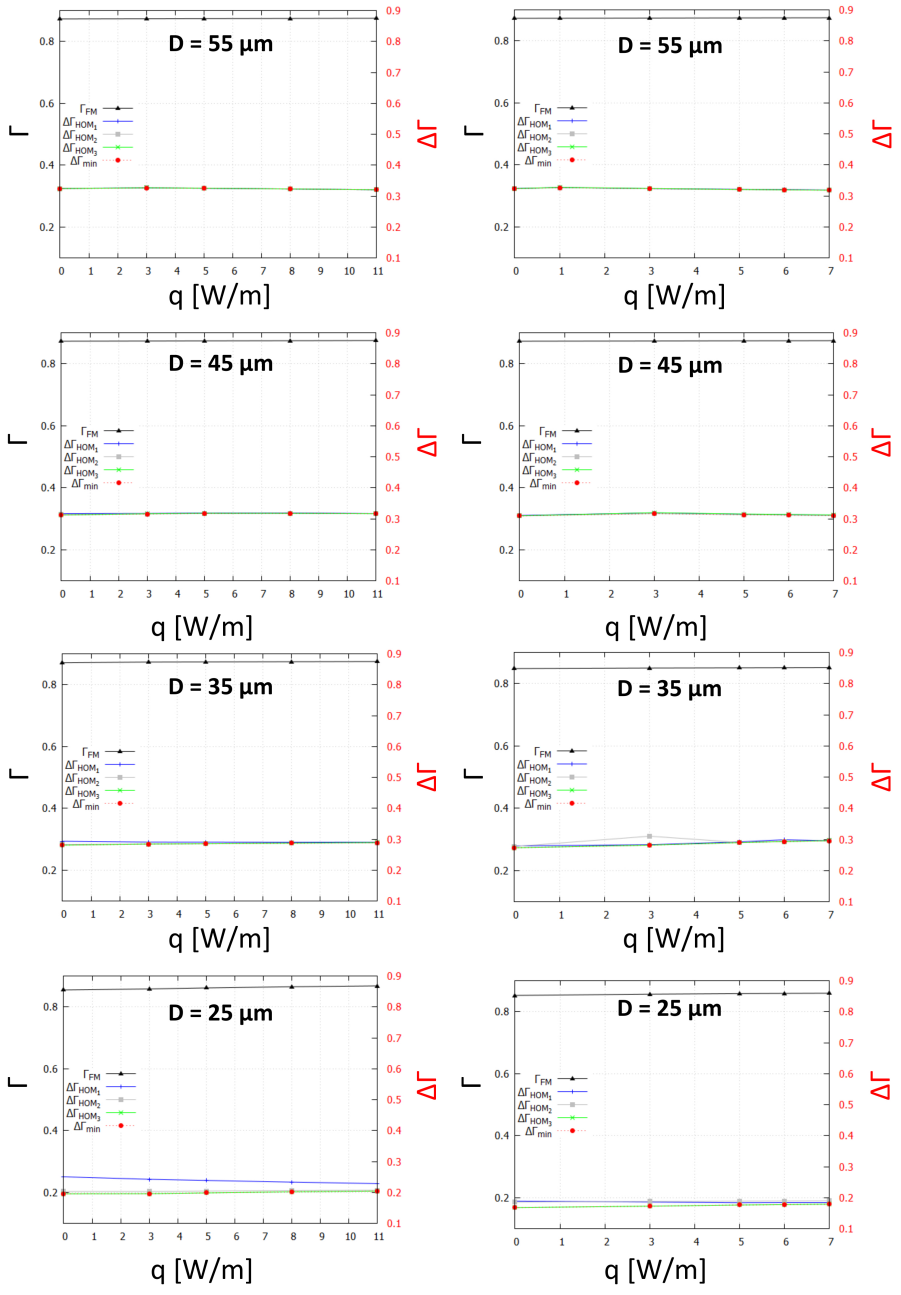

Figure 6.10: FM core overlap integral (Γ_{FM}) and overlap integral difference ($\Delta\Gamma_{HOM,i}$) between FM and three HOMs with effective index closest to FM ($\Delta\Gamma_{min}$), as a function of uniform heat load q, for 9-core (left column) and 16-core (right column) MCFs with core diameter d = 15 μm and pitch D reduction from 55 to 25 μm (from top to bottom).

Conclusions - part II

High average power lasers, widely employed for materials processing and defense applications, are also effective in a variety of scientific applications such as laser-based guidance systems for astronomy, gravitational wave detection, coherent remote wind sensing, and laser-based particle acceleration. Fiber-based lasers and amplifiers have demonstrated their ability to produce high average power while remaining efficient, compact, and reliable. Thermal effects are currently regarded as the most significant barrier to power scaling of fiber lasers in high power applications. Transverse mode instabilities (TMIs), identified as the most damaging feature of thermal effects, turn the formerly stable high quality output beam of a high power fiber laser into an unstable beam once a certain average power threshold has been reached.

Therefore, the second part of this thesis focused on multicore fibers (MCFs), which are regarded as a good candidate to overcome the threshold power limit caused by the onset of nonlinearities and TMIs in high-power applications due to their potential to deliver a single higher-power beam by coherently combining several lower power beams. 9-core and 16-core MCFs for high-power fiber lasers were also studied numerically, highlighting impairment due to thermal effects under severe heat load during amplification. The finite-element method (FEM) was employed to model the optical field distribution for optical amplification and lasing to analyze the effects of heat load on the modes of ytterbium-doped MCFs. According to the obtained results, fiber guidance properties are strongly affected by mode coupling effects induced by thermally-induced refractive index distortion. Therefore, a maximum combined heat load of 100 W/m was determined as an acceptable limit for avoiding irreversible

fiber damage. A decreasing trend of $\Delta\Gamma$ vs. q was observed for the three higher-order modes (HOMs) closest to the fundamental mode. Moreover, for higher values of core diameter, d, the slope of $\Delta\Gamma$ tended to flatten. As a result, the minimum value of $\Delta\Gamma$ consistently decreased with increasing d, to the point where the single-mode criterion could no longer be maintained. In fact, for d > 15 μm, it was found that HOMs became more confined to the cores, causing a negative impact on the optical beam quality. To summarize, the core diameter appears to be a critical parameter in ensuring single mode or effective single mode propagation within each core of the fiber.

To facilitate the adoption of MCFs for high-power beam delivery in the future, comprehensive research must now be performed into effective area and bending effects as these fundamental parameters will play a major role in achieving pragmatic results in this specific field.

List of publications

The result of the activities during the PhD are reflected in the following articles.

- L. Rosa, S. Mckee, F. Poli, A. Cucinotta, L. Vincetti, "Thermo-optical numerical modal analysis of multicore fibers for high power lasers and amplifiers," Optical Fiber Technology, 2022;70:102857.
- S. Mckee, A. Lutey, C. Sciancalepore, F. Poli, S. Selleri, A. Cucinotta, "Microfabrication of polymer microneedle arrays using two-photon polymerization," Journal of Photochemistry and photobiology. B, Biology, 2022;229:112424.
- Fornaini C, Poli F, Merigo E, Lutey A, Cucinotta A, Chevalier M, Mckee S et al. “Nanosecond pulsed fiber laser irradiation for enhanced zirconia crown adhesion: Morphological, chemical, thermal and mechanical analysis,” Journal of Photochemistry and photobiology. B, Biology, 2021 Jun;219:112189.
- S. Mckee et al., "3D Printing by Two-Photon Polymerization," 2020 Italian Conference on Optics and Photonics (ICOP), 2020, pp. 1-3.
- S. Mckee, L. Rosa, F. Poli, L. Vincetti, A. Cucinotta, S. Selleri, " “THERMAL EFFECTS ON OPTICAL AMPLIFICATION IN 16-CORE MCFS,"Italian Conference on Optics and Photonics 2020 - ICOP 2020, September 8-11, 2020, Parma, Italy.
- C. Fornaini, F. Poli, E. Merigo, A. Lutey, A. Cucinotta, M. Chevalier, N. Brulat, S. Mckee, G. Trevisi, “1070 NM FIBER LASER SHORT PULSES LASER

IRRADIATION ON ZIRCONIA SURFACE: MORPHOLOGICAL, CHEMICAL, THERMAL AND MECHANICAL ANALYSIS ," Italian Conference on Optics and Photonics 2020 - ICOP 2020, September 8-11, 2020, Parma, Italy.

- L. Rosa, S. Mckee, L. Vincetti, F. Poli, S. Selleri, A. Cucinotta, "Thermo-optic effects in multicore fibers for high power lasers " SPIE Photonics Europe, March 29 - April 2, 2020, Strasbourg, France (Invited).

- S. Mckee, F. Poli, S. Selleri, A. Cucinotta, L. Rosa, L. Vincetti, "Guidance properties and thermal effects in 9-core Yb-doped fiber for high power applications," 5th International Forum on Research and Technologies for Society and Industry - IEEE RTSI 2019, September 9-12, 2019, Florence, Italy.

- L. Rosa, S. Mckee, C. Molardi, F. Poli, S. Selleri, L. Vincetti, A. Cucinotta, "Phasing and Guidance Properties of Multi-Core Fibers under Heat Load " CLEO/Europe-EQEC 2019, June 23-27, 2019, Munich, Germany, CJ-P.77.

- S. Mckee, L. Rosa, F. Poli, S. Selleri, L. Vincetti, A. Cucinotta, "Electromagnetic Analysis of a 9-core Yb-doped Fiber for High Power Applications," Progress in Electromagnetics Research Symposium - PIERS 2019, June 17-20, 2019, Rome, Italy.

Bibliography

[1] L. Jiao, Z. Chua, S. K. Moon, Jie Song, G. Bi, and Hongyu Y Zheng. Femtosecond laser produced hydrophobic hierarchical structures on additive manufacturing parts. *Nanomaterials*, 8, 2018.

[2] Yong He, Yan Wu, Jian-zhong Fu, Qing Gao, and Jing-jiang Qiu. Developments of 3d printing microfluidics and applications in chemistry and biology: a review. *Electroanalysis*, 28(8):1658–1678, 2016.

[3] Daniel S Correa, Leonardo De Boni, Adriano JG Otuka, Vinicius Tribuzi, and Cleber R Mendonça. *Two-photon polymerization fabrication of doped microstructures*, volume 30. InTech, 2012.

[4] Kwang-Sup Lee, Ran Hee Kim, Dong-Yol Yang, and Sang Hu Park. Advances in 3d nano/microfabrication using two-photon initiated polymerization. *Progress in Polymer Science*, 33(6):631–681, 2008.

[5] Shuhui Wu, Jesper Serbin, and Min Gu. Two-photon polymerisation for three-dimensional micro-fabrication. *Journal of Photochemistry and Photobiology A: Chemistry*, 181(1):1–11, 2006.

[6] Joel M. Hales, San-Hui Chi, Vincent W. Chen, and Joseph W. Perry. *TWO-PHOTON ABSORPTION: CONCEPTS, MOLECULAR MATERIALS AND APPLICATIONS*, chapter 13, pages 397–442. World Scientific, 2016.

[7] Andreas Ostendorf and Boris Chichkov. Two-photon polymerization: A new approach to micromachining. *Photonics Spectra*, 40:72–80, 10 2006.

[8] Erika Zanchetta, Gioia Della Giustina, Gianluca Grenci, Alessandro Pozzato, Massimo Tormen, and Giovanna Brusatin. Novel hybrid organic–inorganic spin-on resist for electron- or photon-based nanolithography with outstanding resistance to dry etching. *Advanced Materials*, 25(43):6261–6265, 2013.

[9] Alexey S Rzhevskiy, Thakur R R Singh, Ryan F. Donnelly, and Yuri German Anissimov. Microneedles as the technique of drug delivery enhancement in diverse organs and tissues. *Journal of controlled release : official journal of the Controlled Release Society*, 270:184–202, 2018.

[10] A. McBride, S. Bargmann, D. Pond, and G. Limbert. Thermoelastic modelling of the skin at finite deformations. *Journal of Thermal Biology*, 62:201–209, 2016. Modeling bioheat transfer processes and thermoregulatory responses.

[11] Mario D'auria, William Otter, Jonathan Hazell, Brendan Gillatt, Callum Long-Collins, N.M. Ridler, and Stepan Lucyszyn. 3-d printed metal-pipe rectangular waveguides. *IEEE Transactions on Components, Packaging, and Manufacturing Technology*, 5:1339–1349, 09 2015.

[12] Simon Ford and Mélanie Despeisse. Additive manufacturing and sustainability: an exploratory study of the advantages and challenges. *Journal of Cleaner Production*, 137:1573–1587, 2016.

[13] Mojtaba Khorram Niaki, S. Ali Torabi, and Fabio Nonino. Why manufacturers adopt additive manufacturing technologies: The role of sustainability. *Journal of Cleaner Production*, 222:381–392, 2019.

[14] Yubo Tao, Qing Yin, and Peng Li. An additive manufacturing method using large-scale wood inspired by laminated object manufacturing and plywood technology. *Polymers*, 13(1), 2021.

[15] Mohsen Attaran. Additive manufacturing: The most promising technology to alter the supply chain and logistics. *Journal of Service Science and Management*, 10, 06 2017.

[16] Abid Haleem, Mohd Javaid, Rizwan Hasan Khan, and Rajiv Suman. 3d printing applications in bone tissue engineering. *Journal of Clinical Orthopaedics and Trauma*, 11:S118–S124, 2020.

[17] Zhenbin Liu, Min Zhang, Bhesh Bhandari, and Yuchuan Wang. 3d printing: Printing precision and application in food sector. *Trends in Food Science & Technology*, 69:83–94, 2017.

[18] Guo Dong Goh, Swee Leong Sing, and Wai Yee Yeong. A review on machine learning in 3d printing: applications, potential, and challenges. *Artificial Intelligence Review*, 54, 01 2021.

[19] Jasveer Shiwpursad and Jianbin Xue. Comparison of different types of 3d printing technologies. *International Journal of Scientific and Research Publications (IJSRP)*, 8, 04 2018.

[20] Qiang Geng, Dien Wang, Pengfei Chen, and Shih-Chi Chen. Ultrafast multi-focus 3-d nano-fabrication based on two-photon polymerization. *Nature Communications*, 10, 05 2019.

[21] Swee Leong Sing, Jia An, Wai Yee Yeong, and Florencia Edith Wiria. Laser and electron-beam powder-bed additive manufacturing of metallic implants: A review on processes, materials and designs. *Journal of Orthopaedic Research*, 34(3):369–385, 2016.

[22] Paolo C. Priarone, Vincenzo Lunetto, Eleonora Atzeni, and Alessandro Salmi. Laser powder bed fusion (l-pbf) additive manufacturing: On the correlation between design choices and process sustainability. *Procedia CIRP*, 78:85–90, 2018. 6th CIRP Global Web Conference – Envisaging the future manufacturing, design, technologies and systems in innovation era (CIRPe 2018).

[23] Xu Song, Wei Zhai, Rui Huang, Jin Fu, Ming Wang Fu, and Feng Li. Metal-based 3d-printed micro parts & structures. In Francisca G. Caballero, editor, *Encyclopedia of Materials: Metals and Allloys*, pages 448–461. Elsevier, Oxford, 2022.

[24] Eleftherios Louvis, Peter Fox, and Christopher J. Sutcliffe. Selective laser melting of aluminium components. *Journal of Materials Processing Technology*, 211(2):275–284, 2011.

[25] C. Y. Yap, C. K. Chua, Z. L. Dong, Z. H. Liu, D. Q. Zhang, L. E. Loh, and S. L. Sing. Review of selective laser melting: Materials and applications. *Applied Physics Reviews*, 2(4):041101, 2015.

[26] Konda Gokuldoss Prashanth. Selective laser melting: Materials and applications. *Journal of Manufacturing and Materials Processing*, 4(1), 2020.

[27] Sorin Cosma. Manufacturing of implants by selective laser melting. *Balneo Research Journal*, 3:85–90, 09 2012.

[28] Jianyu Chen, Zhiguang Zhang, Xianshuai Chen, Chunyu Zhang, Gong Zhang, and Zhewu Xu. Design and manufacture of customized dental implants by using reverse engineering and selective laser melting technology. *The Journal of Prosthetic Dentistry*, 112(5):1088–1095.e1, 2014.

[29] Bartłomiej Wysocki, Piotr Maj, Ryszard Sitek, Joseph Buhagiar, Krzysztof Jan Kurzydłowski, and Wojciech Święszkowski. Laser and electron beam additive manufacturing methods of fabricating titanium bone implants. *Applied Sciences*, 7(7), 2017.

[30] T.B. Sercombe, L.-C. Zhang, S. Li, and Y. Hao. 3.6 - additive manufacturing of cp-ti, ti-6al-4v and ti2448. In Francis H. Froes and Ma Qian, editors, *Titanium in Medical and Dental Applications*, Woodhead Publishing Series in Biomaterials, pages 303–324. Woodhead Publishing, 2018.

[31] James Mutua, Shinya Nakata, Tetsuhiko Onda, and Zhong-Chun Chen. Optimization of selective laser melting parameters and influence of post heat treatment on microstructure and mechanical properties of maraging steel. *Materials & Design*, 139:486–497, 2018.

[32] Khurram Munir, Arne Biesiekierski, Cuie Wen, and Yuncang Li. 7 - selective laser melting in biomedical manufacturing. In Cuie Wen, editor, *Metallic Biomaterials Processing and Medical Device Manufacturing*, Woodhead Publishing Series in Biomaterials, pages 235–269. Woodhead Publishing, 2020.

[33] Richard Bibb. 5 - physical reproduction – rapid prototyping technologies. In Richard Bibb, editor, *Medical Modelling*, Woodhead Publishing Series in Biomaterials, pages 59–96. Woodhead Publishing, 2006.

[34] Paulo Bartolo, Jean-Pierre Kruth, Jorge Silva, Gideon Levy, Ajay Malshe, Kamlakar Rajurkar, Mamoru Mitsuishi, Joaquim Ciurana, and Ming Leu. Biomedical production of implants by additive electro-chemical and physical processes. *CIRP Annals - Manufacturing Technology*, 61:635–655, 12 2012.

[35] Mitchell George, Kevin Aroom, Harvey Hawes, Brijesh Gill, and Joseph Love. 3d printed surgical instruments: The design and fabrication process. *World journal of surgery*, 41, 11 2016.

[36] Fabrizio Fina, Alvaro Goyanes, Simon Gaisford, and Abdul W. Basit. Selective laser sintering (sls) 3d printing of medicines. *International Journal of Pharmaceutics*, 529(1):285–293, 2017.

[37] Ian S. Kinstlinger, Andreas Bastian, Samantha J. Paulsen, Daniel H. Hwang, Anderson H. Ta, David R. Yalacki, Tim Schmidt, and Jordan S. Miller. Open-source selective laser sintering (opensls) of nylon and biocompatible polycaprolactone. *PLOS ONE*, 11(2):1–25, 02 2016.

[38] Nour Allahham, Fabrizio Fina, Carmen Marcuta, Lilia Kraschew, Wolfgang Franz Dietrich Mohr, Simon Gaisford, Abdul W. Basit, and Alvaro Goyanes. Selective laser sintering 3d printing of orally disintegrating printlets containing ondansetron. *Pharmaceutics*, 12:110, 01 2020.

[39] Atheer Awad, Fabrizio Fina, Alvaro Goyanes, Simon Gaisford, and Abdul W. Basit. 3d printing: Principles and pharmaceutical applications of selective laser sintering. *International Journal of Pharmaceutics*, 586:119594, 2020.

[40] K.S. Munir, Y. Li, and C. Wen. 1 - metallic scaffolds manufactured by selective laser melting for biomedical applications. In Cuie Wen, editor, *Metallic Foam Bone*, pages 1–23. Woodhead Publishing, 2017.

[41] David Kazmer. 28 - three-dimensional printing of plastics. In Myer Kutz, editor, *Applied Plastics Engineering Handbook (Second Edition)*, Plastics Design Library, pages 617–634. William Andrew Publishing, second edition edition, 2017.

[42] Christina Schmidleithner and Deepak Kalaskar. *3D Printing*, chapter Stereolithography, pages 3–22. InTech, 10 2018.

[43] Jill Z. Manapat, Qiyi Chen, Piaoran Ye, and Rigoberto C. Advincula. 3d printing of polymer nanocomposites via stereolithography. *Macromolecular Materials and Engineering*, 302(9):1600553, 2017.

[44] Guojiao Ding, Zhang Keqiang, Niping Zhou, and Hao Xu. Stereolithography 3d printing of sic ceramic with potential for lightweight optical mirror. *Ceramics International*, 46, 04 2020.

[45] Serge Corbel, Olivier Dufaud, and Thibault Roques-Carmes. *Materials for Stereolithography*, pages 141–159. Springer US, 01 2011.

[46] Jian-Yuan Lee, Jia An, and Chee Kai Chua. Fundamentals and applications of 3d printing for novel materials. *Applied Materials Today*, 7:120–133, 2017.

[47] Ferry P.W. Melchels, Jan Feijen, and Dirk W. Grijpma. A review on stereolithography and its applications in biomedical engineering. *Biomaterials*, 31(24):6121–6130, 2010.

[48] Haoyuan Quan, Ting Zhang, Hang Xu, Shen Luo, Jun Nie, and Xiaoqun Zhu. Photo-curing 3d printing technique and its challenges. *Bioactive Materials*, 5(1):110–115, 2020.

[49] Ferry P W Melchels, Jan Feijen, and Dirk W. Grijpma. A review on stereolithography and its applications in biomedical engineering. *Biomaterials*, 31(24):6121–6130, August 2010.

[50] Muslim Mukhtarkhanov, Asma Perveen, and Didier Talamona. Application of stereolithography based 3d printing technology in investment casting. *Micromachines*, 11:946, 10 2020.

[51] Pedram Parandoush and Dong Lin. A review on additive manufacturing of polymer-fiber composites. *Composite Structures*, 182:36–53, 2017.

[52] Micheal McLamb, Yanzeng Li, Paige Stinson, and Tino Hofmann. Metasurfaces for the infrared spectral range fabricated using two-photon polymerization. *Thin Solid Films*, 721:138548, 2021.

[53] Yang Lin and Jie Xu. Microstructures fabricated by two-photon polymerization and their remote manipulation techniques: Toward 3d printing of micromachines. *Advanced Optical Materials*, 6(8):1701359, 2018.

[54] Satoshi Kawata, Hong-Bo Sun, Tomokazu Tanaka, and Kenji Takada. Finer features for functional microdevices. *Nature*, 412:697–8, 09 2001.

[55] Linjie Li, Rafael R. Gattass, Erez Gershgoren, Hana Hwang, and John T. Fourkas. Achieving $\lambda/20$ resolution by one-color initiation and deactivation of polymerization. *Science*, 324(5929):910–913, 2009.

[56] S.-H. Park, D.-Y. Yang, and K.-S. Lee. Two-photon stereolithography for realizing ultraprecise three-dimensional nano/microdevices. *Laser & Photonics Reviews*, 3(1-2):1–11, 2009.

[57] Rafael Gattass and Eric Mazur. Femtosecond laser micromachining in transparent materials. *Nature Photonics*, 2:219–225, 04 2008.

[58] Takuo Tanaka, Atsushi Ishikawa, and Satoshi Kawata. Two-photon-induced reduction of metal ions for fabricating three-dimensional electrically conductive metallic microstructure. *Applied Physics Letters*, 88(8):081107, 2006.

[59] Tiziana Ritacco, Giuseppe Emanuele Lio, Xiaolun Xu, Aurélie Broussier, Ali Issa, Michele Giocondo, Renaud Bachelot, Sylvain Blaize, Christophe Couteau, and Safi Jradi. Three-dimensional photoluminescent crypto-images doped with (cdse)zns quantum dots by one-photon and two-photon polymerization. *ACS Applied Nano Materials*, 4(7):6916–6927, 2021.

[60] John T. Fourkas and John S. Petersen. 2-colour photolithography. *Phys. Chem. Chem. Phys.*, 16:8731–8750, 2014.

[61] Ryan C. Sullivan, Kyle Gorkowski, and Leif Jahn. Chapter 12 - characterization of individual aerosol particles. In Jennifer A. Faust and James E. House, editors, *Physical Chemistry of Gas-Liquid Interfaces*, Developments in Physical & Theoretical Chemistry, pages 353–402. Elsevier, 2018.

[62] Xiaoqin Zhou, Yihong Hou, and Jieqiong Lin. A review on the processing accuracy of two-photon polymerization. *AIP Advances*, 5(3):030701, 2015.

[63] J. Serbin, A. Egbert, A. Ostendorf, B. N. Chichkov, R. Houbertz, G. Domann, J. Schulz, C. Cronauer, L. Fröhlich, and M. Popall. Femtosecond laser-induced two-photon polymerization of inorganic–organic hybrid materials for applications in photonics. *Opt. Lett.*, 28(5):301–303, Mar 2003.

[64] Razvan Stoian. Volume photoinscription of glasses: three-dimensional micro- and nanostructuring with ultrashort laser pulses. *Applied Physics A*, 126:1–30, 2020.

[65] Zhaoxin Lao, Neng Xia, Shijie Wang, Tiantian Xu, Xinyu Wu, and Li Zhang. Tethered and untethered 3d microactuators fabricated by two-photon polymerization: A review. *Micromachines*, 12(4), 2021.

[66] Karsten König, Iris Riemann, Frank Stracke, and Ronan Le Harzic. Nanoprocessing with nanojoule near-infrared femtosecond laser pulses. *Medical Laser Application*, 20(3):169–184, 2005.

[67] Muhammad Arif Mahmood and Andrei C. Popescu. 3d printing at micro-level: Laser-induced forward transfer and two-photon polymerization. *Polymers*, 13(13), 2021.

[68] A. Ovsianikov, B. Chichkov, P. Mente, N. A. Monteiro-Riviere, A. Doraiswamy, and R. J. Narayan. Two photon polymerization of polymer–ceramic hybrid materials for transdermal drug delivery. *International Journal of Applied Ceramic Technology*, 4(1):22–29, 2007.

[69] Shoji Maruo, Osamu Nakamura, and Satoshi Kawata. Three-dimensional microfabrication with two-photon-absorbed photopolymerization. *Opt. Lett.*, 22(2):132–134, Jan 1997.

[70] Martin Straub and Min Gu. Near-infrared photonic crystals with higher-order bandgaps generated by two-photon photopolymerization. *Opt. Lett.*, 27(20):1824–1826, Oct 2002.

[71] Mikhail V. Rybin, Ivan I. Shishkin, Kirill B. Samusev, Pavel A. Belov, Yuri S. Kivshar, Roman V. Kiyan, Boris N. Chichkov, and Mikhail F. Limonov. Band structure of photonic crystals fabricated by two-photon polymerization. *Crystals*, 5(1):61–73, 2015.

[72] M. Rill, C. Plet, M. Thiel, M. Wegener, G. von Freymann, and S. Linden. Photonic metamaterials by direct laser writing and silver chemical vapor deposition. In *Conference on Lasers and Electro-Optics/Quantum Electronics and Laser Science Conference and Photonic Applications Systems Technologies*, page QMD3. Optical Society of America, 2008.

[73] Tobias Frenzel, Muamer Kadic, and Martin Wegener. Three-dimensional mechanical metamaterials with a twist. *Science*, 358(6366):1072–1074, 2017.

[74] Péter Galajda and Pál Ormos. Complex micromachines produced and driven by light. *Applied Physics Letters*, 78(2):249–251, 2001.

[75] Z.-B. Sun, X.-Z. Dong, W.-Q. Chen, S. Nakanishi, X.-M. Duan, and S. Kawata. Multicolor polymer nanocomposites: In situ synthesis and fabrication of 3d microstructures. *Advanced Materials*, 20(5):914–919, 2008.

[76] George Kumi, Ciceron O. Yanez, Kevin D. Belfield, and John T. Fourkas. High-speed multiphoton absorption polymerization: Fabrication of microfluidic channels with arbitrary cross-sections and high aspect ratios. *Lab on a Chip - Miniaturisation for Chemistry and Biology*, 10(8):1057–1060, 2010. Copyright: Copyright 2018 Elsevier B.V., All rights reserved.

[77] Ada-Ioana Bunea, Daniele Martella, Sara Nocentini, Camilla Parmeggiani, Rafael Taboryski, and Diederik S. Wiersma. Light-powered microrobots: Challenges and opportunities for hard and soft responsive microswimmers. *Advanced Intelligent Systems*, 3(4):2000256, 2021.

[78] Andreas Seidel, Christoph Ohrt, Sven Passinger, Carsten Reinhardt, Roman Kiyan, and Boris N. Chichkov. Nanoimprinting of dielectric loaded surface-plasmon-polariton waveguides using masters fabricated by 2-photon polymerization technique. *J. Opt. Soc. Am. B*, 26(4):810–812, Apr 2009.

[79] Andreas Ostendorf and Boris Chichkov. Two-photon polymerization: A new approach to micromachining. *Photonics Spectra*, 40:72–80, 10 2006.

[80] Anastasia Koroleva, Andrea Deiwick, Alexander Nguyen, Sabrina Schlie-Wolter, Roger Narayan, Peter Timashev, Vladimir Popov, Viktor Bagratashvili, and Boris Chichkov. Osteogenic differentiation of human mesenchymal stem cells in 3-d zr-si organic-inorganic scaffolds produced by two-photon polymerization technique. *PLOS ONE*, 10(2):1–18, 02 2015.

[81] Oliver Vanderpoorten, Quentin Peter, Pavan Challa, Ulrich Keyser, Jeremy Baumberg, Clemens Kaminski, and Tuomas Knowles. Scalable integration of nano-, and microfluidics with hybrid two-photon lithography. *Microsystems and Nanoengineering*, 5, 09 2019.

[82] Dong Wu, Qi-Dai Chen, Li-Gang Niu, Jian-Nan Wang, Juan Wang, Rui Wang, Hong Xia, and Hong-Bo Sun. Femtosecond laser rapid prototyping of nanoshells and suspending components towards microfluidic devices. *Lab Chip*, 9:2391–2394, 2009.

[83] Alexander K. Nguyen and Roger J. Narayan. Two-photon polymerization for biological applications. *Materials Today*, 20(6):314–322, 2017.

[84] Shaun D. Gittard, Philip R. Miller, Ryan D. Boehm, Aleksandr Ovsianikov, Boris N. Chichkov, Jeremy Heiser, John Gordon, Nancy A. Monteiro-Riviere, and Roger J. Narayan. Multiphoton microscopy of transdermal quantum dot delivery using two photon polymerization-fabricated polymer microneedles. *Faraday Discuss.*, 149:171–185, 2011.

[85] Jiaxi Song, Christos Michas, Christopher S. Chen, Alice E. White, and Mark W. Grinstaff. From simple to architecturally complex hydrogel scaffolds for cell and tissue engineering applications: Opportunities presented by two-photon polymerization. *Advanced Healthcare Materials*, 9(1):1901217, 2020.

[86] Zhenjia Huang, Gary Chi-Pong Tsui, Yu Deng, and Chak-Yin Tang. Two-photon polymerization nanolithography technology for fabrication of stimulus-responsive micro/nano-structures for biomedical applications. *Nanotechnology Reviews*, 9(1):1118–1136, 2020.

[87] Frederik Kotz, Alexander S. Quick, Patrick Risch, Tanja Martin, Tobias Hoose, Michael Thiel, Dorothea Helmer, and Bastian E. Rapp. Two-photon polymerization of nanocomposites for the fabrication of transparent fused silica glass microstructures. *Advanced Materials*, 33(9):2006341, 2021.

[88] Sourabh K. Saha, Chuck Divin, Jefferson A. Cuadra, and Robert M. Panas. Effect of Proximity of Features on the Damage Threshold During Submicron Additive Manufacturing Via Two-Photon Polymerization. *Journal of Micro and Nano-Manufacturing*, 5(3), 05 2017. 031002.

[89] Shuai Zhang, Shanggeng Li, Xiangyu Wan, Jiajun Ma, Ning Li, Jing Li, and Qiang Yin. Ultrafast, high-resolution and large-size three-dimensional structure manufacturing through high-efficiency two-photon polymerization initiators. *Additive Manufacturing*, 47:102358, 2021.

[90] Two-photon lithography for three-dimensional fabrication in micro/nanoscale regime: A comprehensive review. *Optics & Laser Technology*, 142:107180, 2021.

[91] Wei Chu, Yuanxin Tan, Peng Wang, Jian Xu, Wenbo Li, Jia Qi, and Ya Cheng. Centimeter-height 3d printing with femtosecond laser two-photon polymerization. *Advanced Materials Technologies*, 3(5):1700396, 2018.

[92] Gregor Weisgrab, Olivier Guillaume, Zhengchao Guo, Patrick Heimel, Paul Slezak, André Poot, Dirk Grijpma, and Aleksandr Ovsianikov. 3d printing of large-scale and highly porous biodegradable tissue engineering scaffolds from poly(trimethylene-carbonate) using two-photon-polymerization. *Biofabrication*, 12(4):045036, sep 2020.

[93] Guang S. He, Loon-Seng Tan, Qingdong Zheng, and Paras N. Prasad. Multiphoton absorbing materials: Molecular designs, characterizations, and applications. *Chemical Reviews*, 108(4):1245–1330, 2008. PMID: 18361528.

[94] Yoichi Kobayashi, Katsuya Mutoh, and Jiro Abe. Stepwise two-photon absorption processes utilizing photochromic reactions. *Journal of Photochemistry and Photobiology C: Photochemistry Reviews*, 34:2–28, 2018.

[95] Milosz Pawlicki, Hazel Collins, Robert Denning, and Harry Anderson. Two-photon absorption and the design of two-photon dyes. *Angewandte Chemie (International ed. in English)*, 48:3244–66, 05 2009.

[96] Joel M. Hales, San-Hui Chi, Vincent W. Chen, and Joseph W. Perry. *TWO-PHOTON ABSORPTION: CONCEPTS, MOLECULAR MATERIALS AND APPLICATIONS*, chapter CHAPTER 13, pages 397–442. World Scientific, 2016.

[97] S. Maruo and S. Kawata. Two-photon-absorbed near-infrared photopolymerization for three-dimensional microfabrication. *Journal of Microelectromechanical Systems*, 7(4):411–415, 1998.

[98] Zahra Faraji Rad, Philip D. Prewett, and Graham J. Davies. High-resolution two-photon polymerization: the most versatile technique for the fabrication of microneedle arrays. *Microsystems & nanoengineering*, 7:71–71, Sep 2021.

[99] Linjie Li, Rafael R. Gattass, Erez Gershgoren, Hana Hwang, and John T. Fourkas. Achieving lambda/20 resolution by one-color initiation and deactivation of polymerization. *Science*, 324(5929):910–913, 2009.

[100] S.-H. Park, D.-Y. Yang, and K.-S. Lee. Two-photon stereolithography for realizing ultraprecise three-dimensional nano/microdevices. *Laser & Photonics Reviews*, 3(1-2):1–11, 2009.

[101] Rafael Gattass and Eric Mazur. Femtosecond laser micromachining in transparent materials. *Nature Photonics*, 2:219–225, 04 2008.

[102] Takuo Tanaka, Atsushi Ishikawa, and Satoshi Kawata. Two-photon-induced reduction of metal ions for fabricating three-dimensional electrically conductive metallic microstructure. *Applied Physics Letters*, 88(8):081107, 2006.

[103] Mariacristina Rumi and Joseph W. Perry. Two-photon absorption: an overview of measurements and principles. *Adv. Opt. Photon.*, 2(4):451–518, Dec 2010.

[104] Aleksandr Ovsianikov, Vladimir Mironov, Jurgen Stampfl, and Robert Liska. Engineering 3d cell-culture matrices: Multiphoton processing technologies for biological and tissue engineering applications. *Expert review of medical devices*, 9, 09 2012.

[105] Caizhi Liao, Alain Wuethrich, and Matt Trau. A material odyssey for 3d nano/microstructures: two photon polymerization based nanolithography in bioapplications. *Applied Materials Today*, 19:100635, 2020.

[106] W Denk, JH Strickler, and WW Webb. Two-photon laser scanning fluorescence microscopy. *Science*, 248(4951):73–76, 1990.

[107] Marco Carlotti and Virgilio Mattoli. Functional materials for two-photon polymerization in microfabrication. *Small*, 15(40):1902687, 2019.

[108] Mei-Ling Zheng and Xuan-Ming Duan. *Photoinitiators for Multiphoton Absorption Lithography*, chapter 6, pages 133–165. John Wiley & Sons, Ltd, 2016.

[109] Aleksandr Ovsianikov, Vladimir Mironov, Jurgen Stampfl, and Robert Liska. Engineering 3d cell-culture matrices: Multiphoton processing technologies for biological and tissue engineering applications. *Expert review of medical devices*, 9, 09 2012.

[110] C.K. Ober and K. Müllen. 8.01 - introduction – applications of polymers. In Krzysztof Matyjaszewski and Martin Möller, editors, *Polymer Science: A Comprehensive Reference*, pages 1–8. Elsevier, Amsterdam, 2012.

[111] Wei Lin, Dihan Chen, and Shih-Chi Chen. Emerging micro-additive manufacturing technologies enabled by novel optical methods. *Photon. Res.*, 8(12):1827–1842, Dec 2020.

[112] Ka-Wai Yeung, Yuqing Dong, Ling Chen, Chak-Yin Tang, Wing-Cheung Law, Gary Tsui, and Daniel Engstrom. Printability of photo-sensitive nanocomposites using two-photon polymerization. *Nanotechnology Reviews*, 9:418–425, 05 2020.

[113] Roger J Narayan, Anand Doraiswamy, Douglas B Chrisey, and Boris N Chichkov. Medical prototyping using two photon polymerization. *Materials Today*, 13(12):42–48, 2010.

[114] Amol A. Pawar, Gabriel Saada, Ido Cooperstein, Liraz Larush, Joshua A. Jackman, Seyed R. Tabaei, Nam-Joon Cho, and Shlomo Magdassi. High-performance 3d printing of hydrogels by water-dispersible photoinitiator nanoparticles. *Science Advances*, 2(4):e1501381, 2016.

[115] Nir Waiskopf, Shlomo Magdassi, and Uri Banin. Quantum photoinitiators: Toward emerging photocuring applications. *Journal of the American Chemical Society*, 143(2):577–587, 2021.

[116] M. Guvendiren, B. Purcell, and J.A. Burdick. 9.22 - photopolymerizable systems. In Krzysztof Matyjaszewski and Martin Möller, editors, *Polymer Science: A Comprehensive Reference*, pages 413–438. Elsevier, Amsterdam, 2012.

[117] C. Mendonça, D. S. Correa, T. Baldacchini, P. Tayalia, and E. Mazur. Two-photon absorption spectrum of the photoinitiator lucirin tpo-l. *Applied Physics A*, 90:633–636, 2008.

[118] R. Schwalm. Photoinitiators and photopolymerization. In K.H. Jürgen Buschow, Robert W. Cahn, Merton C. Flemings, Bernhard Ilschner, Edward J. Kramer, Subhash Mahajan, and Patrick Veyssière, editors, *Encyclopedia of Materials: Science and Technology*, pages 6946–6951. Elsevier, Oxford, 2001.

[119] Katherine J Schafer, Joel M Hales, Mihaela Balu, Kevin D Belfield, Eric W Van Stryland, and David J Hagan. Two-photon absorption cross-sections of common photoinitiators. *Journal of Photochemistry and Photobiology A: Chemistry*, 162(2):497–502, 2004.

[120] Katherine J Schafer, Joel M Hales, Mihaela Balu, Kevin D Belfield, Eric W Van Stryland, and David J Hagan. Two-photon absorption cross-sections of common photoinitiators. *Journal of Photochemistry and Photobiology A: Chemistry*, 162(2):497–502, 2004.

[121] Marius Albota, David Beljonne, Jean-Luc Brédas, Jeffrey E. Ehrlich, Jia-Ying Fu, Ahmed A. Heikal, Samuel E. Hess, Thierry Kogej, Michael D. Levin, Seth R. Marder, Dianne McCord-Maughon, Joseph W. Perry, Harald Röckel, Mariacristina Rumi, Girija Subramaniam, Watt W. Webb, Xiang-Li Wu, and Chris Xu. Design of organic molecules with large two-photon absorption cross sections. *Science*, 281(5383):1653–1656, 1998.

[122] Paweł Fiedor and Joanna Ortyl. A new approach to micromachining: High-precision and innovative additive manufacturing solutions based on photopolymerization technology. *Materials*, 13(13), 2020.

[123] José M. Quero, Francisco Perdigones, and Carmen Aracil. 11 - microfabrication technologies used for creating smart devices for industrial applications. In Stoyan Nihtianov and Antonio Luque, editors, *Smart Sensors and MEMs (Second Edition)*, Woodhead Publishing Series in Electronic and Optical Materials, pages 291–311. Woodhead Publishing, second edition edition, 2018.

[124] J. M. Shaw, J. D. Gelorme, N. C. LaBianca, W. E. Conley, and S. J. Holmes. Negative photoresists for optical lithography. *IBM Journal of Research and Development*, 41(1.2):81–94, 1997.

[125] Ming-Bo Lin. *Introduction to VLSI Systems: A Logic, Circuit, and System Perspective*. CRC Press, 11 2011.

[126] Tae Woo Lim, Sang Hu Park, and Dong-Yol Yang. Contour offset algorithm for precise patterning in two-photon polymerization. *Microelectronic Engineering*, 77(3):382–388, 2005.

[127] Hong-Bo Sun and Satoshi Kawata. Two-photon photopolymerization and 3d lithographic microfabrication. *Advances in Polymer Science*, 170:169–273, 2004.

[128] Xiaoqin Zhou, Yihong Hou, and Jieqiong Lin. A review on the processing accuracy of two-photon polymerization. *AIP Advances*, 5(3):030701, 2015.

[129] Kenji Takada, Hong-Bo Sun, and Satoshi Kawata. Improved spatial resolution and surface roughness in photopolymerization-based laser nanowriting. *Applied Physics Letters*, 86:071122 – 071122, 03 2005.

[130] Hong-Bo Sun, Makoto Maeda, Kenji Takada, James Chon, Min Gu, and Satoshi Kawata. Experimental investigation of single voxels for laser

nanofabrication via two-photon photopolymerization. *Applied Physics Letters*, 83:819–821, 08 2003.

[131] Edvinas Skliutas, Migle Lebedevaite, Elmina Kabouraki, Tommaso Baldacchini, Jolita Ostrauskaite, Maria Vamvakaki, Maria Farsari, Saulius Juodkazis, and Mangirdas Malinauskas. Polymerization mechanisms initiated by spatiotemporally confined light. *Nanophotonics*, 10(4):1211–1242, 2021.

[132] Linas Jonušauskas, Tomas Baravykas, Dovilė Andrijec, Tomas Gadisauskas, and Vytautas Purlys. Stitchless support-free 3d printing of free-form micromechanical structures with feature size on-demand. *Scientific Reports*, 9, 11 2019.

[133] Elli Käpylä, Tomáš Sedlačík, Dogu Baran Aydogan, Jouko Viitanen, František Rypáček, and Minna Kellomäki. Direct laser writing of synthetic poly(amino acid) hydrogels and poly(ethylene glycol) diacrylates by two-photon polymerization. *Materials Science and Engineering: C*, 43:280–289, 2014.

[134] Matthew Hunt, Mike Taverne, Joseph Askey, Andrew May, Arjen Van Den Berg, Ying-Lung Daniel Ho, John Rarity, and Sam Ladak. Harnessing multi-photon absorption to produce three-dimensional magnetic structures at the nanoscale. *Materials*, 13(3), 2020.

[135] Kwang-Sup Lee, Ran Hee Kim, Dong-Yol Yang, and Sang Hu Park. Advances in 3d nano/microfabrication using two-photon initiated polymerization. *Progress in Polymer Science*, 33(6):631–681, 2008.

[136] Adriano J. G. Otuka, Nathália B. Tomazio, Kelly T. Paula, and Cleber R. Mendonça. Two-photon polymerization: Functionalized microstructures, microresonators, and bio-scaffolds. *Polymers*, 13(12), 2021.

[137] Lei Zheng, Kestutis Kurselis, Ayman El-Tamer, Ulf Hinze, Carsten Reinhardt, Ludger Overmeyer, and Boris Chichkov. Nanofabrication of high-resolution periodic structures with a gap size below 100 nm by two-photon polymerization. *Nanoscale Research Letters*, 14, 12 2019.

[138] Tommaso Baldacchini. *Three-Dimensional Microfabrication Using Two-Photon Polymerization: Fundamentals, Technology, and Applications*. Elsevier Science Ltd, 01 2015.

[139] Koji Sugioka and Ya Cheng. A tutorial on optics for ultrafast laser materials processing: basic microprocessing system to beam shaping and advanced focusing methods. *Advanced Optical Technologies*, 1(5):353–364, 2012.

[140] Aleksandr Ovsianikov, Sven Passinger, Ruth Houbertz, and Boris Chichkov. *Three Dimensional Material Processing with Femtosecond Lasers*, volume 129, pages 121–157. Springer, 01 2007.

[141] Thomas Stichel, Bert Hecht, Ruth Houbertz, and Gerhard Sextl. Two-photon polymerization as method for the fabrication of large scale biomedical scaffold applications. *Journal of Laser Micro/Nanoengineering*, 5(3), 2010.

[142] Sourabh K. Saha, Dien Wang, Vu H. Nguyen, Yina Chang, James S. Oakdale, and Shih-Chi Chen. Scalable submicrometer additive manufacturing. *Science*, 366(6461):105–109, 2019.

[143] Mark R Prausnitz, Samir Mitragotri, and Robert Langer. Current status and future potential of transdermal drug delivery. *Nature reviews. Drug discovery*, 3(2):115—124, February 2004.

[144] Rezvan Jamaledin, Pooyan Makvandi, Cynthia K. Y. Yiu, Tarun Agarwal, Raffaele Vecchione, Wujin Sun, Tapas Kumar Maiti, Franklin R. Tay, and Paolo Antonio Netti. Engineered microneedle patches for controlled release of active compounds: Recent advances in release profile tuning. *Advanced Therapeutics*, 3(12):2000171, 2020.

[145] H. X. Nguyen and A. Banga. Enhanced skin delivery of vismodegib by microneedle treatment. *Drug Delivery and Translational Research*, 5:407–423, 2015.

[146] Shaun Gittard, Aleksandr Ovsianikov, Boris Chichkov, Anand Doraiswamy, and J. Narayan. Two photon polymerization of microneedles for transdermal drug delivery. *Expert opinion on drug delivery*, 7:513–33, 03 2010.

[147] Ana Cordeiro, Ismaiel Tekko, Mohamed Hedi Jomaa, Lalitkumar Vora, Emma McAlister, Fabiana Volpe Zanutto, Matthew Nethery, P. Baine, Neil Mitchell, David McNeill, and Ryan Donnelly. Two-photon polymerisation 3d printing of microneedle array templates with versatile designs: Application in the development of polymeric drug delivery systems. *Pharmaceutical Research*, 37, 08 2020.

[148] Muhammad Waseem Ashraf, Shahzadi Tayyaba, and Nitin Afzulpurkar. Micro electromechanical systems (mems) based microfluidic devices for biomedical applications. *International Journal of Molecular Sciences*, 12(6):3648–3704, 2011.

[149] Jian Yang, Xinli Liu, Yunzhi Fu, and Yujun Song. Recent advances of microneedles for biomedical applications: drug delivery and beyond. *Acta Pharmaceutica Sinica B*, 9(3):469–483, 2019.

[150] Eneko Larrañeta, Maelíosa McCrudden, Aaron Courtenay, and Ryan Donnelly. Microneedles: A new frontier in nanomedicine delivery. *Pharmaceutical Research*, 33:1–19, 05 2016.

[151] Amina Tucak, Merima Sirbubalo, Lamija Hindija, Ognjenka Rahić, Jasmina Hadžiabdić, Kenan Muhamedagić, Ahmet Čekić, and Edina Vranić. Microneedles: Characteristics, materials, production methods and commercial development. *Micromachines*, 11(11), 2020.

[152] Seyyedhossien Mckee, Adrian Lutey, Corrado Sciancalepore, Federica Poli, Stefano Selleri, and Annamaria Cucinotta. Microfabrication of polymer microneedle arrays using two-photon polymerization. *Journal of Photochemistry and Photobiology B: Biology*, 229:112424, 2022.

[153] Aisling Ní Annaidh, Karine Bruyère, Michel Destrade, Michael D. Gilchrist, and Mélanie Otténio. Characterization of the anisotropic mechanical properties of excised human skin. *Journal of the Mechanical Behavior of Biomedical Materials*, 5(1):139–148, 2012.

[154] Pooyan Makvandi, Melissa Kirkby, Aaron R J Hutton, Majid Shabani, Cynthia K Y Yiu, Zahra Baghbantaraghdari, Rezvan Jamaledin, Marco Carlotti, Barbara Mazzolai, Virgilio Mattoli, and Ryan F Donnelly. Engineering microneedle patches for improved penetration: Analysis, skin models and factors affecting needle insertion. *Nano-Micro Letters*, 13, March 2021.

[155] Zhiyong Zhao, Ming Tang, and Chao Lu. Distributed multicore fiber sensors. *Opto-Electronic Advances*, 3:19002401–19002417, 02 2020.

[156] Nikolay A. Kalinin, Elena A. Anashkina, Olga N. Egorova, Sergey G. Zhuravlev, Sergei L. Semjonov, Arkady V. Kim, Alexander G. Litvak, and Alexey V. Andrianov. Controlled excitation of supermodes in a multicore fiber with a 5×5 square array of strongly coupled cores. *Photonics*, 8(8), 2021.

[157] A. A. Balakin, S. A. Skobelev, A. V. Andrianov, E. A. Anashkina, and A. G. Litvak. Coherent amplification of high-power laser radiation in multicore fibers from a rectangular array of cores. *Opt. Lett.*, 46(2):246–249, Jan 2021.

[158] Nemanja Jovanovic, Olivier Guyon, Hajime Kawahara, and Takayuki Kotani. Application of multicore optical fibers in astronomy. In *2017 Optical Fiber Communications Conference and Exhibition (OFC)*, pages 1–3, 2017.

[159] Andrés Macho and Roberto Llorente. *Multi-Core Optical Fibers: Theory, Applications and Opportunities*, chapter 4, pages 63–102. InTech, 02 2018.

[160] Andrés Macho Ortiz and Roberto Llorente Sáez. Multi-core optical fibers: Theory, applications and opportunities. *Selected Topics on Optical Fiber Technologies and Applications*, 2017.

[161] A. Klenke, M. Müller, H. Stark, F. Stutzki, C. Hupel, T. Schreiber, A. Tünnermann, and J. Limpert. Coherently combined 16-channel multicore fiber laser system. *Opt. Lett.*, 43(7):1519–1522, Apr 2018.

[162] Yair Alon, Aviran Halstuch, Raghuraman Sidharthan, Seongwoo Yoo, and Amiel A. Ishaaya. Femtosecond bragg grating inscription in an yb-doped large-mode-area multicore fiber for high-power laser applications. *Opt. Lett.*, 45(16):4563–4566, Aug 2020.

[163] A. V. Andrianov, S. A. Skobelev, A. A. Balakin, E. A. Anashkina, and A. G. Litvak. Tapered multicore fiber for high-power laser amplifiers. *IEEE Photonics Journal*, 14(1):1–6, 2022.

[164] Cesar Jauregui, Jens Limpert, and Andreas Tünnermann. High-power fibre lasers. *Nature Photonics*, 7:861–867, 10 2013.

[165] Svetlana Aleshkina, Tatiana Kochergina, Vladimir Velmiskin, Konstantin Bobkov, Mikhail Bubnov, M.V. Yashkov, Denis Lipatov, Mikhail Salganskii, Alexey Guryanov, and M.E. Likhachev. High-order mode suppression in double-clad optical fibers by adding absorbing inclusions. *Scientific Reports*, 10, 04 2020.

[166] Jay W. Dawson, Michael J. Messerly, Raymond J. Beach, Miroslav Y. Shverdin, Eddy A. Stappaerts, Arun K. Sridharan, Paul H. Pax, John E. Heebner, Craig W. Siders, and C.P.J. Barty. Analysis of the scalability of diffraction-limited fiber lasers and amplifiers to high average power. *Opt. Express*, 16(17):13240–13266, Aug 2008.

[167] A Tünnermann, T Schreiber, F Röser, A Liem, S Höfer, H Zellmer, S Nolte, and J Limpert. The renaissance and bright future of fibre lasers. *Journal of Physics B: Atomic, Molecular and Optical Physics*, 38(9):S681–S693, apr 2005.

[168] Govind P. Agrawal. Chapter 5 - fiber lasers. In Govind P. Agrawal, editor, *Applications of Nonlinear Fiber Optics (Third Edition)*, pages 193–254. Academic Press, third edition edition, 2021.

[169] P. Delaporte, D. Karnakis, and I. Zergioti. 12 - laser processing of flexible organic electronic materials. In Stergios Logothetidis, editor, *Handbook of Flexible Organic Electronics*, pages 285–313. Woodhead Publishing, Oxford, 2015.

[170] Sensitization of er3+ nir emission using yb3+ ions in alkaline-earth chloro borate glasses for fiber laser and optical fiber amplifier applications. *Materials Research Bulletin*, 136:111144, 2021.

[171] Flat-gain and wide-band partial double-pass erbium co-doped fiber amplifier with hybrid gain medium. *Optical Fiber Technology*, 52:101952, 2019.

[172] Ahmed Nabih Zaki Rashed, Mohammed Salah F. Tabbour, Shimaa El-Meadawy, Toni Anwar, Aliza Sarlan, P. Yupapin, and I.S. Amiri. The effect of using different materials on erbium-doped fiber amplifiers for indoor applications. *Results in Physics*, 15:102650, 2019.

[173] Aya A. Almukhtar, Alabbas A. Al-Azzawi, X.S. Cheng, P.H. Reddy, A. Dhar, M.C. Paul, H. Ahmad, and S.W. Harun. Enhanced triple-pass hybrid erbium doped fiber amplifier using distribution pumping scheme in a dual-stage configuration. *Optik*, 204:164191, 2020.

[174] Jiangyun Dai, Changle Shen, Nian Liu, Lihua Zhang, Hao Li, Honglei He, Fengyun Li, Yuwei Li, Jiakun Lv, Lei Jiang, Yue Li, Honghuan Lin, Jianjun Wang, Feng Jing, and Cong Gao. 10 kw-level output power from a tandem-pumped yb-doped aluminophosphosilicate fiber amplifier. *Optical Fiber Technology*, 67:102738, 2021.

[175] Jawad Mirza, Salman Ghafoor, Anila Kousar, Benish Kanwal, and Khurram Karim Qureshi. Design of a continuous-wave ytterbium-doped tunable

fiber laser pump for thulium-doped fiber amplifiers. *Arabian Journal for Science and Engineering*, 47(3):3541–3549, jan 2022.

[176] Ping Yan, Zehui Wang, Xuejiao Wang, Qirong Xiao, Yusheng Huang, Jiading Tian, Dan Li, and Mali Gong. Beam transmission properties in high power ytterbium-doped tandem-pumping fiber amplifier. *IEEE Photonics Journal*, 11(2):1–12, 2019.

[177] Cesar Jauregui, Jens Limpert, and Andreas Tünnermann. High-power fibre lasers. *Nature Photonics*, 7:861–867, 10 2013.

[178] Wei Shi, Qiang Fang, Xiushan Zhu, R. A. Norwood, and N. Peyghambarian. Fiber lasers and their applications. *Appl. Opt.*, 53(28):6554–6568, Oct 2014.

[179] Bin Yin, Suchun Feng, Zhibo Liu, Yunlong Bai, and Shuisheng Jian. Single-frequency and single-polarization dfb fiber laser based on tapered fbg and self-injection locking. *Photonics Journal, IEEE*, 7:1–9, 06 2015.

[180] Cesar Jauregui, Christoph Stihler, and Jens Limpert. Transverse mode instability. *Adv. Opt. Photon.*, 12(2):429–484, Jun 2020.

[181] Bryce Samson Liang Dong. *Nonlinear Effects in Optical Fibers*, chapter chapter3. CRC Press, 2016.

[182] Zhen Xing, Xin Wang, Shuqin Lou, Zijuan Tang, Haoqiang Jia, Shuai Gu, and Jihong Han. Large-mode-area all-solid anti-resonant fiber with single-mode operation for high-power fiber lasers. *Opt. Lett.*, 46(8):1908–1911, Apr 2021.

[183] Cesar Jauregui, Jens Limpert, and Andreas Tünnermann. Ultra-large mode area fibers for high power lasers. In *Optical Fiber Communication Conference*, page M2J.1. Optical Society of America, 2018.

[184] Fabian Stutzki, Florian Jansen, Tino Eidam, Alexander Steinmetz, Cesar Jauregui, Jens Limpert, and Andreas Tünnermann. High average power large-pitch fiber amplifier with robust single-mode operation. *Opt. Lett.*, 36(5):689–691, Mar 2011.

[185] C. Molardi, F. Poli, L. Rosa, S. Selleri, and A. Cucinotta. Mode discrimination criterion for effective differential amplification in yb-doped fiber design for high power operation. *Opt. Express*, 25(23):29013–29025, Nov 2017.

[186] Tino Eidam, Christian Wirth, Cesar Jauregui, Fabian Stutzki, Florian Jansen, Hans-Jürgen Otto, Oliver Schmidt, Thomas Schreiber, Jens Limpert, and Andreas Tünnermann. Experimental observations of the threshold-like onset of mode instabilities in high power fiber amplifiers. *Opt. Express*, 19(14):13218–13224, Jul 2011.

[187] Tino Eidam, Christian Wirth, Cesar Jauregui, Fabian Stutzki, Florian Jansen, Hans-Jürgen Otto, Oliver Schmidt, Thomas Schreiber, Jens Limpert, and Andreas Tünnermann. Experimental observations of the threshold-like onset of mode instabilities in high power fiber amplifiers. *Opt. Express*, 19(14):13218–13224, Jul 2011.

[188] Christian Gaida, Martin Gebhardt, Tobias Heuermann, Ziyao Wang, Cesar Jauregui, and Jens Limpert. Transverse mode instability and thermal effects in thulium-doped fiber amplifiers under high thermal loads. *Opt. Express*, 29(10):14963–14973, May 2021.

[189] Cesar Jauregui, Christoph Stihler, and Jens Limpert. Transverse mode instability. *Adv. Opt. Photon.*, 12(2):429–484, Jun 2020.

[190] Kuniharu Himeno. Basics and features of high-power fiber laser. volume 44. Fujikura, March 2015.

[191] Jesper Lægsgaard, Federica Poli, Annamaria Cucinotta, and Stefano Selleri. Theory of thermo-optic instabilities in dual-core fiber amplifiers. *Optics Letters*, 43(19):4775–4778, 2018.

[192] Georg Rademacher, Ruben S. Luís, Benjamin J. Puttnam, Yoshinari Awaji, and Naoya Wada. Crosstalk dynamics in multi-core fibers. *Opt. Express*, 25(10):12020–12028, May 2017.

[193] K. Petermann. 1 - oxide laser crystals doped with rare earth and transition metal ions. In B. Denker and E. Shklovsky, editors, *Handbook of Solid-State Lasers*, Woodhead Publishing Series in Electronic and Optical Materials, pages 3–27. Woodhead Publishing, 2013.

[194] Mette Marie Johansen, Kristian Rymann Hansen, Marko Laurila, Thomas Tanggaard Alkeskjold, and Jesper Lægsgaard. Estimating modal instability threshold for photonic crystal rod fiber amplifiers. *Opt. Express*, 21(13):15409–15417, Jul 2013.

[195] Yuanyuan Fan, Bing He, Jun Zhou, Jituo Zheng, Houkang Liu, Yunrong Wei, Jingxing Dong, and Qihong Lou. Thermal effects in kilowatt all-fiber mopa. *Opt. Express*, 19(16):15162–15172, Aug 2011.

[196] David L. Fain. Planck and stefan–boltzmann laws in refractive media. *Journal of the Optical Society of America*, 55(4):460–461, Apr 1965.

[197] Robert H. Kingston. Chapter 1 - blackbody radiation, image plane intensity, and units. In Robert H. Kingston, editor, *Optical Sources, Detectors, and Systems*, Optics and Photonics, pages 1–32. Academic Press, Burlington, 1995.

[198] Enrico Coscelli, Federica Poli, Thomas Tanggaard Alkeskjold, Mette Marie Jørgensen, Lasse Leick, Jes Broeng, Annamaria Cucinotta, and Stefano Selleri. Thermal effects on the single-mode regime of distributed modal filtering rod fiber. *J. Lightwave Technol.*, 30(22):3494–3499, Nov 2012.

[199] L. Rosa, H. Mckee, F. Poli, S. Selleri, L. Vincetti, and A. Cucinotta. Thermally-driven mode coupling in multi-core optical fibers. In *Advanced Photonics 2018 (BGPP, IPR, NP, NOMA, Sensors, Networks, SPPCom, SOF)*, page JTu5A.79. Optical Society of America, 2018.

[200] Clémence Jollivet, Arash Mafi, Daniel Flamm, Michael Duparré, Kay Schuster, Stephan Grimm, and Axel Schülzgen. Mode-resolved gain analysis and lasing in multi-supermode multi-core fiber laser. *Opt. Express*, 22(24):30377–30386, Dec 2014.

[201] Hans-Jürgen Otto, Arno Klenke, Cesar Jauregui, Fabian Stutzki, Jens Limpert, and Andreas Tünnermann. Scaling the mode instability threshold with multicore fibers. *Opt. Lett.*, 39(9):2680–2683, May 2014.

[202] Seyyedhossein Mckee, Federica Poli, Stefano Selleri, Annamaria Cucinotta, Lorenzo Rosa, and Luca Vincetti. Guidance properties and thermal effects in 9-core yb-doped fiber for high power applications. In *2019 IEEE 5th International forum on Research and Technology for Society and Industry (RTSI)*, pages 380–383, 2019.

[203] Lorenzo Rosa, Seyyedhossein Mckee, Federica Poli, Annamaria Cucinotta, and Luca Vincetti. Thermo-optical numerical modal analysis of multicore fibers for high power lasers and amplifiers. *Optical Fiber Technology*, 70:102857, 2022.

[204] Lorenzo Rosa, Seyyedhossein Mckee, Luca Vincetti, Federica Poli, Stefano Selleri, and Annamaria Cucinotta. Thermo-optic effects in multicore fibers for high-power lasers. In Maurizio Ferrari, Jacob I. Mackenzie, and Stefano Taccheo, editors, *Fiber Lasers and Glass Photonics: Materials through Applications II*, volume 11357, pages 165 – 170. International Society for Optics and Photonics, SPIE, 2020.

Acknowledgements

There are a number of people without whom this thesis might not have been completed and to whom I am greatly indebted.
First and foremost, I offer my sincerest gratitude to my wonderful supervisor Professor Annamaria Cucinotta. Her scholarly advice, meticulous scrutiny, dedication, keen interest and her overwhelming attitude to help her students enabled me to accomplish this task. It was a great honor for me to work under the supervision of such an outstanding professor.
I would like to acknowledge my brilliant advisor Dr. Adrian H.A. Lutey who played a significant role in aligning the components and setting the two-photon polymerization system up for his invaluable support and assistance in overcoming many of the challenges I faced during my study.
I would like to express my very great appreciation to Professors Federica Poli and Stefano Selleri for their generous guidance, expertise and support. Despite the hectic schedule, the door of their office was always open whenever I confronted a problem or had a question about my research project.
I would also like to thank Prof. Anna Painelli, Prof. Francesca Terenziani, Prof. Daniel Milanese and Dr. Corrado Sciancalepore for their support and insightful suggestions as well as Prof. Alessandro Fortunato for providing the laser setup employed for experiments.
In addition, I would like to acknowledge Prof. Boris Chichkov, Dr. Ulf Hinze and Dr. Roman Kiyan for their guidance and teaching during my stay at Laser nanoFab in Hannover (Germany) which was a very valuable experience for me to learn more

about microfabrication via two-photon polymerization technique.
Finally, I am particularly grateful for the assistance given by Professors Luca Vincetti and Lorenzo Rosa. Their valuable and constructive suggestions, enthusiastic encouragement and useful critiques made it possible for me to enhance my practical knowledge about multicore fiber laser technology and to work on a topic that is of great interest to me.